# Junction design strategies in molecular electronics


UNIVERSITY OF LIVERPOOL

Thesis submitted in accordance with the requirements of the University of Liverpool for the degree of Doctor in Philosophy by

**Inco J. Planje**

September
**2019**

# Abstract

The field of molecular electronics ultimately aims to develop electronic devices using single molecules as building blocks. To achieve this goal, a thorough understanding of the structure-property relationships in molecular architectures is crucial. The past few decades have seen an explosive number of studies in this emerging field, establishing a solid foundation for electronic interactions at the nanoscale. Despite this progress, the route to genuinely stable and reproducible devices still faces many challenges. This work contributes to tackling some of these challenges by studying the effects of manipulating components of a nanoscale junction on its electronic transport properties. Scanning tunnelling microscopy techniques are employed to fabricate junctions and measure the current through them.

Firstly, the influence of junction design on electron transport is studied by inserting platinum or ruthenium metal atoms in the molecular bridge. These organometallic wires generally have a higher conductance than their organic counterparts due to a smaller gap between highest occupied and lowest unoccupied molecular orbitals. However, in the thioether induced midgap wires studied here, only the ruthenium wires show an increased conductance. This is a result of a stronger coupling between molecule and metal, and a better distribution of orbitals along the entire junction, which is not the case for the platinum wires.

In the second part, one of the two metal electrodes is replaced by transparent indium tin oxide for future optoelectronic studies and applications. New anchoring groups for binding to this semiconductor electrode are designed and show promising results, including one group that only binds to this indium tin oxide electrode. Moderate rectification is also observed for these metal-molecule-semiconductor junctions.

In the third and last part, three junction designs for studying complex effects in molecular structures are discussed. The first is a three-dimensional metal complex, designed to study supramolecular lateral effects, where the metal does not seem to participate in the transport pathway. The second contains a metallic anchoring group, which does not seem to be suitable for forming junctions using the dynamic scanning tunnelling microscopy break-junction technique. Finally, a molecular wire that is designed for optical switching shows a curious inverse correlation of conductance with applied bias voltage. The results presented here confirm yet again that there is a complex interplay between several key parameters, which together dictate the electrical behaviour of nanoscale junctions.

# Contents

# List of Figures

# List of Tables

# List of Acronyms and Symbols

| | |
|---|---|
| 1D | One-dimensional |
| 2D | Two-dimensional |
| AFM | Atomic force microscope/microscopy |
| DFT | Density functional theory |
| DHP | Dihydropyrene |
| DMBT | Dimethylbenzothiophene |
| $E_F$ | Fermi energy |
| eV | Electronvolt |
| $\varepsilon$ | Energy-level offset between Fermi level and HOMO or LUMO |
| $\varepsilon$ | Molar extinction coefficient (only in section 4.3) |
| G | Conductance |
| HOMO | Highest occupied molecular orbital |
| I | Current |
| IR | Infrared |
| ITO | Indium tin oxide |
| $k_B$ | Boltzmann constant |
| LUMO | Lowest unoccupied molecular orbital |
| nN | Nano newton |
| QCM | Quartz crystal microbalance |
| SAM | Self-assembled monolayer |
| SEC | Spectroelectrochemistry |
| SMe | Methyl thioether |
| STM | Scanning tunnelling microscope/microscopy |
| STMBJ | STM break-junction |
| STM-I(s) | STM current-distance spectroscopy |
| STM-I(t) | STM current-time spectroscopy |
| T | Temperature |
| UV-VIS | Ultraviolet–visible |
| V | Voltage |
| XPS | X-ray photoelectron spectroscopy |

# Chapter 1

# Introduction

*"I learned very early the difference between knowing the name of something and knowing something."*

— **Richard P. Feynman**

Silicon is the major component in almost all commercial electronic devices [1]. However, chip fabrication using silicon has now reached its fundamental limit in scaling down transistors, as predicted by Moore in the sixties [2]. Therefore, high demand for alternative designs is now driving the use of novel materials and architectures, in both research laboratories and industry alike. A promising approach is the use of single molecules as active components, because of their reduced size, structural diversity obtained through flexible chemical design, and vast availability using facile bulk synthesis [3]. Creating these molecule-based nanoelectronic devices requires a fundamental understanding of conductance mechanisms across metal-molecule-metal junctions. The properties of molecules have been studied intensively for about a century. A few early visionary ideas slowly conceived possible ways to combine the two broad research areas of molecular sciences and electronics. But it was not until the development of some key techniques like the scanning tunnelling microscope (STM) [4] and the atomic force microscope (AFM) [5], that experimental verification of these ideas became possible. Following these breakthroughs in nanoscale science, the field of molecular electronics started to take shape. It has grown rapidly since then and has allowed for synergistic discoveries in both electronic engineering and the structure-property relationships of molecules. Specifically, molecules have been studied as individual units or small assemblies of units, allowing for conditions that are far from thermodynamic equilibrium. Over the years, molecular electronics has evolved and matured significantly and now involves many branches of science to make a highly interdisciplinary field. Nevertheless, molecular electronics would not be anywhere without the pioneering development of the transistor by Shockley and colleagues.

## 1.1 History of molecular electronics

The history of commercial electronic chips can be pointed to the invention of the transistor. It was conceived independently by Lilienfield in 1926, Heil in

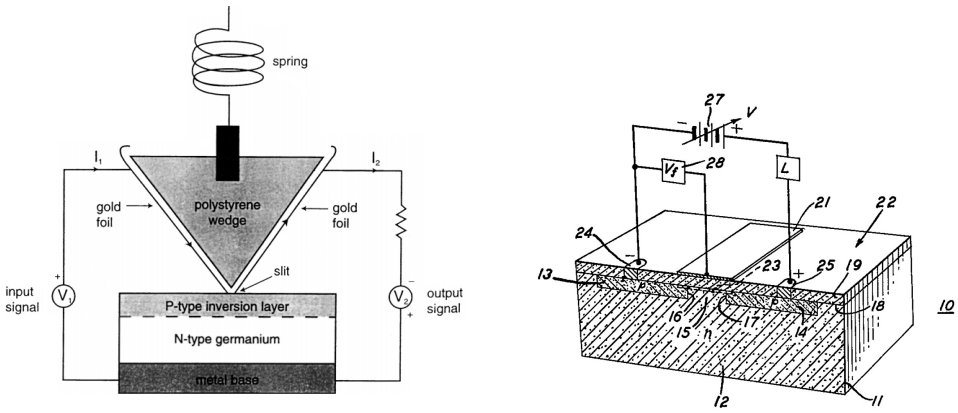


**Figure 1.1** Schematic illustration of the first transistor (left), and the metal oxide semiconductor transistor that allowed for easy mass production and miniaturisation (right). *Adapted from reference [6] and US patent No. 3,102,230 [7].*

1930, and Shockley in 1935, before being realised in 1947 in the laboratories of Bell Labs [6], see left panel of Figure 1.1. This work was awarded the 1956 Nobel Prize in Physics. However, this device was neither optimised for mass production nor easy to reduce in physical size. Both of these problems were overcome by Atalla and Kahng in 1961, who developed the metal oxide semiconductor field-effect transistor (MOSFET). Approximately 70 years later, we currently know what a ground-breaking discovery this was for making possible the technologies of today. Soon after the first few electronic MOSFET chips were developed, Moore recognised a halving trend, which he predicted to continue for about a decade [2]. In short, the number of resistors per unit area would double approximately every two years. Therefore, computing power (and speed) would also double every two years. This became known as Moore's law and ended up holding true until the 21$^{st}$ century. Von Hippel was the first to propose thinking of atoms and molecules as small building blocks to make larger structures, rather than ever decreasing the size of existing architectures [8]. This is the revolutionary bottom-up approach, which has several advantages over the traditional top-down designs. In 1959 Richard Feynman gave a fascinating speech, that is now famous, on why it was important to pursue the world of the small [9]. He invited the scientific community to start exploring the new

and exciting field of nanotechnology. Progress was not very fast in the years that followed, mainly because of experimental limitations to explore and test ideas based on these concepts. Mann et al. were the first to study molecular assemblies in 1971, which were sandwiched between two metal electrodes [10]. Here, they showed a clear dependence of conductance on molecular length, which will be discussed in detail below. Around the same time, Aviram and Ratner published the idea of a molecular diode based on a single molecule that contained both an electron donor and an electron acceptor moiety, separated by a saturated (insulating) carbon chain [11]. This work was paramount to the development of the field of molecular electronics because it was the first case in which a single molecule was the main component of an electrical circuit.

## 1.2 The metal-molecule-metal junction

The setup described by Aviram and Ratner represents a circuit at the nanoscale level, where the molecule is a resistor. A schematic of such a simple circuit is shown in the top panel of Figure 1.2. Connected to a power supply are, from the edges to the centre, first the reservoirs for supplying electrons (the source) and carrying them away (the drain). Changing the polarity of the power supply switches the source and drain around. Moving further inwards, the bulk reservoirs become continuously smaller and lead into electrodes of nanoscale size. Next, the terminal ends of a single molecule are bound to both electrodes, thereby forming the nanoscale junction. The centre of the molecule, also called the bridge or backbone, can be modified depending on the goal for the system in question. Finally, the environment around the junction also plays an important role when designing systems that are either for fundamental exploration of properties or for electronic circuits based on molecular assemblies. Here, the term 'junction' refers to the extended metal-molecule-metal configuration, whereas the molecule by itself is referred to as the 'molecular wire'. Each part of a junction as described above has been studied

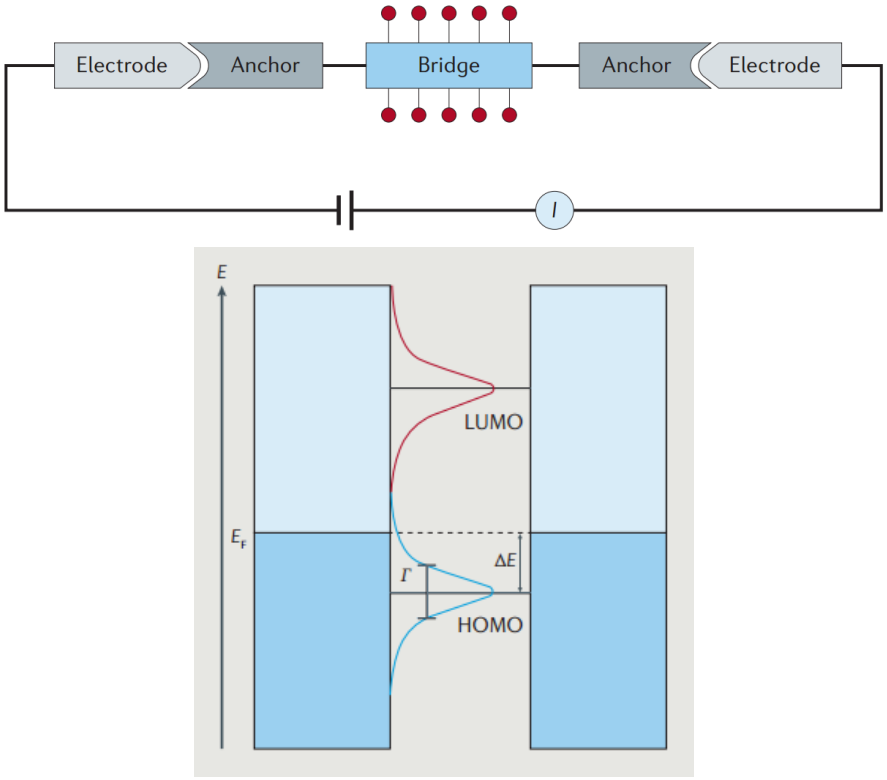


**Figure 1.2** Schematic illustration of a molecular junction (top), and model of energy levels (bottom). *Adapted from reference [12].*

extensively by numerous groups since the first diode that was proposed by Aviram and Ratner. The bottom panel of Figure 1.2 shows the energy levels of the electrodes at zero bias, i.e. no voltage is applied across the junction. When a bias voltage is applied, the positive electrode moves down in energy, and the negative electrode moves up. Then, the change in electrochemical potential between the two electrodes results in a current flow. The Lorentzian Breit-Wigner curves in between the electrodes represent the molecular orbital levels, and are derivative Fermi functions (see chapter 2 for details). These curves are transmission probabilities of electron transport through the molecule. When the HOMO is closer to the electrode Fermi levels, it dominates transport, and the magnitude of the transmission (and thus conductance) corresponds to the area under the curve. This area lies symmetrically around the Fermi energy level, and its width is determined experimentally by the applied bias voltage. It

is also called the bias window and runs from negative 0.5∗V to positive 0.5∗V. For example, if the bias voltage is 300 mV the bias window runs from -150 eV to +150 eV, see section 4.4 for more details.

Often used in the literature, the following variables describe each part of the junction: $\Phi$ for the Fermi levels of the electrodes, $\Gamma$ for the coupling strength between molecular terminals and electrodes, and $\Delta E$ for positions of the frontier molecular orbitals with respect to the Fermi level. A convenient model for transport theory is the single-level model, in which $\Delta E$ is generally replaced by $\varepsilon$. Here the complex collection of molecular orbitals and electrode density of states is simplified by assuming a single energy level that dominates transport. In addition to these important intrinsic junction parameters, other factors that influence the junction performance, conductance, and stability, are external factors (or environmental effects), such as temperature, solvent properties (including pH), light, mechanical effects like stress, strain, and force, electric field strength and polarity, magnetic effects (spintronics). Some of these are useful to map out mechanisms, such as dependence of junction conductance on temperature. Or the effect of the length of a junction, which is a combination of the intrinsic length of the molecule, and the external factor of the separation between the electrodes, or whether the molecule is extended in the junction or not. Other variables are more prominent for studying active components for molecular electronics, for example using light to switch a junction between relative states of high and low conductance.

The conductance values of such junctions are a direct result of the electron transmission probability across the junction [13]. The position of the highest unoccupied molecular orbital (HOMO) and lowest unoccupied molecular orbital (LUMO) of the molecule are important here. This is because the transmission strongly depends on how well the resulting frontier molecular orbitals (FMOs) align with the (metal) electrode Fermi levels [14]. Another important parameter that influences the transmission is the electronic coupling strength between the metal electrodes and the molecule, i.e. the contacts [15]. The anchoring group

of the molecule that binds to the metal electrode plays a key part in this process [16]. Anchoring groups for gold electrodes have been studied widely and include thiols [17], amines [18], methyl sulfides [19], pyridines [20], and covalent carbon [21].

## 1.3 Electrode formation

Various experimental methods exist for creating nanoscale electrodes, which can be categorised according to the number of molecules that are measured simultaneously. Investigating the properties of individual molecules has the advantage of retaining critical information because averaging over vast numbers is not necessary. Measuring ensembles of molecules, on the other hand, is essential for establishing how properties of individual molecules scale up when gathered in large arrays. The majority of experiments to date have focused on electrodes made out of metal. However, nonmetal materials have also shown promising results to form electrode-molecule junctions. A tremendous milestone for the field was the development of scanning probe microscopy (SPM) as it opened up numerous possibilities for measuring both single molecules and ensembles. SPM techniques are discussed in detail in subsection 1.3.1 below because they are the main focus of this thesis.

The first study with a single-molecule resolution was published in 1997 by Reed et al. [22] They measured the conductance of a benzene dithiol molecule using a technique called the mechanically controlled break-junction technique (MCBJ) [23]. The working principle of the MCBJ is relatively straightforward in which a thin metal wire is fabricated on top of a flexible substrate. A push rod then moves this substrate up and down, thereby stretching and compressing the metal wire. When stretched just the right amount, it breaks apart to form a nanogap that can be bridged by molecules in solution to form a junction.

In 1999 two additional techniques were developed for measuring individual molecules, one using electrochemical deposition and the other based on elec-

tromigration. The deposition technique relies on lithography to first create two metal electrodes with a separation of roughly 50-400 nm [24]. The exact distance is not critical because additional metal is electrodeposited in the second step. Monitoring the decreasing resistance between the growing electrodes then provides an exact ditance of atomic resolution. The electromigration technique, on the other hand, forms two nanoscale electrodes by using an electrochemical current to break apart the metallic wire[25]. In a follow-up study, the same group measured the nanomechanical properties of a buckminsterfullerene molecule trapped between gold electrodes [26]. Unfortunately, a significant downside of this technique is that the junction geometry is hard to control.

Carbon is the most promising nonmetal material for creating single-molecule electronic junctions. It is atomically rigid, unlike metal atoms, which are very mobile. This property makes carbon more robust, more reproducible, and easier to scale up. It is also cheap, abundant, and naturally compatible for integration with organic and biological materials. An example architecture for its use as electrodes is the carbon nanotube (CNT) [27]. These structures are produced using an electric arc, laser ablation, or chemical vapour deposition [28]. After immobilisation on a substrate surface, a nanogap is formed either by electrical breakdown using a high-density current [29] or a combination of ion-beam etching and oxidative cutting [30]. More advanced architectures can be achieved using straightforward solution-based chemical methods [31]. Graphene is a two-dimensional atomic sheet of carbon, which is also showing promise as electrode material for molecular-scale electronics [32]. Nanogaps in the direction of the graphene plane can be created using electroburning [33], or dash-line lithography [34]. Single-molecule STM junctions with a perpendicular orientation on graphene were recently studied by Tao et al. [35]. Other nonmetal materials besides carbon include semiconductors like silicon [36–38], indium tin oxide [39], and gallium arsenide [40], but also conducting polymers [41].

Since this work focuses on single-molecule techniques and specifically the STM,

elaborate details of ensemble junctions can be found in the comprehensive review of Xiang et al. [3]. However, a brief overview of the existing techniques is given below. The majority of electrode fabrication methods for measuring molecular assemblies use liquid metals, evaporation, or some form of lithography. It can be somewhat confusing at first to get familiar with each ensemble technique. The reason for this comes from the different names, which can refer to the material used (liquid metals), the process (lithography), or even refer to the resulting architecture (crossbar). On top of this, many critical studies have combined several of the methods in various clever ways.

The first liquid metal experiments were done using two mercury drop electrodes, contacting a monolayer of alkane dithiol molecules [42]. Chiechi et al. developed eutectic gallium-indium (EGaIn) as a different type of liquid electrode [43]. A different approach relies on the so-called lift-off and float-on technique, which softly applies the top electrode onto the molecular layer by using a solvent bath [44]. Loo et al. developed another popular technique in 2003, involving nanotransfer printing [45]. Kushmerick et al. developed a crosswire architecture, where the top contact can be established gently using a controllable magnetic force [46]. The first reported crossbar structure was created using a combination of a polymer-assisted lift-off and nanotransfer printing [47]. In 2007 Tang et al. developed a technique based on self-aligned lithography [48]. Earlier methods already used lithography to create nanopore [49], planar nanowell [50], or on-wire [51] architectures. Akkerman et al. developed the buffer-interlayer technique in 2006 to reduce the number of defect junctions from the penetration of metal through the molecular layer [52]. On-edge architectures first create the complete electrode architecture [53]. The advantage here is that the molecular layer is the last step, which is less invasive and allows for redesigning the junction architecture by changing the molecular layers.

Combinations of techniques include Nijhuis et al. who combined the liquid EGaIn electrode with optical lithography and transfer printing methods to create a crossbar architecture [54]. On-wire lithography has been combined

with gold nanorods [55] and carbon nanotubes [56]. Yu et al. used self-aligned lithography to create nanogap arrays for measuring electrical properties of DNA-linked gold nanoparticles [57]. Another fascinating study used transparent graphene oxide electrodes to sandwich a molecular layer [58].
Recently a new technique developed by Dubois et al. even offers the flexibility of measuring single molecules as well as molecular ensembles [59]. This fully scalable crack-defined break junction (CDBJ) relies on a brittle material present underneath the electrode material. Under the right conditions, reproducible cracks in this brittle material are capable of producing large arrays of junctions. Another method that shows promise to have similar flexibility in scaling is surface-diffusion-mediated deposition (SDMD) as developed by Bonifas et al. [60, 61]. It offers a solution to the problem of metal deposition damaging the molecular layer. The deposition of metal atoms happens remotely rather than directly on top of the monolayer. The deposited atoms then diffuse laterally towards the horizontally oriented monolayer to contact anywhere between one and ten molecules in the layer. The number of contacted molecules can potentially be scaled up several orders of magnitude.

### 1.3.1 Scanning probe microscopy

Two critical techniques that are now collectively referred to as surface probe microscopy (SPM) were developed in the eighties. First, Binnig et al. described a vacuum tunnelling experiment with mechanical stability in 1982 [62], followed by the scanning tunnelling microscope (STM) in the same year [4]. The left panel in Figure 1.3 shows a schematic illustration of the STM. Here, a conductive substrate is connected to an electrical circuit, which in turn is connected to a piezo scanner. A conductive tip, usually a metal wire, is then mounted into the piezo tube and is placed a few hundred micrometres from the substrate surface. A potential is then applied between the tip and the substrate, normally called $V_{bias}$. Next, a mechanical stepper motor is used to approach the tip to the substrate until the system registers a tunnelling setpoint

current, which is typically in the range of nA. From this point onwards, the piezo feedback takes over from the mechanical motor for precise control over the current value. Scanning the substrate surface is then achieved by maintaining a constant current, which means that the separation between tip and substrate varies, thereby mapping the height profile of the substrate.

Theoretical principles of the STM were published by Hamann et al. a few years later [63]. This publication was followed up shortly after that by another surface probe technique called atomic force microscopy (AFM) [5], see the middle panel of Figure 1.3. This technique relies on a force between the sample and the probe rather than an electrical tunnelling current. Now that several relatively convenient methods for probing the properties of molecules on a surface were available, many groups started measuring transport properties of molecular assemblies, an example of which was first published by Aviram et al. [64]. Wold et al. later expanded the AFM technique to measure the electrical properties of a self-assembled monolayer at the same time as measuring the force. They achieved this combined conducting probe AFM setup (CPAFM) by coating the AFM probe [65]. The schematic of their experiment is shown in the right panel of Figure 1.3. Using a similar setup a year later, Cui et al. developed the matrix isolation technique [66]. They first created a single-molecule environment by inserting small quantities of dithiol molecules into an existing layer of monothiols. They then added gold nanoparticles on top of this monolayer to provide a robust contact to the conducting AFM probe for measuring the electrical properties of the dithiol molecules.

### Scanning tunnelling spectroscopy

The STM has become an extensive platform for the use of single-molecule techniques. Especially since 2003, when several breakthrough methods were developed in quick succession. For example, Xu et al. published the STM break-junction method as presented in Figure 1.4, one of the most widely used

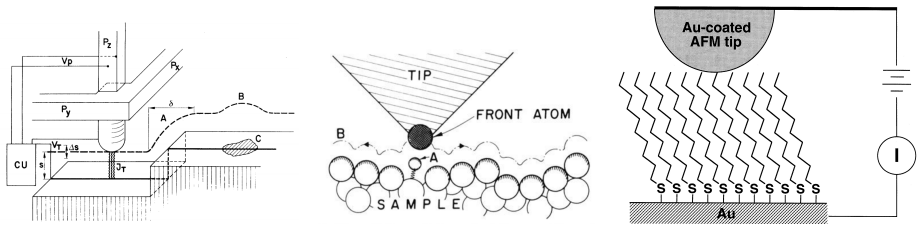


**Figure 1.3** Development of scanning probe microscopy (SPM) techniques. The scanning tunnelling microscope (left), atomic force microscope (middle), and conducting probe AFM (right). *Adapted from references [4, 5, 65].*

methods in molecular electronics today [67]. In this experiment, a gold tip is driven a few angstroms into a gold substrate to form a metallic nanocontact. Then the tip is withdrawn, until a short chain of gold atoms is left. During this process, the number of parallel conductance channels decreases stepwise, as indicated by the horizontal plateaus at integer multiples of the quantum of conductance ($G_0 = 2e^2h$) [68]. The schematic illustration in panel A shows the last remaining conductance channel. Upon further retraction, the gold contact is broken, which results in a sharp conductance drop where quantum tunnelling takes over (note the red box, which zooms in to a fraction of the conductance). This tunnelling scenario is depicted in panel C, where molecules are present in solution. These molecules can bridge the gap that is left between the two metal electrodes, which results in characteristic steps in the traces (indicated by the red arrows). When no molecules are present in solution (panel E), no steps are present after breaking the gold contact. Each trace depicted here corresponds to withdrawing the tip away from the surface once, but the approaching steps that reform the gold contact are not shown. Thousands of these traces are then compiled into histograms, where integer multiples of the conductance quantum each show a peak (panel B). Thus, the horizontal plateaus in A make up the vertical counts in B. Similarly, the molecular steps in panel C give rise to peaks in the histogram presented in panel D, where the first peak corresponds to one molecule, the second to two, and the third to three. No peaks are observed below the conductance quantum when no molecules are present (panel F).

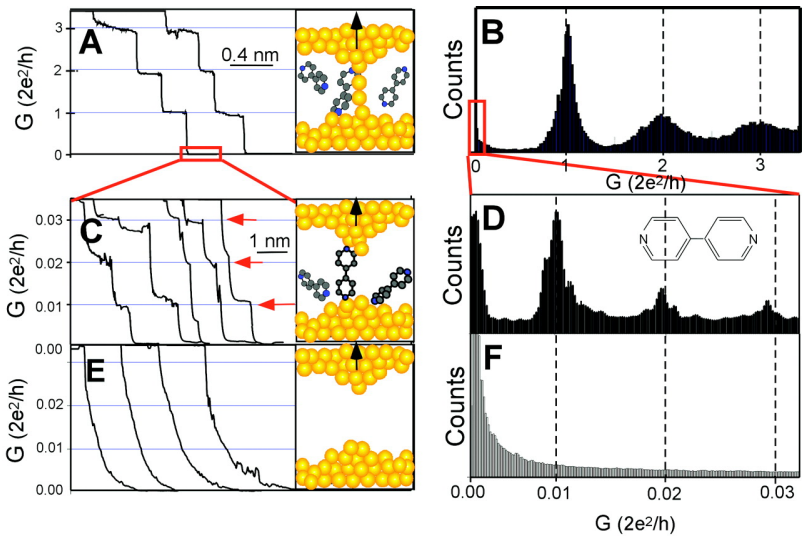


**Figure 1.4** Schematic illustration of the STM break-junction method. *Adapted from reference [67].*

The units of conductance quantum have become the standard when presenting break-junction data, as it provides clear and reproducible internal standard for each experiment.

In the same year, Haiss et al. published both the current-distance method , generally referred to as I(s) (or fishing) [69], and current-time method called I(t) or blinking [70], see Figure 1.5. Both of these STM techniques do not form a metallic contact between the tip and the substrate. As a result, the current range remains in the tunnelling region at all times and can thus be plotted on a linear scale. In the I(s) method, conductance is measured as a function of distance just like in the break-junction method described above. In this case, though, the STM tip is placed at a fixed distance from the sample by means of a current setpoint value (panel A on the left in Figure 1.5). The tip is then pulled away from the surface, resulting in a typical exponential conductance-distance trace indicated by the blue arrow. When molecules are present on the surface, the tip can contact one and pull it up as the tip is withdrawn. This scenario is shown in the cartoon, where the fully extended molecular junction (panel D) gives the conductance value of the molecule. In

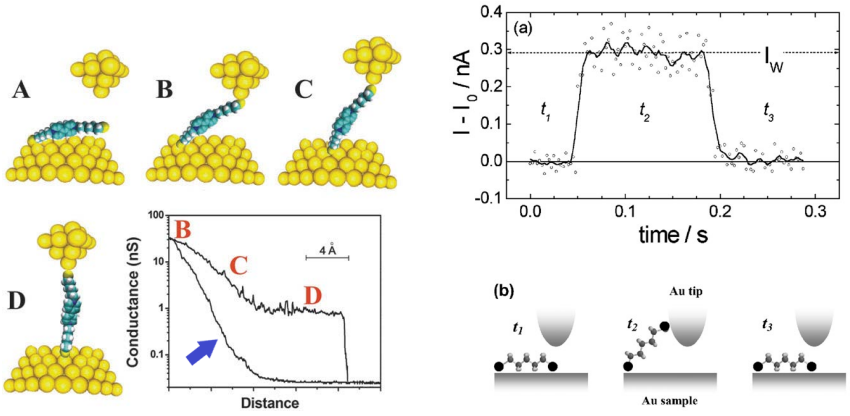


**Figure 1.5** Schematic illustration of non-contact STM techniques. The current-distance (left), and current-time method (right). *Adapted from references [70, 71].*

the I(t) method, the STM tip is also placed at a fixed distance from the surface, but here the tip is not pulled away from the surface. Instead, the current is recorded continuously over time, while stochastic binding and breaking events between the molecules and the tip occur (see schematic at the bottom right of Figure 1.5). These binding events result in characteristic current jumps in the current-time plots, as shown in the top right. The difference in current can then be translated into the conductance of a single molecule. The I(t) method is particularly useful for studying systems where tip-sample contact is best avoided, such as semiconductor-molecule-metal junctions (and also metal-protein-metal junctions). This will be discussed in detail in chapter 5. Until today these current spectroscopy techniques and their variations are among the most widely used for studying single-molecule conductance, and are a simple yet effective starting point for studying many molecular systems.

## 1.4 Molecular anchoring groups

The anchoring groups of the molecule chemically connect to the two electrodes to close the nano-electronic circuit. The nature of this interaction strongly influences the electron transmission through the junction. This dependence is

mainly determined by two factors. First, the densities of states at the relevant energy levels of the electrodes and the molecular anchoring groups. And second, the relative position for each of these energy levels, see Figure 1.2 on page 5. A stronger coupling, $\Gamma$, between the electrode orbitals and the frontier molecular orbitals results in more hybridisation, and therefore increased transmission probability. Likewise, the difference in energy, $\Delta E$, between electrode Fermi levels and frontier molecular orbitals shifts the probability curve of the transmission and therefore changes the area and thus the magnitude of the transmission. The effect of anchoring groups is one of the themes addressed in chapter 5.

### 1.4.1 Types of anchors

Sulfur has become an important atom in anchoring groups due to numerous studies on the gold-sulfur bond in multiple research fields. It is straightforward to synthesise molecules that contain sulfur moieties, which contributed to its popularity for molecular transport studies. However, multiple possibilities for the binding geometry between gold and the thiol group, in particular, have made it challenging to interpret transport data. This is because histograms that are constructed from thousands of traces show a broad set of possible conductance values, see below.

In addition to anchoring groups that contain a sulfur atom to bind to the metal electrodes, other suitable atoms include nitrogen [72], phosphorus [73], and carbon [74–76]. Numerous research groups have contributed to the rich knowledge on contact chemistry in molecular electronics, where a selection of key resuts is presented in Figure 1.6. The top panel shows a study by Chen et al., who found that not only the single-molecule conductance values are affected by the type of anchoring group, but also the decay length, $\beta$ [16]. Moreover, they found that the contact resistance also strongly depends on the type of anchoring group, where the resistance trend is thiol $<$ amine $<$ carboxylic acid. This result can be seen in the plot by extrapolating the lines to the points

corresponding to N=0 methylene units.

The bottom left panel in Figure 1.6 shows how Park et al. studied how anchoring groups affect the conductance histograms for molecular wires of the same type [73]. They found that for all three anchoring groups that they studied, the conductance histograms are relatively narrow, indicating that the variation between junctions is relatively low. They also found that the contact resistance is the lowest for molecules terminated by the phosphine group (blue curve), followed by the methyl sulfides (red curve), and finally the amines. This trend comes from a combination of bond-strength and orbital size.

In contrast, the conductance histograms for the thiol group are significantly broader as shown in the bottom right panel of Figure 1.6. Here, Hong et al. used conjugated molecular wires rather than alkanes, which leads to higher overall conductance values, but similar trends in contact chemistry [77]. They indeed found that the broad histogram for the thiol group stems from the multiple binding configurations that are found upon fully stretching the metal-molecule-metal junction. They also found a higher stability and junction formation probability for pyridine and thiol when compared to the other two groups, which they attributed to more possible geometries and a higher binding energy.

## 1.5 The molecular backbone

In this section, chemical modifications of the molecular backbone and how they affect the junction properties are discussed. Here, the focus will be on the intrinsic junction design, i.e. the direct wire-like connection between the electrodes. External factors are then covered in the next section, where different types are split into three distinct categories. The concept of molecular diodes (rectification) can be considered as intrinsic junction design, but since it is studied as a function of bias voltage, it will be part of the section on external parameters below. Rectification is one of the themes addressed in chapter 5.

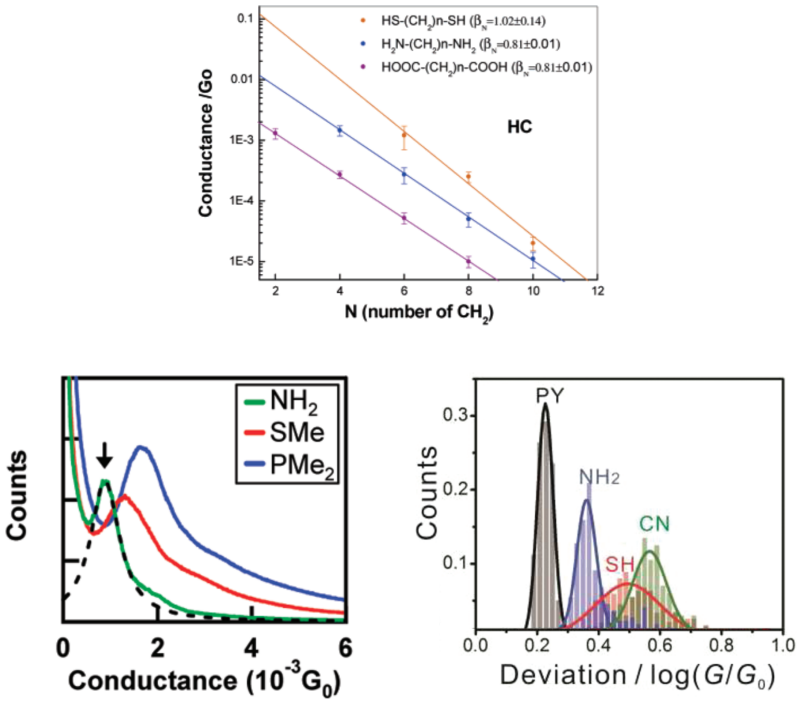


**Figure 1.6** Effect of anchoring group on molecular conductance. Top: comparison of length-dependence for three series of alkane wires terminated with different anchoring groups. Bottom: two separate studies on the effect of the type of anchoring group on junction conductance values. *Adapted from references [16, 73, 77].*

### 1.5.1 Conjugation

Perhaps the simplest example of chemical functionality along the bridge is $\pi$-conjugation. Here, the carbon chain that comprises the molecular backbone has alternating single and double bonds. The double bonds have $\pi$-orbitals in addition to $\sigma$-orbitals, whereas saturated molecules only have single bonds from $\sigma$-orbitals. The carbon atoms of such molecular wires are essentially repeating units, $CH_2$ for saturated, and CH for conjugated wires. Each repeating unit can be considered a single-level model that is wired in series. The $\pi$-orbitals on the conjugated wires increase the electronic coupling, $\tau$, between each level. This broadens the transmission function, which increases its area under the bias window and thus the current. If the bias voltage stays the same, the con-

ductance also goes up [78]. An important result of this is that the relationship between conductance and length changes as discussed below.

## 1.6 Beyond the junction

As highlighted in the Scanning tunnelling spectroscopy section on page 11, the most basic experiments yield conductance information as a function of either electrode separation or time. Let us now shift our attention beyond the structure of a junction as depicted in Figure 1.2 on page 5. The environment around the junction represents a vast area of different concepts within molecular electronics. It includes the effects that external factors can have on the junction, such as solvents, temperature , pH, and more. In addition, it covers active control over the junction properties, such as switching effects. And in this discussion, although less common, it also includes tools to gauge the properties of a molecular junction, such as inelastic electron tunnelling spectroscopy (IETS), and how a thermal current can be measured as a function of temperature difference between the two electrodes. The external factors or environmental effects are divided into three distinct categories here. First, in subsection 1.6.1, the conductance as a function of other quantities is discussed. This allows for important relationships to be studied. For example, each mechanism for electron transport has a distinct correlation between conductance and quantities like temperature, bias voltage, and molecular length. The second category contains methods for gauging properties of the junction other than conductance and is covered in subsection 1.6.2. This category includes parameters that directly relate to the transmission probability, and thus the conductance. For example, thermopower measurements reveal the molecular orbital that dominates electron transport. But also studying barrier shape and size falls into this category, as well as work function of the electrodes and energy level positions of the molecules using ultraviolet photoelectron spectroscopy (UPS) [79]. The third category is discussed in subsection 1.6.3 and focuses

on active junctions and switching them between high and low conductance states using different external stimuli. Studying mechanical effects in molecular electronics is a bit tricky because it can belong to all three categories. As a function of electrode separation (piezo modulation), to probe barrier shapes, and also to switch between high and low states.

### 1.6.1 Dependence of conductance

In this section, the dependence of conductance on specific quantities is addressed. These studies give valuable insights into junction properties.

#### Length and Temperature

Although technically part of the bridge, the length of the molecule in a junction is included in this section because it is most often studied as a function of conductance. There are two aspects to the relationship between conductance and length. First, the mechanism for electron tunnelling depends on the width of the tunnelling barrier, and therefore on the length of the molecules. The second is the tunnelling decay factor, $\beta$, which is also called the conductance attenuation factor. For coherent tunnelling, this decay has an exponential dependence on length, and it is a measure for the electronic coupling along the backbone of the molecular wire. When the transport mechanism changes to hopping, the dependence of conductance on length becomes much less. A pioneering study by Seong et al. showed this transition in a series of oligophenyleneimine (OPI) molecular wires of different lengths [80], see Figure 1.7.

### 1.6.2 Gauging properties beyond conductance

Measuring the electrical response of molecular junctions provides tremendous information, which is required for their application in electronic devices. However, many other properties of these nanoscale systems are critical along the way to realise this aim [81]. An excellent review on single-molecule properties besides

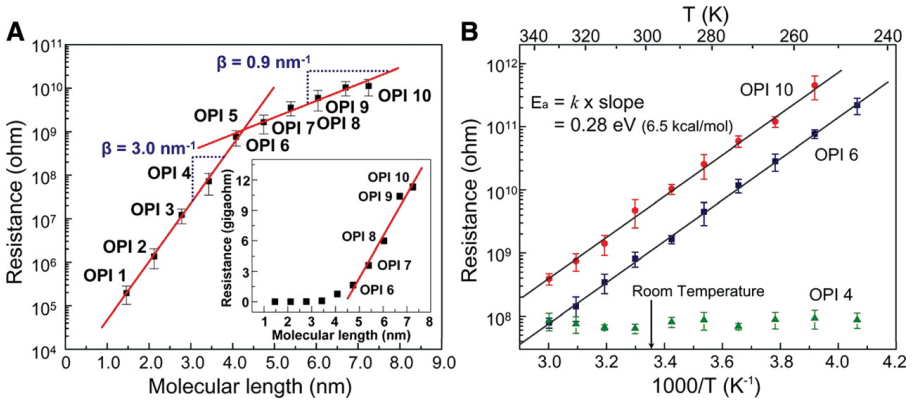


**Figure 1.7** Effect of molecular length on conductance. *Adapted from reference [80].*

conductance was published in 2013 by Aradhya et al. [82]. Specific topics covered in this review include optical characterisation [83], mechanical effects [84], thermoelectricity [85], and magnetism [86]. Among optical characterisation tools, Raman spectroscopy is the most widely used technique at the nanoscale level [87]. The reason for the limited use of other common optical methods is because the optical resolution is roughly around the micrometre scale.

One technique that is suited particularly well for the molecular scale is inelastic electron tunnelling spectroscopy (IETS) [88]. This is because it measures the interaction between the transporting electrons and the vibrational modes of the molecule. The results provide information on the types of molecular orbitals and thus the nature of the interaction between the molecular anchoring group and the electrode [89]. A study by Song et al. from 2009 showed how the IETS signal could be enhanced by tuning the orbital alignment using a gate voltage [90].

A different way to align the molecular orbitals, thereby tuning the charge transport, is by using the mechanical modulation tools of the atomic force microscope [91]. One of the first single-molecule electromechanical studies was carried out by Xu et al. [92]. They found that the strength of the gold-sulfur bond is comparable to the metallic gold-gold bond, which means that the gold-alkanedithiol-gold junction breaks at either bond with roughly the

same probability. They also measured alkanediamines in the same study, but the gold-nitrogen bond is much weaker, indicating that the junction almost always breaks at the gold-nitrogen bond.

Temperature measurements provide valuable information about the mechanism of charge transport by verifying how the conductance depends on the temperature (a case of category I as described in subsection 1.6.1 above). However, temperature plays a key role in several other ways. For example, the thermoelectricity is the current produced by a molecular junction in response to a temperature gradient across the electrodes [85]. In other words, one of the electrodes is hotter than the other. By plotting the magnitude of this current as a function of the difference in temperature, the thermopower can be extracted. This is valuable because the sign of the thermopower depends on the molecular orbital that dominates electron transport [93]. This line of research could see sensing applications in the nearer future [94]. Studying heat transport more generally has recently received attention through atomic contacts [95] and molecular junctions [96].

Another powerful electronic characterisation tool, which does not directly measure conductance, is transition voltage spectroscopy (TVS) [97]. This technique quantifies the alignment between the molecular energy levels and the Fermi level of the electrodes [98]. On a final note, tools to identify and manipulate molecules at the single level include orbital imaging [99] and even catalysis of chemical reactions [100, 101].

### 1.6.3 Molecular switches as active components

So far, only passive molecular wires and the effects that the resulting junctions display have been discussed. For applications of architectures based on transistors, the junction conductance needs to be switched between a high conductance "ON" state, and a low conductance "OFF" state [102].

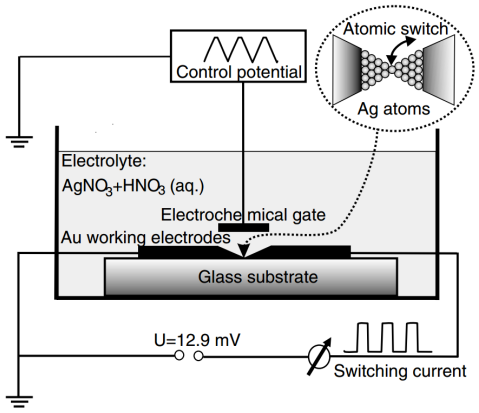


**Figure 1.8** Schematic illustration of a quantum switch using the electrochemical control. *Adapted from reference [103].*

### Gating

An attractive method for achieving such a transistor-type setup is by using electrochemical control in the form of a third electrode near the junction, called a gate electrode. It effectively controls the amount of current that flows through the main path of the junction. This configuration is the working principle of a commercial silicon transistor. A nanoscale example of this system is the metallic switch presented by the Schimmel group, see Figure 1.8. They used electrochemical control to form and break repeatedly a nanometallic silver contact [103]. In this case, the "ON" state is the quantised conductance of the silver metal chain, and the "OFF" state is the electrolyte-containing gap after electrochemically breaking the metal chain. Although not a molecular switch, it is a clever way to avoid the disadvantages of the electromigration technique.

## 1.7 Summary and outlook

Understanding tunnelling mechanisms is a key aim in molecular electronics because it enables fine control over device fabrication and the resulting device properties. Important tools for revealing these mechanisms involve studying

the dependence of junction conductance on quantities like temperature and voltage. The specific details of different mechanisms are discussed in chapter 2. Other tools give valuable information about junction architectures too, such as transition voltage spectroscopy (TVS) for estimating tunnelling barrier heights, or thermopower for determining the molecular orbital that dominates the transport pathway.

## 1.8 Thesis outline

This introduction chapter focused on the history and development of the field of molecular electronics and discussed important contributions made by numerous research groups. The rest of this thesis is structured according to Table 1.1. I will first give a brief introduction to nanoelectronics theory in chapter 2. This chapter will start by highlighting theoretical concepts of both tunnelling and transport mechanisms, followed by the computational methods for calculating transmission functions. I will then cover experimental details in chapter 3 by listing the materials and sample preparation, followed by data collection and analysis. This chapter will conclude by highlighting the individual contributions of colleagues and collaborators involved with my thesis work.

As discussed in the previous sections, different parts of the metal-molecule-metal junction contribute to the electrical transport through a junction. In chapter 4, I will discuss the chemical manipulation of the molecular backbone using metal atoms. After that, I will shift the focus from the bridge to the electrode, and discuss indium tin oxide as electrode material in chapter 5. The last results chapter is chapter 6 in which I will discuss the design of three different types of molecular wires. The first is based on a nonlinear metal cluster, the second involves efforts to form junctions using a new metallic anchoring group, and the third is a wire that contains the optically switchable dihydropyrene (DHP) moiety. Finally, conclusions are summarised in chapter 7.

**Table 1.1** Thesis outline by chapter.

| Chapter | Details | Page |
|---|---|---|
| 1 Introduction | Literature review | 1 |
| 2 Theoretical background | Quantum tunnelling<br>Electron transport<br>Calculations | 25 |
| 3 Materials and methods | Sample preparation<br>Experimental setup<br>Data analysis<br>Contributions | 35 |
| 4 Organometallic molecular wires | Results | 47 |
| 5 New anchoring groups for ITO | Results | 68 |
| 6 Complex architectures | Results | 83 |
| 7 Conclusions | Summary and Outlook | 91 |

# Chapter 2

# Theoretical background

*"The task is... not so much to see what no one has yet seen; but to think what nobody has yet thought, about that which everybody sees."*

— **Erwin Schrödinger**

## 2.1 Introduction

Theoretical concepts in the field of nano-electronics best start from a schematic representation of a simple resistor, see Figure 2.1. Here, the black squares represent a bulk metal as the electron reservoirs, which are connected to a power supply, in theory providing infinite electrons. In a simple and macroscopic case, the reservoirs and the channel have dimensions on the scale of millimetres and are all the same material, e.g. copper. We then have a classical, Newtonian bulk metal wire. The properties of such a wire are straightforward to describe using Ohm's law, which is given by

$$I = \frac{V}{R}, \tag{2.1}$$

where $I$ is the current, $V$ is the voltage, and $R$ the resistance. When we move down in scale several orders of magnitude, we enter the dimensions of mesoscopic physics, where many introductory descriptions for the electrical properties start from the Drude formula, which describes the resistor (or conductor) in terms of electron mobility. In this picture, the electrons are said to flow due to the electric field. However, when moving to smaller scales, this approach becomes less intuitive. Therefore, another way to look at a resistor is using the concept of a ballistic device. In this case, the electrons flow from one lead to the other without losing any momentum. It was first described by Landauer, and can be written as

$$G = G_B \frac{\lambda}{L + \lambda}, \tag{2.2}$$

where $G$ is the conductance, $G_B$ is the ballistic conductance, $\lambda$ is the mean free path, and $L$ is the length of the channel. Here, the bulk reservoirs can be viewed as being connected to nano-scale electrodes when we move closer inwards to the edge of the channel between the reservoirs. At these length scales, Equation 2.2 describes quantised conductance through our channel, which is now a small

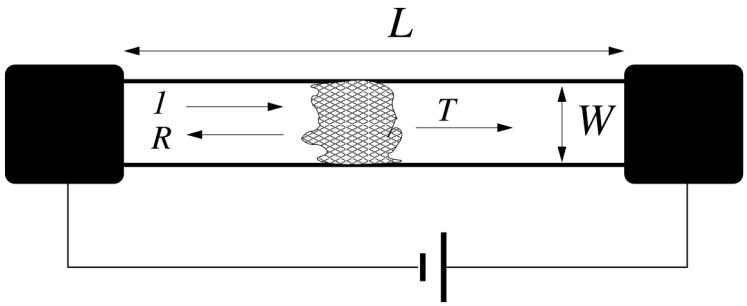


**Figure 2.1** Schematic illustration of a resistor. *Adapted from reference [104].*

chain of metal atoms. When the last atoms in the chain break, we enter wave probabilities of electrons tunnelling across the newly formed metal electrode contacts, see discussion below. These electrodes can be obtained through several experimental procedures, as described in chapter 1. Regardless of how the contacts are formed, most commonly they are made of the same metal. This is also convenient in the theoretical picture, since the density of states, and therefore the Fermi energies, will be the same for both contacts. Breaking down the numerous concepts that make up the field of molecular electronics, and presenting them in a clear and chronological way, is a challenging task. This is because quite a few different perspectives can be taken to explain phenomena from the broader fields of chemistry, physics, and quantum mechanics. One approach is to take scale as the main lead, and the discussion would move from macroscopic bulk material properties down to the nano-scale dimensions. There are important environmental effects to discuss as well, most notably bias voltage, temperature, and distance between the electrodes. These factors play a key part in the mechanism for conductance.

In the rest of this chapter, I will start by presenting the concept of quantum tunnelling using Schrödinger equations, which can be applied to any metal-insulator-metal junction. Next, I will discuss the scenario in which a molecule enters the system to obtain a metal-molecule-metal junction and how it relates to the transmission probability of electron flow. Several mechanisms for electron

transport are highlighted here as well. Finally, I will give a basic introduction to modelling systems using density functional theory.*

## 2.2 Quantum tunnelling

Quantum tunnelling happens when the metallic nano-contacts in our ballistic resistor break and leave a small gap to form a metal-insulator-metal junction. The conductance drops below the conductance quantum, and we enter the realm of wave probabilities. This depends on the distance between the electrodes, see below. The width of the insulator (or the gap) increases and is proportional to the barrier width of a potential barrier. When the barrier width becomes sufficiently large, coherent tunnelling is no longer possible, and other mechanisms take over. Likewise, when the bias voltage becomes very large, other mechanisms also start dominating. On the other hand, when the applied bias is small, the rectangular shape of the potential barrier from the previous section is a decent approximation. However, as the bias voltage increases, the tunnelling barrier takes a trapezoidal form. In addition, when a molecule is in the junction, the electronic structure of the molecule complicates matters more. The Simmons model is a good approximation when describing simple systems. In this case, the length L in our schematic picture represents the distance between two metallic contacts. In classical mechanics, the electron is

* In the fields of molecular— and nanoelectronics, the terms 'theory', 'calculations', and 'computations' are often used interchangeably. However, there is an important distinction between 'theory' and the other two. Theory is generally based on mathematical frameworks to describe certain phenomena, usually capable of predicting the outcome of a specific physical system. On the other hand, calculations (or computations) are computer algorithms that use specific theoretical models to simulate experiments and obtain predictions for how a system behaves. Therefore, calculations are usually preceded by the theory, which provides the equations needed in the calculations. However, experiments can and often do happen before the theory and thus, the calculations. Regardless of whichever comes first, when in agreement, the three branches of science complement and strengthen each other. The difference between 'calculations' and 'computations' is that the noun 'calculations' is more common, and the adjective 'computational'. This is also how I will use these terms throughout this work.

treated as a particle and can be described by

$$E = \frac{p^2}{2m} + U(x). \tag{2.3}$$

The potential barrier $U$ has a width of $x$, $E$ is the energy of the electron, $p$ is its momentum, and $m$ is its mass. This equation does not have any solutions for $E < U(x)$ and thus, the electron cannot penetrate the barrier. In the quantum mechanical case, electrons are treated as waves, and the wave function is given by the time-independent Schrödinger equation

$$E\psi(x) = -\frac{\hbar^2}{2m}\frac{d^2}{dx^2}\psi(x) + U(x)\psi(x). \tag{2.4}$$

The potential barrier $U$ still has a width of $x$, and the wave-function $\psi$ is a function of $x$. This equation does have a solution for when $E < U$ and is given by

$$\psi(x) = \psi(0)e^{-\kappa x}, \tag{2.5}$$

with

$$\kappa = \frac{\sqrt{2m(U-E)}}{\hbar}. \tag{2.6}$$

The solution for the case of $E > U$ is given by

$$\psi(x) = \psi(0)e^{ikx}, \tag{2.7}$$

with

$$k = \frac{\sqrt{2m(-U+E)}}{\hbar}. \tag{2.8}$$

When we zoom out and look at the total picture of the wave approaching the potential barrier, tunnelling through, and emerging on the other side, the schematic picture is given in Figure 2.2. Here we can identify the following three important regions: I the incoming wave that approaches the potential barrier, II the potential barrier of width $x$, and III the wave has passed through

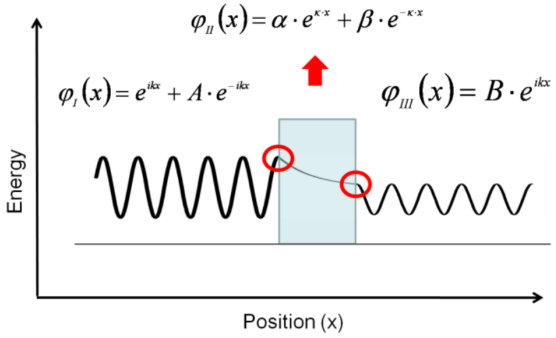


**Figure 2.2** Schematic representation of an electron tunnelling through a potential barrier. *Adapted from reference [105].*

the potential barrier. The time-independent wave-function of the electron takes the form

$$E\psi(x) = \left(-\frac{\hbar^2}{2m}\frac{\partial d^2}{\partial x^2} + V(r)\right)\psi(x), \tag{2.9}$$

where the three parts can be described by

$$\psi_I = e^{ikx} + Ae^{-ikx}, \tag{2.10}$$

$$\psi_{II} = \alpha e^{\kappa x} + \beta e^{-\kappa x}, \tag{2.11}$$

and

$$\psi_{III} = Be^{ikx}. \tag{2.12}$$

The decay constant outside the barrier is given by

$$k = \frac{\sqrt{2mE}}{\hbar}, \tag{2.13}$$

and inside the barrier it is

$$k = \frac{\sqrt{2m(\phi - E)}}{\hbar}. \tag{2.14}$$

The probability that an electron tunnels from region I to region III is given by

$$T = \frac{|B|^2}{|A|^2}. \tag{2.15}$$

The wave-functions have to match at the boundaries between the different regions.

## 2.3 Molecular transport

It is now convenient to expand our schematic of a resistor by adding different parts of the molecular junction. In this case, the tunnelling concept described in the previous section is best treated as the electron transmission* probability from a negative to a positive electrode. When looking at the schematic of a junction, either metal-insulator-metal, where the insulator can be vacuum, air, or a solvent, or metal-molecule-metal, the equation needs to be adapted to take into account the possible directions of the electron flow. The Hamiltonian operator can be used to describe this system as a combination of different parts by

$$\hat{\mathbf{H}} = \mathbf{H_{left}} + \mathbf{H_{right}} + \mathbf{H_{coupling}} + \mathbf{H_{backbone}}. \tag{2.16}$$

The first thing we need is an estimate for the density of states, and the position of the Fermi function. The source Fermi level is represented by $\mu_1$, the Fermi level of the drain by $\mu_2$, and applied the bias voltage is $qV$. Within the picture of elastic transport, where the electrons don't lose energy, we obtain the current expression

$$I = \frac{1}{q} \int_{-\infty}^{+\infty} G(E) \Big( f_1(E) - f_2(E) \Big) \, \mathrm{d}E. \tag{2.17}$$

* The terms 'tunnelling', 'transmission', and 'transport' are closely related and it can be confusing to distinguish the difference between them. Tunnelling specifically refers to the process of a particle wave (most commonly of an electron) moving through a classically forbidden barrier. Transmission describes the probability of the electron actually doing so. And transport is a more general term used to describe the mechanism of tunnelling and the corresponding current magnitude of the junction.

The energy $G(E)$ is at a specific value that is represented by the difference in Fermi levels of the contacts. This value is then averaged over multiple energy levels because each channel is independent of the next one, i.e. they are quantised. If we assume a small applied voltage, we obtain an expression for the conductance, which is given by

$$I/V = \int_{-\infty}^{+\infty} G(E) \left(-\frac{\partial f_0}{\partial E}\right) \mathrm{d}E. \tag{2.18}$$

The partial derivative of the fermi function with respect to energy yields the iconic Lorentz shape curve that represents the HOMO and LUMO in the literature. This is an average of the conductance function $G(E)$, which depends on energy. At low temperatures, the derivative of the Fermi function is very sharp, which means only the specific energy matters. At higher temperature Equation 2.18 needs to be averaged over an energy window on the order of $k_B T$. For example, at ambient temperatures, this is approximately equal to 25 meV.

$$G_B = q^2 \frac{D\bar{\mathrm{v}}}{2L} \tag{2.19}$$

Ballistic conductance is the Sharvin conductance, with a fundamental limit for $R_B$. The tunnelling current depends on the transmission and can be described using Landauer by

$$I = T(E)\Gamma_L\Gamma_R. \tag{2.20}$$

$$G = \frac{q^2 D}{2t} \tag{2.21}$$

G depends on density of states, which is given by

$$D(E) = \frac{1}{2\pi} \frac{\Gamma}{(E - E_0)^2 + (\Gamma/2)^2}. \tag{2.22}$$

The Landauer-Büttiker formula is given by

$$I(V) = \frac{2e}{h} \int_{-\infty}^{\infty} T(E,V)[f(E - eV/2) - f(E + eV/2)]\,\mathrm{d}E \tag{2.23}$$

With the Breit-Wigner formula describing the transmission by

$$T(E,V) = \frac{4\Gamma_L \Gamma_R}{[E - E_0(V)]^2 + [\Gamma_L \Gamma_R]^2}. \tag{2.24}$$

### 2.3.1 Mechanisms

Identifying mechanisms of electron transport in molecular junctions is an important goal as it allows for specific manipulation of new electronic functions. The first case to discuss is coherent transport, which means that electrons flow through the junction elastically. In other words, the phase of the wave-function before and after tunnelling remains the same. The first two mechanisms that are listed in Table 2.1 describe coherent transport, as their characteristic behaviour is that they are not temperature-dependent. Frisbie's group showed the transition between these two transport regimes experimentally using SAMs in metal-molecule-metal junctions [97]. The remaining two mechanisms listed dependent on temperature as they involve excitation and localisation, respectively.

## 2.4 Calculations

Density functional theory (DFT) is by far the most used technique for calculations in molecular electronics, which is based on Hamiltonian mechanics. These operators describe the total kinetic and potential energy states of a system using momentum vectors. A common approach is to first optimise (or relax) the geometry of a particular system using software packages like Gaussian. Next, transport properties are obtained by computing specific values of the transmission function at discrete energy intervals using Gollum or Smeagol. One significant limitation of DFT is that temperature is not included in the

**Table 2.1** Possible conduction mechanisms and their characteristics. $J$ is the current density, $V$ is the bias voltage, $d$ is the barrier width, $\Phi$ is the barrier height, $T$ is temperature, and $k_B$ is Boltzmann's constant. *Adapted from reference [3].*

| **Conduction mechanism** | **Typical behaviour** | **Temperature dependence** | **Voltage dependence** |
|---|---|---|---|
| Direct tunnelling | $J \sim Ve^{\left(-\frac{2d}{\hbar}\sqrt{2m\Phi}\right)}$ | none | $J \sim V$ |
| Fowler-Nordheim tunnelling | $J \sim V^2 e^{\left(-\frac{4d\sqrt{2m}\Phi^{3/2}}{3q\hbar V}\right)}$ | none | $ln\left(\frac{J}{V^2}\right) \sim \frac{1}{V}$ |
| Thermionic emission | $J \sim T^2 e^{\left(-\frac{\Phi - q\sqrt{qV/4\pi\varepsilon d}}{k_B T}\right)}$ | $ln\left(\frac{J}{T^2}\right) \sim \frac{1}{T}$ | $ln(J) \sim \sqrt{V}$ |
| Hopping conduction | $J \sim Ve^{\left(-\frac{\Phi}{k_B T}\right)}$ | $ln\left(\frac{J}{V}\right) \sim \frac{1}{T}$ | $J \sim V$ |

calculations, and thus the systems are treated as if at 0K. Another challenge is determining the exact position of the Fermi energy levels for the electrodes in question.

Simple and small molecules that are connected to common metal electrodes such as gold, are relatively straightforward to model using this approach. However, more advanced and longer systems require electron-electron (Coulomb blockade), and electron-phonon (inelastic transport) interactions to be taken into account. In these cases, a combination of, e.g. Poisson & Schrödinger equations need to be solved in a self-consistent manner.

# Chapter 3

# Materials and methods

*"Is it not ironic that we are doing research towards better circuit components using rubbish circuit components?"*

— **Inco J. Planje**

## 3.1 Introduction

The focus of this thesis is on experimental physical chemistry. Therefore, both synthetic procedures and theoretical calculations are not highlighted here.* This chapter starts by presenting the materials and chemicals that were used for experiments, followed by the details of sample preparation. Next, experimental methods and the acquisition of data are discussed, followed by analysis procedures and the presentation of results. The final section of this chapter contains a comprehensive overview of the contributions to this work that were made by colleagues and collaborators.

## 3.2 Sample preparation

Solvents were purchased from commercial sources: dichloromethane (DCM), hydrochloric acid, hydrogen peroxide, propylene carbonate (PC), sulfuric acid, tetrahydrofuran (THF), toluene, and 1,3,5-trimethylbenzene (TMB). The following compounds were also purchased from commercial sources: 44'-bipyridine (BP), potassium carbonate, and tetrabutylammonium hexafluoride (TBAF). All experiments and cleaning steps involving water were carried out using Ultrapure Millipore water of 18.2 MΩ (Milli-Q, MilliporeSigma USA, formerly Merck Millipore).

For *in situ* conductance measurements, molecular solutions of 1 mM were prepared in TMB if the compounds were sufficiently soluble. Less soluble compounds were dissolved in a mixture of TMB:THF, usually 4:1. Compounds **1Fe** and **1Co** in chapter 6 were insoluble in apolar solvents and therefore measured in PC using an insulated tip (see below). Compounds **2Fe** and **2Co**

* All compounds presented in this work were synthesised by collaborators. Transport calculations and some characterisation experiments were also carried out by collaborators. Chapter 4 of reference [106] contains synthesis details for some of the compounds, whereas others, as well as calculations, are included in manuscripts currently in preparation. Please contact the author for relevant updates.

were pre-adsorbed onto the substrates from 1 mM solutions in ethanol.

Liquid sample cells made out of polytetrafluoroethylene (Teflon) or polychlorotrifluoroethylene (PCTFE) were used for all scanning tunnelling microscopy (STM) experiments. Prior to each experiment, the cells were thoroughly cleaned by sonicating them in three steps, first immersed in piranha solution, then in Milli-Q water, and finally in acetone, ∼15 minutes each. Piranha solution was prepared by adding 30 w/w% hydrogen peroxide to concentrated sulfuric acid in a 1:3 ratio. ⚠ Caution—Piranha solution is a very strong oxidising agent and releases hazardous fumes. Never add hydrogen peroxide to concentrated sulfuric acid, always the other way around! Explosion risk when in contact with organic material!

All conductance experiments were carried out using STM gold tips, which were cut with scissors from a 99.99% pure gold wire 0.25 mm in diameter, purchased from Goodfellow Cambridge Ltd (England). For measurements carried out in polar solvents like PC, the tips were etched electrochemically and subsequently coated in Apiezon wax. The etching procedure is adapted from reference [107] and involves suspending the gold wire into a 1:1 mixture of hydrochloric acid:ethanol solution. A second gold wire is placed around the STM tip in a ring, touching the surface of the solution to form a meniscus. Both wires are connected to a power supply, where the STM tip acts as the anode and the ring wire as the cathode. Upon applying a potential of ∼5 V, gold at the anode dissolves into solution by reacting with chloride ions to form chloroaurate ions. The reaction continues for a few minutes until the bottom of the wire breaks off due to gravity and leaves behind a sharp, cone-shaped tip. The power supply is switched off, and the tip is rinsed with Milli-Q water and then coated with Apiezon wax. The wax is heated up on a fork-shaped soldering iron at 160°until it melts and the tip is pushed through the wax from the bottom with the sharp end. The coated tip is then pulled away horizontally and allowed to cool to room temperature before being mounted in the STM scanner.

For experiments involving gold-gold junctions, substrates purchased from

Arrandee GmbH (Germany) were used. These have a 250 nm gold (Au) layer on borosilicate glass with a 2.5 nm chromium adhesion layer in between. Before each experiment, the substrates were rinsed with acetone and then gently flame-annealed using a butane torch while placed on top of a silicon wafer to avoid bending of the glass. The substrate was heated until it started glowing bright orange, after which the flame is held for another ∼5 seconds before removing it and allowing the substrate to cool for ∼1 minute. This process is then repeated two more times, which yields large Au(111) terraces that are atomically flat [108]. For experiments with indium tin oxide (ITO) electrodes, glass substrates with a 40 nm layer of ITO were purchased from Präzisions Glas & Optik GmbH (PGO, Germany), and from SPI Supplies (USA) with a 700 nm layer of ITO. The PGO substrates were used as received, for testing and establishing optimal conditions, for STMBJ experiments on ITO, and for scratching a self-assembled monolayer of **A1** on ITO using atomic force microscopy (AFM). See Figure 3.1 for STM images of both gold and ITO surfaces. The substrates from SPI Supplies were cut into squares of roughly 12x12 mm with a diamond pen. They were then used for STM-I(t) experiments, after cleaning them according to the procedures in reference [109]. They were first sonicated in DCM for ∼20 minutes, then in methanol for another ∼20 minutes, and finally in a 0.5 M solution of potassium carbonate in a 3:1 mixture of methanol:Milli-Q water. The substrates were then immersed for ∼48 hours in 1 mM solutions of target molecules in 1:1 DCM:ethanol for STM-I(t)-i experiments (SAMs on ITO substrate), or mounted directly into the STM liquid cell in the case of STM-I(t)-ii experiments (SAMs on Au tip, see below). For the latter, molecules were adsorbed onto the gold STM tip under the same conditions, but for ∼12 hours. All STM-I(t) experiments were carried out in air, except for the measurement of wire **A3**, where TMB was added after adsorbing the molecules onto ITO.

The molar absorption coefficients, $\varepsilon$ (not to be confused with the energy offset $\varepsilon$, which has the same symbol), were determined by recording absorption spectra

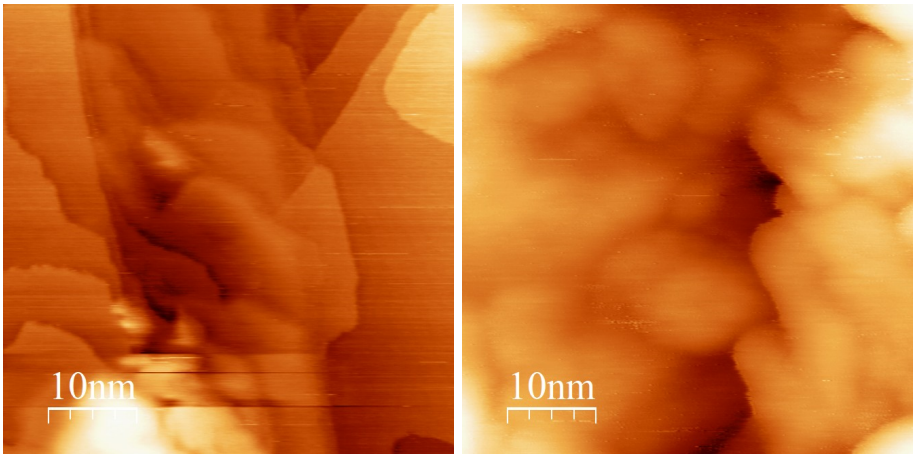


**Figure 3.1** STM images of Au surface (left) and ITO surface (right) at 50x50 nm.

of molecular solutions with a known concentration. The electrolyte solutions for all electrochemical measurements were prepared by making up 0.1 M of TBAF in DCM. Electrodes and cells for cyclic voltammetry (see below) were cleaned by sonication in DCM. For spectroelectrochemical (SEC) experiments, both solutions and OTTLE (optically transparent thin layer electrode) sample cells were prepared in a glove-box under nitrogen atmosphere. The OTTLE cell was rinsed several times with DCM before loading it into the glove box. Here, it was filled with the target compound dissolved in the electrolyte solution, after which it was taken out of the glove box and mounted into the spectrometer.

## 3.3 Experimental setup

Single-molecule conductance experiments were carried out using two separate STM setups dubbed 'Cerberus' and 'Leviathan'. Both operate a now discontinued Keysight Technologies 5500 SPM (formerly Agilent Technologies and originally developed by Molecular Imaging). 'Cerberus' was used for STM break-junction (STMBJ) experiments involving gold-gold junctions, with the exception of molecule **1Co** in chapter 6. 'Leviathan' was used to measure this molecule, for all STMBJ experiments on ITO substrates, and for all STM

current-time (STM-I(t)) experiments. In all cases, substrates were mounted into a liquid STM cell, and a few drops of 1 mM molecular solution was added for STMBJ experiments, and the SAMs on ITO were measured in air or TMB solvent for STM-I(t) measurements.

In STMBJ, the tip was repeatedly driven a few angstroms into the substrate and subsequently withdrawn several nanometres, all at constant bias voltage, retraction speed, and maintaining a fixed lateral position. The analogue current was recorded continuously during approach and withdrawal and fed into a current pre-amplifier, where the signal was converted into a digital voltage signal. This voltage signal was saved as raw data along with other relevant parameters, e.g. bias voltage and electrode separation. The voltage signal was also converted into units of conductance during the experiment and plotted into live histograms using a Python or LabVIEW interface ('Cerberus' and 'Leviathan', respectively). Data was saved as text files by controlling a toggle within these interfaces.

In STM-I(t) measurements, the tip was positioned a few angstroms from the substrate using a setpoint current of ∼5 nA. The feedback loop was then switched off to allow for fluctuations and jumps in the current to be monitored. Once the current was relatively stable, i.e. the baseline remains mostly horizontal (see section 3.4 below), segments of 0.5 seconds were saved as raw data regardless of whether any jumps were observed. Approximately 2000 of these traces were recorded for each experiment.

For the scratching of a SAM on ITO, the substrate was mounted into the AFM equipped with a silicon cantilever. The laser was aligned onto the centre of the photodiode before approaching. Once in contact, a surface image was recorded in contact mode using a force setpoint of 2 nN, followed by reducing the scan area to record a second smaller image in the centre of the first. This second image was recorded at a force of 10 nN, after which the first scan was repeated at 2 nN.

The electrochemical cell used for cyclic voltammetry was fitted with a platinum

disk (2.5 mm diameter) working electrode (WE), and a platinum wire (1.0 mm diameter) counter electrode (CE). A second platinum wire (1.0 mm diameter) was used as a pseudo-reference electrode (RE), together with internal reference compound decamethylferrocene (Fc*). The cell was connected to an EmStat2 potentiostat to control the cell potential. The target molecule and internal reference were added to the supporting electrolyte solution. After preparation in the glove-box, the OTTLE cell was connected to an EmStat2 potentiostat and mounted into the slit of a Cary 5000 spectrometer for ultra-violet visible (UV-VIS) measurements, or into a Cary 660 FTIR for infrared (IR). In both experiments, an open-circuit spectrum was first recorded when the potentiostat was switched off. A cell potential of 0 V was then applied, followed by recording a second spectrum. Next, the cell potential was increased by steps of 50 mV, recording a spectrum after each step, until the spectrum did not show any further changes. This process was then repeated in reverse order, i.e. decreases the potential in steps of 50 mV and again recording a spectrum after each step. All electrochemical data was saved as either ASCII or text files.

### 3.3.1 Troubleshooting

Undesirable experimental outcomes have two distinct origins. In the case of results that do not meet expectations, it makes no sense to blame instrumental failure. However, it does frequently happen that the system malfunctions, which should be verified. For example, to make sure that the electrochemical setup is working correctly, a sample of ferrocene can be measured. In the case of the STM, useful testing compounds include BP and simple alkanedithiols. Despite the STM working, challenges in taking measurements are still common. Sometimes it can take hours to stabilise the system, which is particularly relevant for the I(t) technique. More generally, constant changes in the nanoscopic environment invariably interfere with ongoing measurements. Therefore, data collection will have to be interrupted frequently to allow for system restoration. Tools to achieve this include moving the tip around the substrate, modulating

the piezo signal, applying a short and high voltage pulse through the tip, and changing the bias polarity. Including these steps using an automated procedure might be of interest.

Especially problematic for the STM are different types of solvents and its interactions with the sample molecules. Sometimes it is necessary to replace (or clean) the substrate and the tip several times to obtain one full dataset. Another more general solvent related challenge is the solubility of molecules in available solvents. For example, volatile solvents are unavailable because they can damage the instrument. It is also generally more straightforward to work nonpolar solvents as otherwise, the tip needs to be insulated to prevent high solvent currents. It is recommended to keep this compatibility in mind during synthetic design.

## 3.4 Data analysis

Raw STMBJ data was converted into conductance-distance traces using either a Python script ('Cerberus') or a LabVIEW routine ('Leviathan'). Only data corresponding to the withdrawal portion of the experiment was used for analysis, and the approach data is discarded. Several thousand traces were collected for each molecule and presented without selection in logarithmically binned conductance histograms. The analysed results of a 44'-bipyridine (BP) experiment are shown in Figure 3.2 as an example. Individual traces are presented in panel A, where black traces correspond to traces without a molecule, and grey traces are from Au-BP-Au junctions. In both cases, plateaus are observed at integer values of the quantum of conductance ($G_0 = 2e^2h$) as indicated by the red arrows [110, 111]. These steps correspond to atomic gold contacts and are particularly clear in the second black trace. The units are chosen to reflect these gold contacts as an internal reference to the break-junction experiment, e.g. $0\ log\ (G/G_0)$ corresponds to $10^0\ G/G_0$, which means $G = G_0$. Each integer step down on the axis then corresponds to a

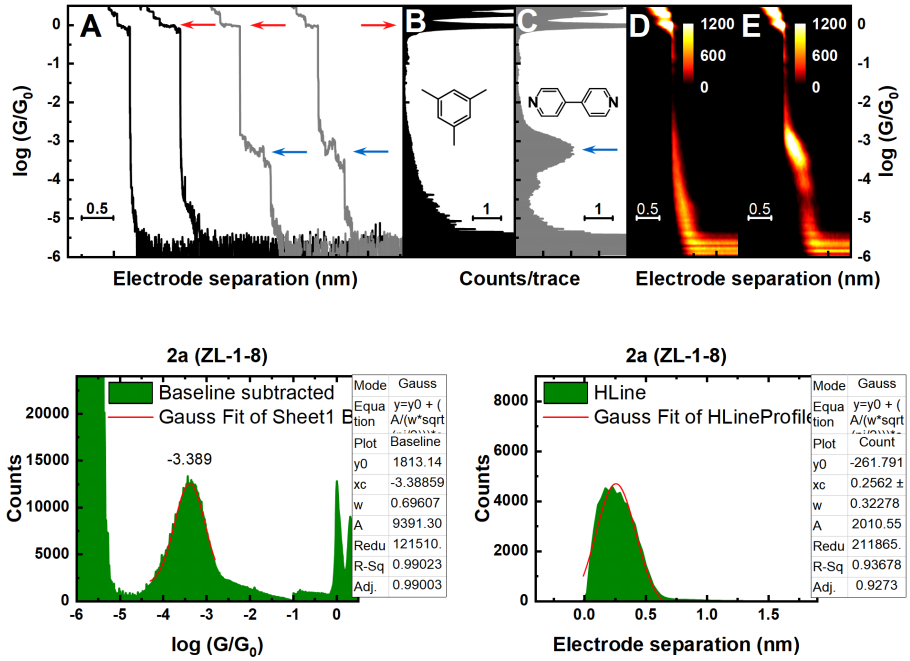


**Figure 3.2** STMBJ data of 44'-bipyridine (top). Single conductance-distance traces (A) without molecules (black) and with molecules (grey), the inset shows the molecular structure of BP. One-dimensional histograms of bare gold (B) and the molecule (C). Two-dimensional histograms of bare gold (D) and the molecule (E). Gaussian fits to the conductance (bottom left) and break-off data (bottom right) using molecular wire **2a** from chapter 4 as an example.

conductance value that is an order of magnitude lower than $G_0$, and the noise floor of the measurements is observed at $\sim 10^{-5.5}$ $(G/G_0)$. After the gold contact breaks, the conductance drops to the noise floor almost immediately due to the snapback effect (see chapter 4). In short, this leaves a gap between the electrodes, which is set by the analysis procedure as an electrode separation of 0 $nm$. When molecules are present in solution, they can bridge this gap to form a metal-molecule-metal junction, which results in a molecular plateau in the conductance-distance trace as indicated by the blue arrows. This means that BP has a conductance approximately 3 orders of magnitude below $G_0$. The one-dimensional (1D) histograms constructed from all traces are shown in Figure 3.2B (solvent only) and C (BP), with insets showing the structures of the solvent and the molecule. These histograms can be imagined as if the

x-axis in A was collapsed onto the y-axis as a single line, where the new x-axis corresponds to the total number of data points at any specific conductance value. This results in a sharp peak at the gold-gold contact as indicated by the red arrow in A that points to the right. In the case of molecules present in solution, the traces that show molecular features (like the grey ones in A) add up to show an additional peak in the 1D histogram, again indicated by a blue arrow. Figure 3.2D (solvent only) and E (BP) show two-dimensional (2D) histograms of the same data, which were obtained by storing both conductance and distance data using a density matrix. The counts in panel B and C are now represented by a z-scale as intensity. Average conductance values were determined by fitting the histogram peaks with Gaussian curves, see Figure 3.2 bottom left. Break-off lengths were obtained by first drawing a box around the molecular features in the two-dimensional histograms. Then the electrode separation counts were fitted with Gaussian curves, see Figure 3.2 bottom right.

Raw current-time traces from STM-I(t) measurements were loaded into a Python script to normalise the current jumps. This was done by establishing the baseline current, which usually corresponds to the setpoint value of the experiment, see Figure 3.3. The steps shown here were repeated for all traces with a reasonably flat baseline while discarding all traces that were too noisy. Approximately 300 traces (out of ∼2000) were processed for analysis, one example of which is shown in the right panel of Figure 3.3. Data points that fall below the zero current baselines are omitted from graphs. These traces were then compiled into histograms for determining the single-molecule conductance values of ITO-molecule-Au junctions.

All STM and AFM images were analysed and presented using WSxM software [112]. Spartan Wavefunction was used to draw 3D structures of the molecules, and determine the molecular length of compounds in chapter 4 as measured by the distance between sulfur atoms on either end.

Raw (spectro)electrochemical data was directly imported into Origin and

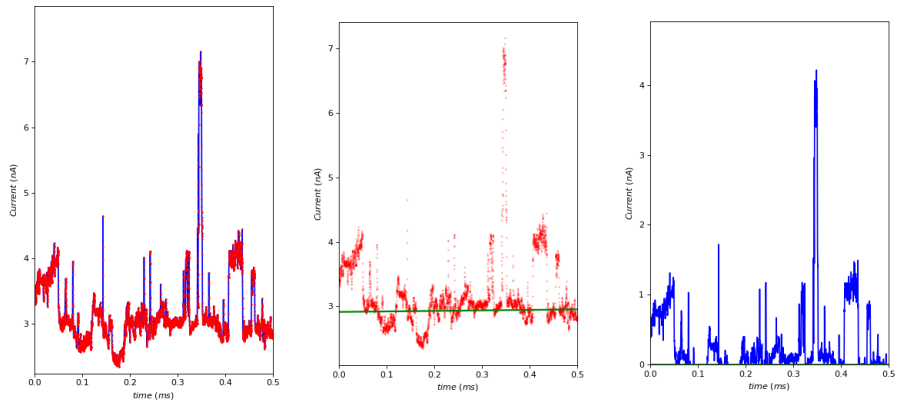


**Figure 3.3** Python routine for the analysis procedure of the STM-I(t) data. The current-time trace is loaded (left), then the background is determined (middle), and the resulting trace is saved (right).

presented without further analysis. Recorded oxidation potentials against Fc* were changed to the Fc scale. Peak current values were determined by drawing a baseline using LabVIEW programme eL-Chem Viewer [113]. For visual clarity, only a selected number of SEC spectra were included in figures.

## 3.5 Contributions

All of the work presented in this thesis has been part of ongoing collaborations of the molecular electronics research group at the University of Liverpool. In particular, without the hard synthesis work of the Low group in Perth and the Beeby group in Durham, no measurements could have been undertaken. Table 3.1 lists all contributions made to this thesis. Some of them are only discussed as text in the relevant chapters, with figures included in the appendices, and are therefore used as produced by the original authors.

**Table 3.1** Contributions to this thesis by colleagues and collaborators.

| Name | Location | Experiments |
|---|---|---|
| chapter 4: | | |
| David C. Milan | Liverpool | STMBJ of **3a**, **4a**, **4b**, **5a**, and **5b** |
| Sören Bock, Zakary Langtry, Masnun Naher | Perth | Synthesis of all compounds |
| Masnun Naher | Perth | Infrared spectroelectrochemistry & molar extinction coefficients |
| Oday A. Al-Owaedi | Lancaster & Hilla | Calculations (see Figure 4.10) |
| *Appendix only*: | | |
| David C. Milan | Madrid | Thermopower of **2b**, **3b**, **4b**, and **6b** |
| chapter 5: | | |
| Saman Naghibi | Liverpool | STM-I(t) of **A1**, **A2**, and **A3** |
| Ross Davidson (and students) | Durham | Synthesis of all compounds |
| *Appendix only*: | | |
| Santiago Martin Solans | Zaragoza | XPS, QCM, and CA of **A1**, **A2**, and **A3** |
| chapter 6: | | |
| Ross Davidson (and students) | Durham | Synthesis of **1Fe**, **1Co**, **2Fe**, and **2Co** |
| David C. Milan | Liverpool | STMBJ of **2Fe**, and **2Co** |
| Stephanie Beach | Boston | Synthesis of **FePt** |
| David Jago | Perth | Synthesis of **DHP** |

# Chapter 4

# Organometallic molecular wires

Parts of this chapter are published in:
D. C. Milan, A. Vezzoli, I. J. Planje, P. J. Low, "Metal bis(acetylide) complex molecular wires: concepts and design strategies", *Dalton Transactions* **2018**, *47*, 14125–14138, DOI 10.1039/C8DT02103A

*"We should be united in our uncertainty, not divided over fabricated certainty."*

— **Tim Urban**

## 4.1 Introduction

Metal atoms offer an attractive and vast toolbox for the design of molecular junctions [114]. In particular, transition metals are an interesting choice because of their electron-rich d-orbitals. Molecular wires that incorporate these electron-rich metal centres generally reduce the HOMO-LUMO gaps when compared to their organic equivalents (either simply omitting the metal atom, or putting a phenyl ring in its place).

In this chapter, I will discuss electrical and chemical properties of the molecular wires presented in Figure 4.1. I will start with a qualitative discussion of single-molecule conductance values, followed by a quantitative summary. I will then discuss electrochemical— and spectroscopic properties of the ruthenium wires. Next, I will discuss computational studies, thermoelectric properties, and finally, present an analytical interpretation of the trends that we found. This study is part of an ongoing collaboration between research groups in Liverpool (England), Perth (Australia), Lancaster (England), Hilla (Iraq), and Madrid (Spain). The full details of all individual contributions can be found in chapter 3.

## 4.2 Single Molecule Conductance

As described in chapter 1, the conductance of a molecule can be determined by trapping the molecule between two nano-sized metal electrodes using a bias voltage difference between the two electrodes. The corresponding current increase (when compared to tunnelling without molecules present) determines the conductance of the molecule under study. We used the STMBJ method to trap the molecules of interest and to build subsequent histograms from the current-distance traces. See chapter 3 for a detailed explanation of the features in the histograms, including data acquisition, and data treatment. Example conductance-distance traces for the four organic wires are presented in Figure 4.2A along with their corresponding histograms (B-E). The plateau features

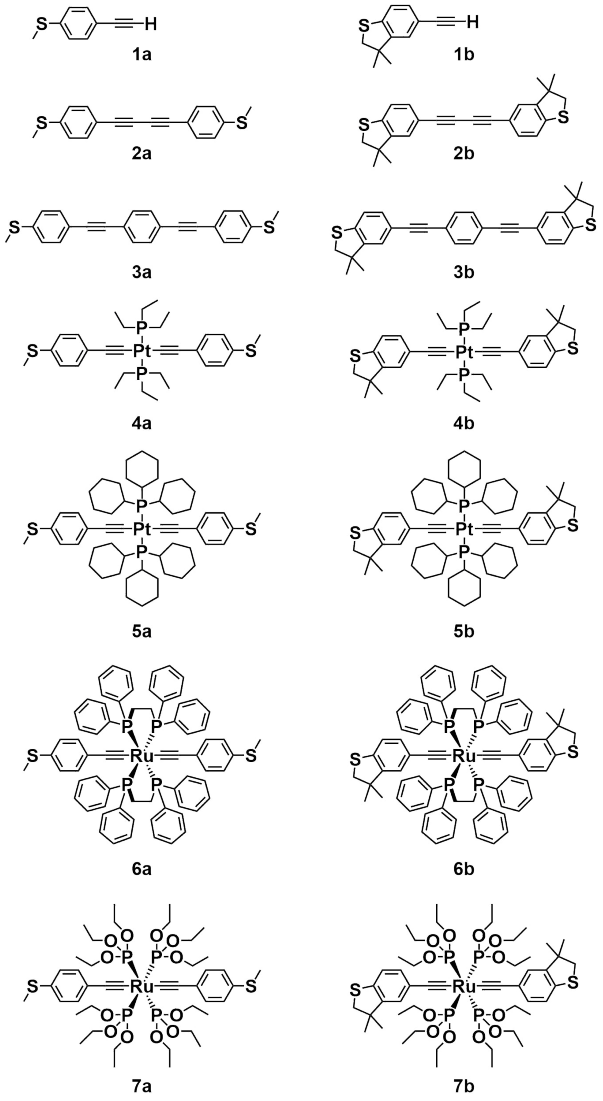


**Figure 4.1** Structures for the compounds studied in this chapter. The molecular wires are categorised by their anchoring groups, with thioether-contacted wires **a** on the left, and dimethylbenzothiophene-contacted wires **b** on the right.

that can be seen in the single traces around $\sim 10^{-3}$ are slanted. This is a result of electronic interactions between the conjugated backbone of the molecules and the metal electrodes as the junction is elongated. Directly following the 'snap-back' of the electrodes, the molecule bridges the resulting nano-gap with a tilted angle. This is because the molecules are longer than the separation between the electrodes. 'Snap-back' values for ambient STMBJ experiments

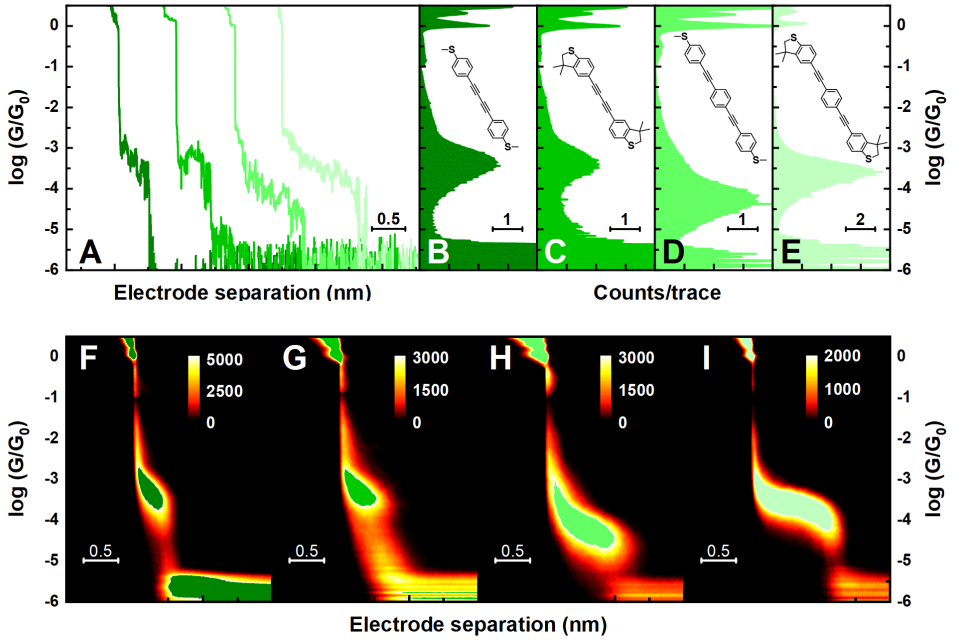


**Figure 4.2** Comparison of the four organic wires with example conductance-distance traces shown in **A**. From left to right; the first trace corresponds to wire **2a**, the second trace corresponds to wire **2b**, the third trace to **3a**, and the last to **3b**. In the same order, one-dimensional histograms for each wire are shown in **B-E** along with molecular structures, and two-dimensional histograms are shown in **F-I**.

range from ∼0.50 nm to to ∼0.65 nm using linear extrapolation [77] and push-back calibration [115], respectively. This interaction between the molecule and the electrodes then decreases when the separation between the electrodes increases, resulting in a substantial drop in conductance, which is seen as a slanted plateau. The conductance values for **2a** and **2b** are very close, which can be seen clearly from Figure 4.2B and C. This is not surprising given that the only difference is a slight variation in the geometry and binding of the sulfur atoms of the anchoring groups. That said, the conductance value for compound **3a** (Figure 4.2D) is surprisingly low when compared to the other three organic wires (Figure 4.2B, C, and E). At first sight, this result is not obvious since the difference in structure between **3a** and **3b** is not more prominent than the difference between wires **2a** and **2b**. However, the two-dimensional histograms

in Figure 4.2F-I provide more information about the junction evolution. For example, the shape of the histogram for wire **3b** stands out. It looks quite different from the others in that the junction conductance value does not change as much upon electrode separation. Only when the junction is approaching a fully extended configuration does the conductance drop considerably. This lower conductance value seems to compare better with the conductance value for wire **3a**. In other words, the one-dimensional conductance histogram for wire **3b** seems to be misleading because it provides an average over the separation range. Therefore, it may be better to compare the conductance values of fully extended junctions, see the discussion on transmission calculations below.

In comparing the break-off values in the two-dimensional histograms, at first sight, it looks like molecules **2** in Figure 4.2F and G are less extended in the junction than molecules **3** (Figure 4.2H and I). That is, the molecule has a higher tilt angle to the surface normal [116, 117]. However, tilt angles for all molecules are in roughly the same range, see further below. These also compare well with literature values for sulfur-gold bonds [118]. Another observation from the two-dimensional plots is that the hit-rate for wires **3** seems to be higher when compared to wires **2**. This is indicated by the absence of direct tunnelling traces, which is most clearly visible for wire **3b** in Figure 4.2I. Longer molecules tend to have a higher hit-rate in general, because they are easier to 'pick up' by the electrodes [119]. However, it is not clear why molecule **2b** has a lower hit-rate than **2a** (comparing Figure 4.2G to Figure 4.2F).

The series of platinum wires (**4** and **5**) are presented in Figure 4.3, with example conductance-distance traces in A, and their corresponding one-dimensional histograms in B-E. The conductance values for three out of four platinum wires are significantly lower than their organic counterparts in Figure 4.2, **5a** being the exception. Wire **4a** is much less conductive when comparing it to organic wire **3a**, even though it is slightly shorter (see Table 4.1 below). Likewise, both **4b** is slightly less conductive than **3b**, but **5b** is much less conductive. On the other hand, wire **5a** is slightly more conductive than its organic equivalent and

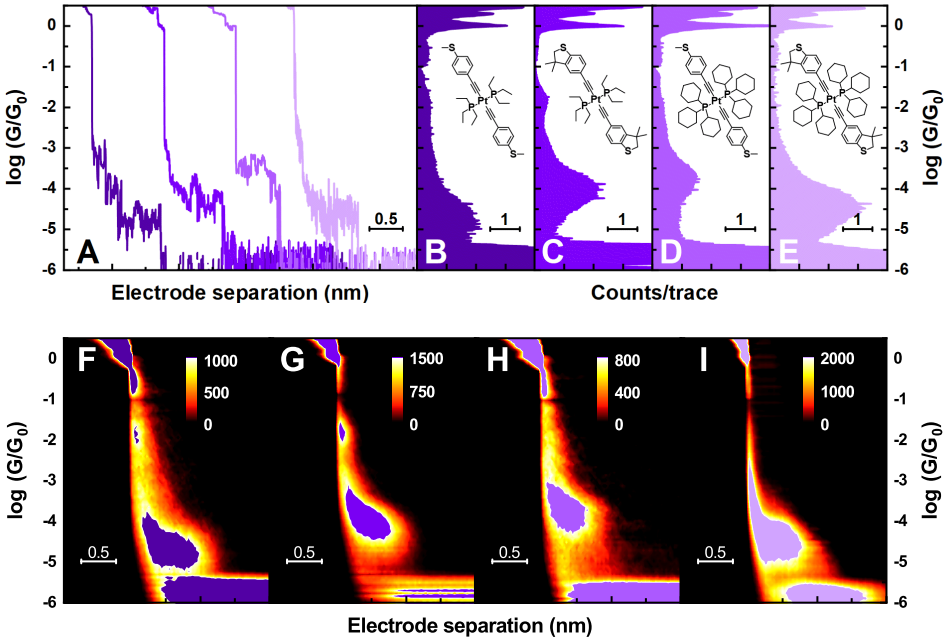


**Figure 4.3** Comparison of the four platinum wires with example conductance-distance traces shown in **A**. From left to right; the first trace corresponds to wire **4a**, the second trace corresponds to wire **4b**, the third trace to **5a**, and the last to **5b**. In the same order, one-dimensional histograms for each wire are shown in **B-E** along with molecular structures, and two-dimensional histograms are shown in **F-I**.

**3a**. These results are largely in contrast to recent studies of organometallic wires containing platinum metal centres. It is unlikely that this is a result of a weaker conjugation along the backbone of the molecules, as the platinum generally mixes well with the $\pi$-orbitals of the acetylide ligands. The molecule-electrode coupling also remains largely unchanged, as the anchoring groups are the same for the molecules being compared. However, the type of molecular orbitals dominating in the electron transport pathway might be altered by the anchoring groups used here, see further below. The hit-rates of the platinum wires are also generally lower than those of the organic wires, as can be seen from an increased number of direct tunnelling traces in Figure 4.3F-I. It is not completely understood why this is the case, but the steric hindrance of the ligands around the metal centre might make it more difficult for the molecule to

readily bridge the gap. The plateau features for the platinum wires seem to be less slanted when compared to the two-dimensional histograms of the organic wires. The reduced interaction between the electrodes and the backbones of the platinum molecules makes sense due to the saturated nature of their ancillary ligands. However, the conductance values are not straightforward to interpret, especially for wire **5a**. Subtle differences in electronic structure could be responsible for these observations, but more studies are needed to confirm this.

The two-dimensional histogram for molecule **4b** in Figure 4.3G shows an additional, smaller peak. We attribute this to trace amounts of the acetylide ligand that contains the anchoring group, molecule **1b** in Figure 4.1, which is left from synthesis procedures (see below for control experiments). Molecule **4a** shows a similar feature in Figure 4.3F, albeit a bit less pronounced. Here, it would be an impurity of molecule **1a** in Figure 4.1.

Figure 4.4 shows single-molecule conductance data for the ruthenium wires. Panel A presents example conductance-distance traces for wires (**6** and **7**), with their corresponding one-dimensional histograms in B-E. Conductance values for the four ruthenium wires have less spread than both organic— and platinum wires. This means that the ancillary (non-acetylide) ligands around the metal centre presented here have a minimal influence on the transport properties of the ruthenium wires. The two-dimensional histogram of **6b** in Figure 4.4G shows a higher hit-rate than any of the other ruthenium wires. Its plateau shape is also quite well-defined, with a relatively large break-off distance. In contrast, the two-dimensional histogram of **6a** in Figure 4.4F shows a large spread in its plateau features, i.e. a portion of the histogram shows a large break-off distance. But looking at the heat profile, a significant number of traces only show short plateau features. However, the hit-rate is also significantly lower, which makes it challenging to interpret the data. As a result, the break-off analysis in Figure A.9 has a very poor fit. This is likely a direct result of the experimental difficulties in measuring this molecule. It has very poor solubility

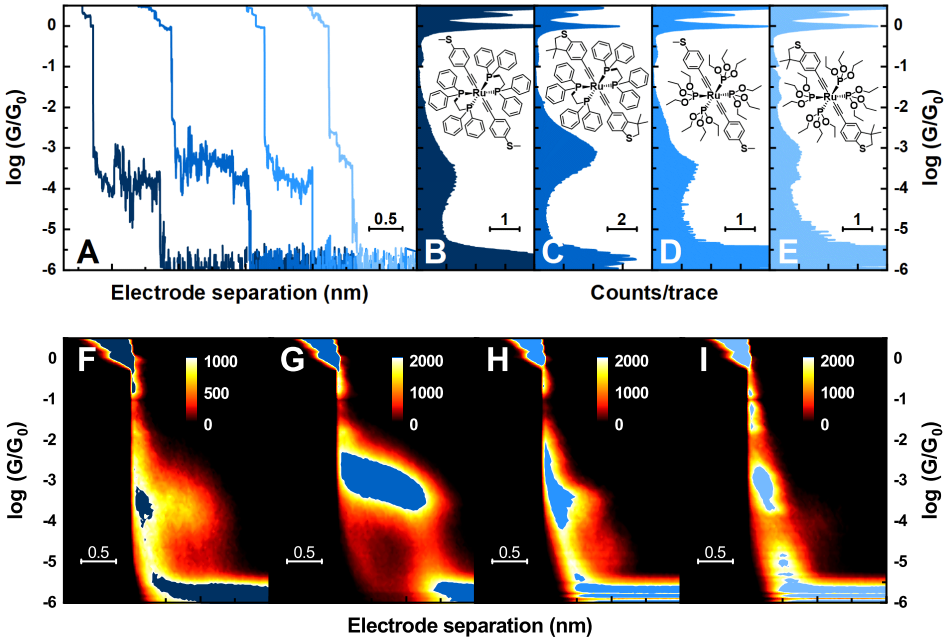


**Figure 4.4** Comparison of the four ruthenium wires with example conductance-distance traces shown in **A**. From left to right; the first trace corresponds to wire **6a**, the second trace corresponds to wire **6b**, the third trace to **7a**, and the last to **7b**. In the same order, one-dimensional histograms for each wire are shown in **B-E** along with molecular structures, and two-dimensional histograms are shown in **F-I**.

in organic solvents that are suitable for use in the STM (see chapter 3). This is one of the main reasons for turning to the phosphite moiety as ancillary ligands as it improves solubility significantly. In fact, wires **7** are soluble in mesitylene alone. Unfortunately though, the hit-rates and junction stabilities are not great, see Figure 4.4H and I. The histogram for compound **7b** also shows a smaller, secondary peak, similar compound **4b** in Figure 4.3G (see Control experiments on page 55 for details).

Conductance data for all wires in this chapter are summarised in Figure 4.5 and in Table 4.1. It is clear that the added metal atom in the centre has a pronounced effect on the conductance behaviour. However, it is not straightforward to draw simple conclusions from these results. For example, not all the metallic wires are higher in conductance than the organic series, as one

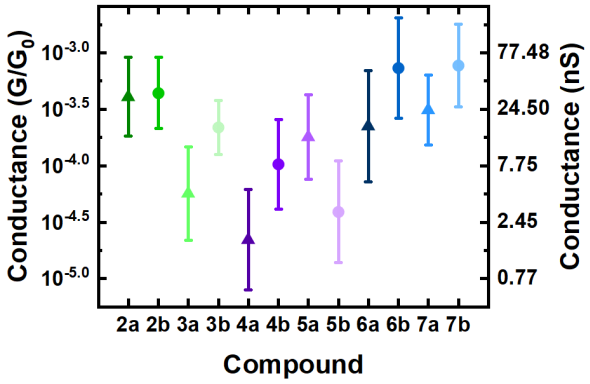


**Figure 4.5** Comparison of the conductance values for all wires. Organic wires in green, platinum wires in purple, and ruthenium wires in blue. Triangles are for SMe wires and circles are for DMBT wires. Error bars represent one standard deviation of the Gaussian fits, see appendix Appendix A.

might expect [120]. Quite surprisingly, the platinum wires seem to have a lower conductance overall. If we look only at molecular lengths (from crystallography data), we should not put too much emphasis on wires **2**. In this case, only one of the platinum wires, **5a**, surpasses the conductance of its organic SMe equivalent **3a**. Then all four ruthenium wires have a similar conductance 'boost' of about $4x$, comparing DMBT wires **6b** and **7b** to **3b**, and comparing SMe wires **6a** and **7a** to **3a**. It is also worth noting that even with a shorter molecular length, wires **2** are still lower in conductance than the DMBT ruthenium wires.

### 4.2.1 Control experiments

The shoulder peaks at high conductance that we found for some of the compounds have previously been attributed to ancillary ligands binding to the electrodes (in STM-I(s) experiments) [121]. To determine if that is also the case for the wires here, we measured one of the molecules containing only one acetylide ligand (with anchoring group). The other side has a chlorine bonded to the ruthenium instead, which is a common intermediate product in the synthesis of the *bis*-complexes. Figure 4.6A shows the two-dimensional histogram of **4a**

once more, for comparison to its *mono*-equivalent in Figure 4.6B. It is clear that the *mono*-Pt wire does not form any junctions. Only direct tunnelling, and some extra noise can be seen in Figure 4.6B. However, the anchoring groups **1a** and **1b** by themselves, do show distinct features at $\sim 10^{-2}$ G/G$_0$ (Figure 4.6C and D). Unfortunately, the hit-rate of these anchoring group molecules is quite low. The remaining parts of the histograms are also quite noisy. Therefore, it is unlikely that we will be able to use these systems elsewhere. Finally, using new batches of freshly purified molecules, we repeated some measurements that contained shoulder peaks. In most cases, the shoulders completely disappeared, but a small feature remained for others (such as **4a**). These control experiments confirm that the additional features at $\sim 10^{-2}$ G/G$_0$

**Table 4.1** Correlation of molecular length with break-off distance for all wires. [a]Determined from crystallography data ([†]estimated value) as measured by the sulfur-sulfur distance. [b]Break-off distances from statistical fitting (see appendix Appendix A), and a 'snap-back' value of 0.5 nm (*unreliable entry, see text for details). [c]Theoretical tilt angle of the molecule extended in the junction, calculated from $\cos^{-1}\left(\frac{\text{breakoff+snapback}}{\text{length}}\right)$.

| Molecule | Length (nm)[a] | Break-off + 'snap-back' (nm)[b] | Θ (deg)[c] | Conductance ($G/G_0$) | Conductance (nS) |
|---|---|---|---|---|---|
| **2a** | 1.57 | 0.76 | 61 | $4.1 \times 10^{-4}$ | 32 |
| **2b** | 1.57 | 0.81 | 59 | $4.4 \times 10^{-4}$ | 34 |
| **3a** | 2.01 | 1.10 | 57 | $5.6 \times 10^{-5}$ | 4.4 |
| **3b** | 2.00[†] | 1.14 | 55 | $2.2 \times 10^{-4}$ | 17 |
| **4a** | 1.85 | 1.12 | 53 | $2.2 \times 10^{-5}$ | 1.7 |
| **4b** | 1.84 | 0.96 | 58 | $1.0 \times 10^{-4}$ | 8.0 |
| **5a** | | 0.89 | | $1.8 \times 10^{-4}$ | 14 |
| **5b** | | 0.92 | | $3.9 \times 10^{-5}$ | 3.0 |
| **6a** | 1.86 | 0.83* | 64* | $2.2 \times 10^{-4}$ | 17 |
| **6b** | 1.85 | 1.17 | 51 | $7.4 \times 10^{-4}$ | 57 |
| **7a** | 1.86 | 0.80 | 65 | $3.1 \times 10^{-4}$ | 24 |
| **7b** | 1.83 | 0.72 | 67 | $7.7 \times 10^{-4}$ | 60 |

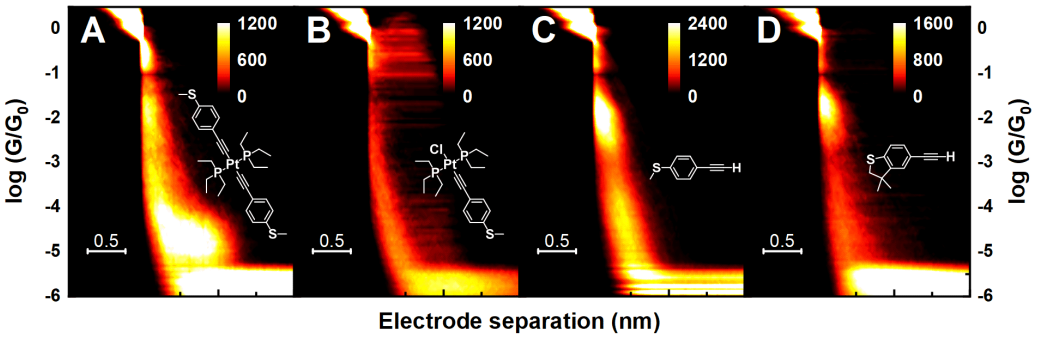


**Figure 4.6** Control experiments comparing compound **4a** in **A** to its *mono*-equivalent in **B** Panel **C** and **D** show two-dimensional histograms of the acetylide anchoring groups **1a** and **1b**.

came from synthesis impurities only, and not from ancillary ligand 'short-circuits'.

## 4.3 Electrochemical properties

The ruthenium molecular wires are redox-active, which means that they can be cycled reversibly between their neutral— and oxidised states. Their reversibility is confirmed by analysis of scan rates (see appendix Appendix A, and chapter 3 for details). Cyclic voltammograms for the ruthenium wires are shown in Figure 4.7. The internal reference decamethylferrocene shows a feature around 0 V in all cases. The more positive feature is the oxidation wave of the ruthenium compound. Oxidation potentials are highlighted on the graphs, and also summarised in Table 4.2. When comparing the ancillary ligands, the oxidation potentials of wires **6** containing the diphenylphosphine ligand appear to be lower than those of wires **7** containing the phosphite ligands. However, the comparison is more clear when comparing the molecules based on their anchoring groups. DMBT wire **6b** in Figure 4.7B is more easily oxidised than SMe wire **6a** in Figure 4.7A. And DMBT wire **7b** in Figure 4.7D is more easily oxidised than SMe wire **7a** Figure 4.7C. Next, phosphine wire **6b** is more easily

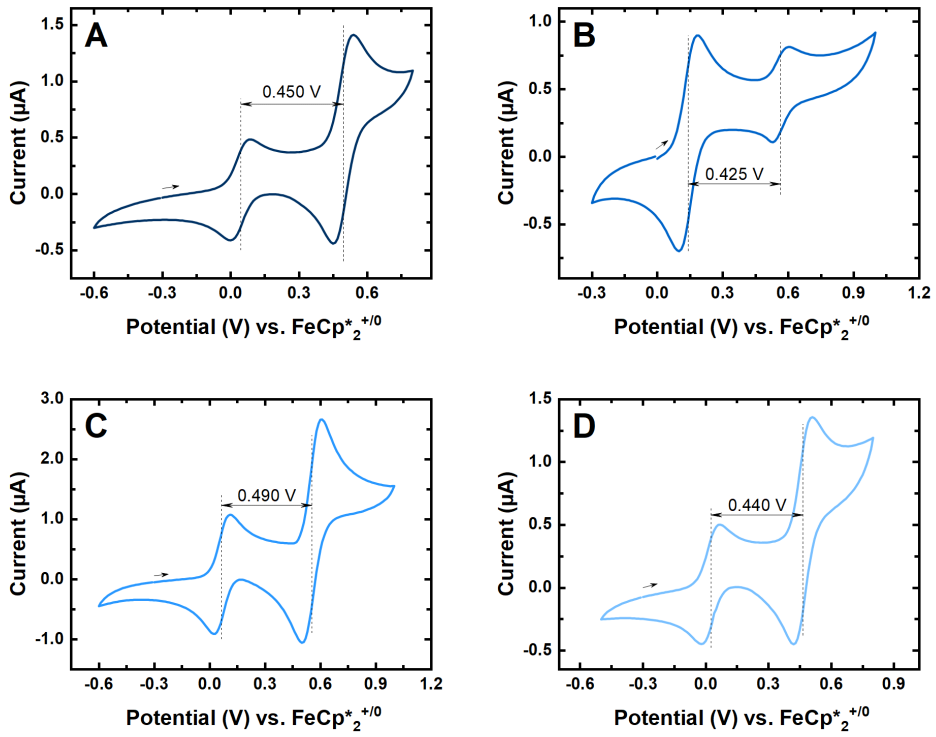


**Figure 4.7** Cyclic voltammograms for the ruthenium wires with their oxidation potentials listed against decamethylferrocene. **6a** (A), **6b** (B), **7a** (C), and **7b** (D). Arrows indicate sweep direction and starting voltage for all graphs.

oxidised than phosphite wire **7b**, and phosphine wire **6a** is more easily oxidised than phosphite wire **7a**. These observations indicate that the DMBT anchoring group is slightly more electron-donating than SMe, and also that the phosphine ligand is slightly more electron-donating than phosphite. Finally, comparing DMBT phosphite wire **7b** with SMe phosphine wire **6a** shows that the effect of the anchoring group is slightly greater than that of the ancillary ligand.

### 4.3.1 IR spectroelectrochemistry

Oxidation of the ruthenium wires was analysed by infrared (IR) spectroelectrochemistry, the results of which are shown in Figure 4.8, see chapter 3 for experimental details. The oxidation potentials needed to fully oxidise the species in the cell compare well to the cyclic voltammetry results. The neutral

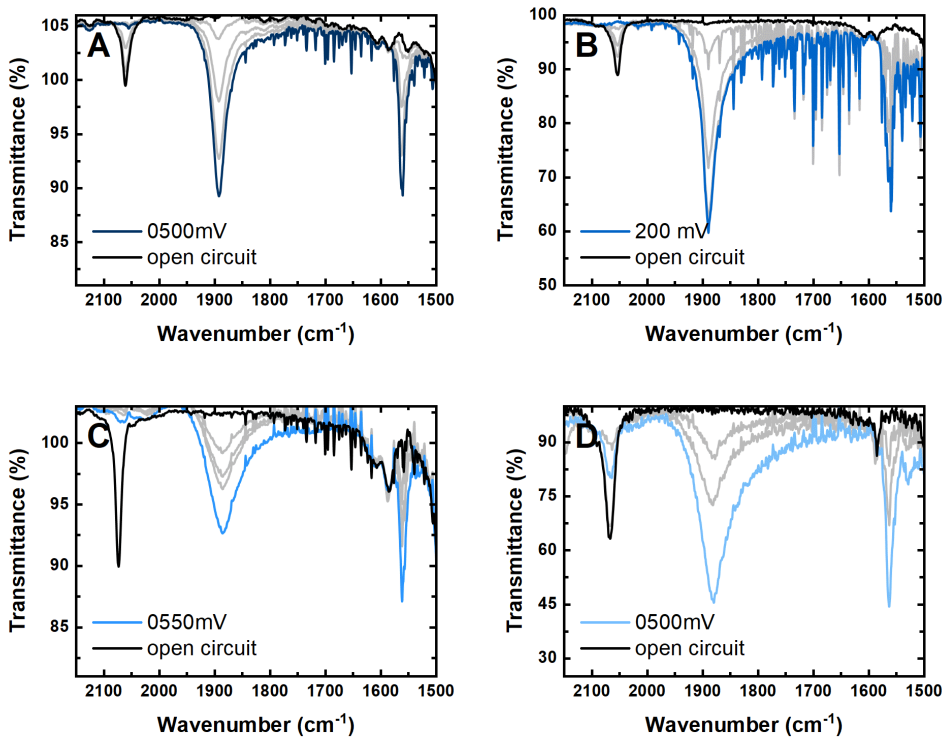


**Figure 4.8** Infrared spectra for the ruthenium wires **6a** (A), **6b** (B), **7a** (C), and **7b** (D). Neutral states represented by black lines, fully oxidised states in different shades of blue.

states of all wires, represented by black solid lines, show a pronounced peak around 2050 $cm^{-1}$. This mode corresponds to the C≡C vibrations. Upon stepwise potential oxidation, this band slowly disappears and is replaced by a broader, asymmetric band around 1900 $cm^{-1}$. This feature corresponds to a RuC≡C asymmetry in the electronic structure along the acetylide backbone

**Table 4.2** Oxidation potentials of ruthenium wires versus ferrocene.

| Molecule | Oxidation (V) | Versus ferrocene (V) |
|---|---|---|
| **6a** | 0.450 | -0.095 |
| **6b** | 0.425 | -0.120 |
| **7a** | 0.490 | -0.055 |
| **7b** | 0.440 | -0.105 |

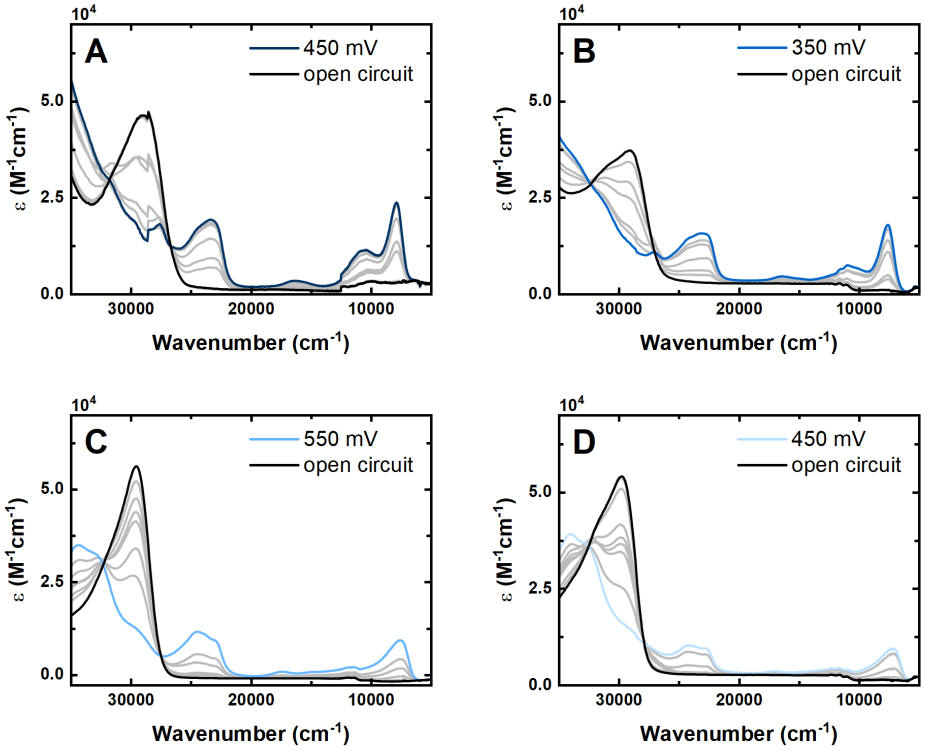


**Figure 4.9** UV-VIS spectra for the ruthenium wires **6a** (A), **6b** (B), **7a** (C), and **7b** (D). Neutral states represented by black lines, fully oxidised states in different shades of blue.

as a result of a delocalised positive charge. An additional feature around 1550 $cm^{-1}$ starts appearing upon oxidation, and corresponds to the breathing mode of the phenyl rings along the acetylide backbone.

### 4.3.2 UV-VIS spectroelectrochemistry

Oxidation of the ruthenium wires was also analysed by ultra-violet visible ultra-violet visible (UV-VIS) spectroelectrochemistry, see Figure 4.9. Refer to chapter 3 for experimental details. The oxidation potentials again correspond well with the cyclic voltammetry results. The neutral ruthenium compounds all show a clear UV absorption band around 30000 $cm^{-1}$ (~330 nm), black solid lines. Upon oxidation, this main band shifts to lower energies, due to a newly

available energy-level transition. This is because an electron is removed from the HOMO, raising its position and thereby decreasing the HOMO-LUMO gap. A second feature appears around 8000 $cm^{-1}$, which corresponds to the transition from the HOMO-1 to the newly accessible HOMO since this orbital is now missing an electron due to oxidation. The molar extinction coefficients, $\varepsilon$, are all in the same range. Note that the offset in energy levels between electrodes and molecules uses the same symbol, which is how this work also uses $\varepsilon$ outside this specific section.

## 4.4 Transmission calculations

Collaborators from the University of Lancaster have carried out electron transport calculations on the wires presented in this chapter (see chapter 3 for details). Figure 4.10 shows the calculated conductance values as a function of energy, for all the wires in Figure 4.1, except **5a** and **5b**. Just like in the experimental conductance data discussed above, the vertical axes show the conductance values in terms of $G_0$, where peaks in the transmission curves correspond to a higher conductance, and the troughs to lower values. The dashed vertical lines represent the Fermi energy levels of the electronic leads, which in this case are the gold STM tip and substrate. At applied bias voltages that are relatively small, as is the case in all experiments discussed in this work, the experimental conductance values correspond to a small symmetric area on both sides of the Fermi energy in the transmission plots. This area is also called the bias window and has the same numerical value as half the transmission energy in both directions. For example, an applied bias voltage of 0.2 V corresponds to a bias window in the transmission plot that goes from negative 0.1 eV to positive 0.1 eV. The area underneath the curve within this window is then integrated to give an average calculated conductance value.
In all cases, the peaks at negative values of $E$-$E_F$ correspond to the highest

occupied molecular orbitals (HOMOs) of the molecular wires, and the peaks at positive values correspond to the lowest unoccupied molecular orbitals (LUMOs). In the top left panel, ligands **1a** and **1b** do not have these peaks clearly defined, which is typical for short wires that are highly conjugated. These wires also show a relatively high conductance value around the Fermi energy, which is in good agreement with the experimental values shown in Figure 4.6.

One observation that stands out from these results is that the HOMO levels of wires **2**-**4** and **7** are approximately pinned to the same energy values around negative 1.2 eV (bottom four panels). Therefore, the shape and the position of the LUMO orbitals largely dictate the changes observed in the transmission curves around the Fermi level (dashed vertical lines). This result is intriguing because the HOMO orbitals dominate the conductance, as confirmed by thermopower results (see below). A notable exception to this observation is visible in the transmission curves for wires **6** (top right panel). In this case, the diphenylphosphine ancillary ligands (Figure 4.1) seem to have a more considerable influence on both the position of the HOMO and the shape of the LUMO. This interpretation would also explain the lack of differences that result from the anchoring groups, which is the case for wires **2**-**4**. A similar ligand effect is visible in the transmission curve for one of the triphenylphosphite wires (**7b** in the middle right panel). The two narratives discussed above might compete for these wires, where the distributed $\pi$-system dominates the transmission curve for **7a**, but the ligand dominates in the case of **7b**.

An important note here is to take some caution when drawing conclusions from these results. For example, discrepancies between transmission curves of wires **3a** and **3b** could arise from a difference in average junction geometry. This average overestimates the conductance for **3b** as discussed in the experimental section above. The geometry used in the calculations can be adjusted by applying so-called scissor corrections [122, 123]. Here, the positions of the HOMO and LUMO are shifted based on the optical band gap of the molecule measured by UV-VIS spectroscopy.

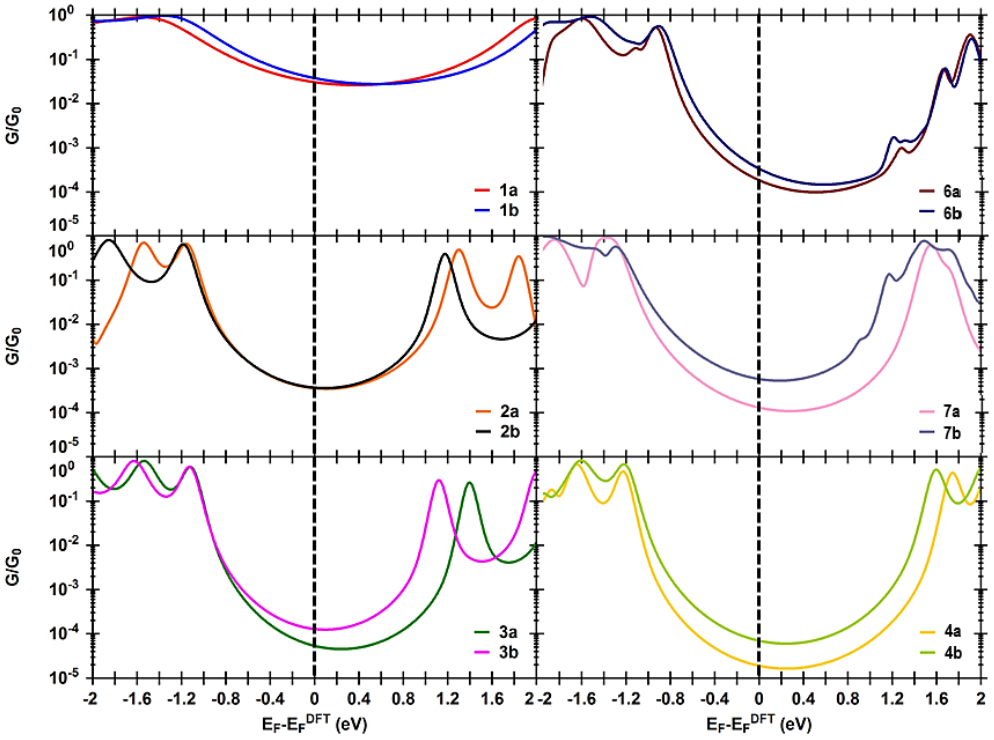


**Figure 4.10** Transmission calculations for all wires excluding **5a** and **5b**. Also note that the organic wires are all on the left, the ruthenium wires are displayed on the top right and middle right, and the platinum wires **4a** and **4b** are on the bottom right.

In all cases, the coupling between the molecule and the electrode significantly affects the transmission plot. This influence is most clearly visible in the HOMO peaks (at negative eV) of wires **4** (bottom right panel) and **6** (top right panel). In each of these two panels, the two overlapping transmission curves have the HOMO peaks that are closest to the Fermi level in the same position. However, the width of the peaks is greater for DMBT wires **b**, which increases the transmission close to the Fermi level. This broadening parameter $\Gamma$, which is a measure of the molecule-electrode coupling strength, has considerable influence on the conductance and is in good agreement with other studies [79].

## 4.5 Thermoelectric properties

Thermoelectricity in molecular electronics refers to the electronic response of a molecule when exposed to a temperature difference. The magnitude of the voltage is called the thermopower, which is expressed by the Seebeck coefficient S. The first effort to improve thermoelectric efficiency using nanoscale devices was carried out on thin films by Venkatasubramanian et al. [124]. Paulsson et al. gave a theoretical description of a single-molecule junction [13], and the first experiment to realise this thermoelectric effect in molecular junctions came from Reddy et al. [125]. In short, the magnitude of the Seebeck coefficient (thermopower), is proportional to the slope of the transmission function discussed in the previous section. That means that the thermopower is higher (at low bias) when one of the frontier molecular orbitals lies closer to the electrode Fermi level. Since the Seebeck coefficient is proportional to the negative slope, a HOMO conducting molecule has a positive Seebeck value, and a LUMO conducting molecule a negative one. The thermoelectric properties of a selected number of wires were measured, see Figure A.17. Small and positive values were found, which confirms HOMO conducting wires for which the centre of the transmission curves align with the Fermi level. This finding is in good agreement with the calculations presented in Figure 4.10.

## 4.6 Rectangular tunnelling barrier

Oxidation potentials can be used to obtain estimates for the position of the HOMO-orbital [126]. In light of the transmission picture discussed above, this provides useful information about the junction. However, merely plotting the conductance as a function of the orbital energies does not reflect the fact that conductance values are measured close to the electrode Fermi level. Therefore, oxidation potentials are taken together with the molecular length to fit the square tunnelling barrier model from Table 2.1 (direct tunnelling). In the case presented here, the molecular length estimates the barrier width and the

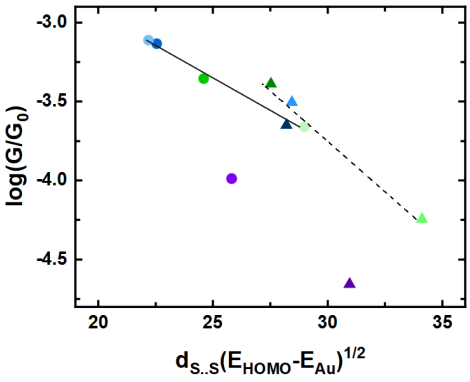


**Figure 4.11** Experimental conductance values as a function of $d_{S..S} \times (E_{HOMO} - E_{Au})^{1/2}$ for SMe wires **a** (triangles) and DMBT wires **b** (circles). The fitting parameter $E_{Au}$ is 2.4 eV for the SMe wires (dashed line) and 3.2 eV for the DMBT wires (solid line). Note that these fits do not include platinum wires **4** (purple data points).

energy difference between the HOMO and the Fermi level represents the barrier height [127]. Since the transmission calculations cannot accurately predict the electrode Fermi level, it acts as a fitting parameter here.

Figure 4.11 shows this correlation, with the molecular wires separated by their anchoring groups. Oxidation potentials for the organic wires **2** and **3** were approximated by $E_{3/4}$. Triangles represent wires **a** with SMe anchoring groups, with the dashed line showing a linear fit ($R^2 = 0.95$) through the data points for the organic and ruthenium wires. Likewise, the circles represent DMBT wires **b**, with the linear fit ($R^2 = 0.99$) marked by the solid line. The platinum wires **4a** and **4b** (in purple) lie quite far from these linear trends. The electrochemical data for the platinum wires significantly underestimates the tunnelling barrier height. Rather than a poor estimation for the position of the HOMO, more likely is that the tunnelling mechanism has a significant contribution from $\sigma$-orbitals [121, 128]. These orbitals are much lower in energy and thus lie farther away from the Fermi level, which means a lower conductance [127]. Note that compounds **5a** and **5b** are missing from this trend because no electrochemical data is available for these wires. Despite a clear correlation between conductance and electrochemical potentials, these trends emphasise

that a simple model like the rectangular barrier is not sufficient to describe the complex interactions of the systems under study.

## 4.7 Conclusions

This chapter has presented a series of organic and organometallic molecular wires, and a study of their electrical properties both experimentally and theoretically. Adding ruthenium centres to the molecular wires boosts conductance values by a factor of about two on average. The platinum wires studied here generally have a lower conductance value than their organic equivalents. This result is in contrast with similar platinum systems studied previously, and is likely a result of an increased $\sigma$-orbital (and decreased $\pi$-orbital) contribution to the frontier molecular orbitals. Electrochemical experiments confirmed these findings by providing estimates for the positions of HOMO-levels (which are $\pi$-orbitals). Fitting the electrochemical data to a rectangular tunnelling barrier reveals a trend for the organic- and ruthenium wires, but not for the platinum ones. However, deviations from this fit and limitations of this simple model, confirm the notion that the electrical properties of molecular wires result from a complex mix of different parameters. Key factors include the molecular length, the frontier-molecular orbital character (HOMO or LUMO) and position ($\varepsilon$), electron-electron interactions, electron-phonon interactions, and the molecule-electrode coupling factor, $\Gamma$. This last parameter shows the most significant influence on conductance, which is in good agreement both with theoretical calculations and other studies.

The work presented in this chapter confirms the importance of organometallic systems for molecular junction design. However, more work is needed to elucidate mechanisms and understand the intricate interplay of the parameters that make up the junction. The results presented here should be repeated using large-area junctions to establish if the single-molecule properties drasti-

cally change when studying assemblies of molecules. These scaling studies are indispensable for building device applications using molecular architectures.

# Chapter 5

# New anchoring groups for Indium Tin Oxide electrodes

*"Questions you cannot answer are usually far better for you than answers you cannot question."*

— **Yuval Noah Harari**

## 5.1 Introduction

For transistor type applications, molecules that can be switched rapidly between two different conductance states are required. An important method for controlling the junction conductance is optical modulation [129]. However, gold electrodes are not suitable for such experiments as they quench the light-induced excited states [130]. For this reason, transparent electrode materials such as tin-doped indium oxide, or simply indium tin oxide (ITO), have been studied in numerous research fields over the last few decades [131]. This material is important because of its combined conductivity and transparency. It is classified as a degenerate semiconductor, which means that the doping level (of tin) is high enough for the material to act somewhat like a metal. The structure of ITO is shown in Figure 5.1. The group of Tao showed that

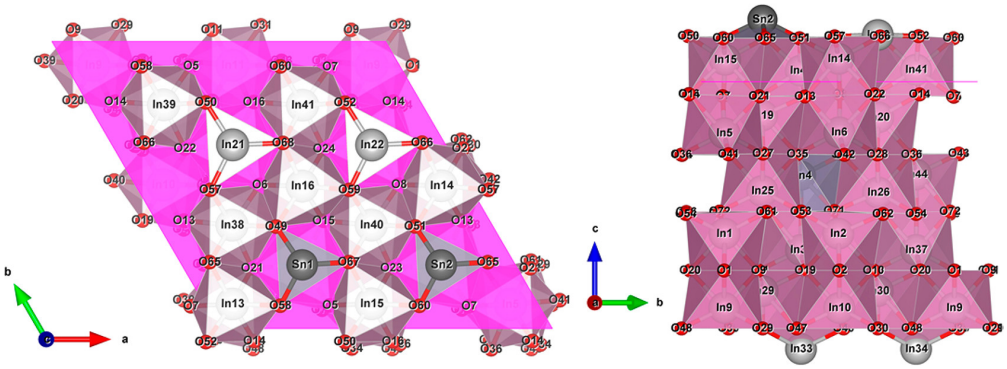


**Figure 5.1** Crystal structure of tin-doped indium oxide (ITO). *Adapted from reference [132].*

carboxylates are suitable anchoring groups for forming molecular junctions between ITO electrodes [133]. Lindsay's group later investigated an optically switchable molecular junction where the conductance was high under visible light illumination and low in the dark [134]. Other groups have used molecular monolayers of phosphonic acids and amino-silanes to modify surface properties of ITO [135–137]. However, to date little work has been done to investigate new anchoring groups for the formation of single molecule junctions using ITO.

This chapter will focus on a series of asymmetric tolane molecular wires presented in Figure 5.2, which we designed for the formation of Au-molecule-ITO junctions. As reviewed in chapter 1, the vast body of literature on the gold-sulfur bond in molecular electronics justifies the choice of a sulfur-containing anchoring group on one end of each wire. The other anchoring-group is expected to bind to ITO and will be the main focus of discussion in this chapter. I will start by presenting conductance data of Au-molecule-Au junctions measured using the STMBJ technique [67] for all the wires, which mainly serves as a rough evaluation of the molecules. Next, there will be a brief section on experimental challenges in forming Au-molecule-ITO junctions using current-distance spectroscopy. I will then narrow down the discussion of the molecular series to a few selected ones, which we evaluated on ITO substrates using current-time spectroscopy, known as STM-I(t) (see section 3.3 in chapter 3). We also carried out surface characterisation experiments of the molecules on ITO, which I will discuss after the conductance results. Finally, I will briefly touch on the difficulty of computational efforts before closing with the concluding statements and a note on future work to be done.

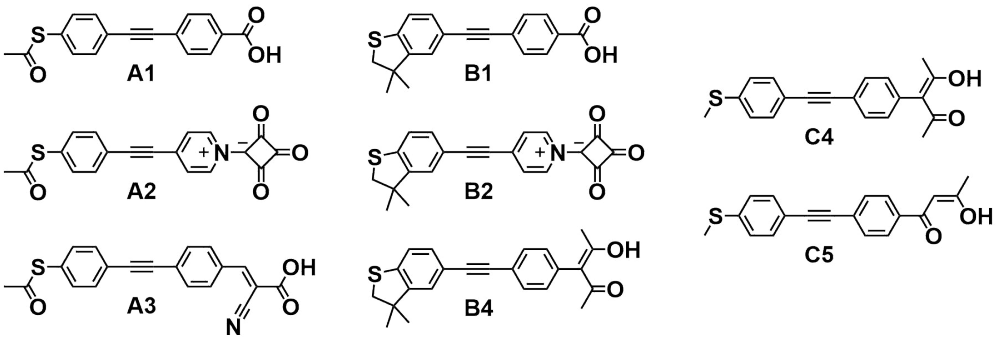


**Figure 5.2** Molecular structures for the compounds studied in this chapter. The molecular wires are categorised by their sulfur anchoring groups, with thioacetate-contacted wires **A** on the left, the dimethylbenzothiophene-contacted wires **B** in the middle, and the thioether-contacted wires **C** on the right. Numbers correspond to the anchoring groups designed for binding to ITO: carboxylic acid (**1**), pyridinium squarate (**2**), cyanobutenoic acid (**3**), conjugated acetyl-acetone (**4**), and cross-conjugated acetyl-acetone (**5**).

## 5.2 Au-Au break-junctions

Experimental challenges in forming *in situ* metal-molecule-metal junctions mainly come from limitations of solvents, see chapter 3. As a result, solubility is a key property to take into account when designing molecular wires for *in situ* junctions. Molecules **A** were the starting point of this study, due to their well-studied thiol anchoring groups. However, the solubility of these wires is not great in trimethylbenzene. Especially **A2** is poorly soluble in nonpolar organic solvents in general, which made it challenging to measure. In an effort to improve solubilities, and thus making measurements both easier and more reliable, wires **B** were added to this study. Additionally, these wires serve as a comparison to wires **A**, or as will be discussed below, can also complicate matters. Finally, wires **C** were added due to synthetic challenges in making a thiol-acetyl-acetone wire.

STMBJ measurements were carried out as a first step evaluation of the molecular wires. The resulting histograms are presented in Figure 5.3, where the wires are categorised by colour in terms of their ITO-anchoring groups. Blue histograms of carboxylic acid wires **1** are shown in Figure 5.3A-B. Red histograms in Figure 5.3C-D show data of the pyridinium squarate wires **2**. Figure 5.3E shows the histogram for the cyanobutenoic acid wire **3** in grey. Conjugated forms of the acetyl-acetone anchoring group are shown in green (Figure 5.3A-B), and finally the cross-conjugated acetyl-acetone wire **5** is shown in yellow in Figure 5.3H.

### 5.2.1 Carboxylic acids

It was a sensible choice to start this project by measuring the conductance of carboxylic acid wires, because of the body of literature available for the gold-carboxylate bond. However, the main issue with tolane wires is that their solubilities in aqueous environments are limited. Therefore, it is challenging to control the pH, and thus to ensure a negatively charged carboxylate group

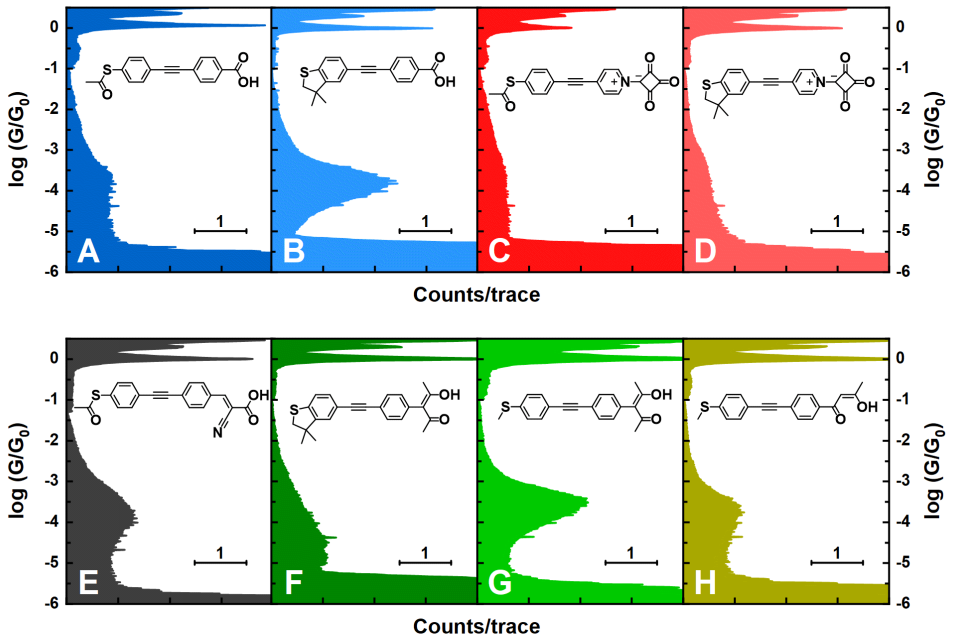


**Figure 5.3** One-dimensional conductance histograms of Au-molecule-Au junctions using the tolane wires presented in this chapter. Insets show the molecular structures for each histogram.

to bind to the gold electrode. Nevertheless, both molecules **A1** and **B1** do form junctions using gold electrodes as shown in Figure 5.3A-B. There is a remarkable difference in junction stability between the thiol wire **A1** and the DMBT wire **B1**. Since we know that the pKa values are similar, and therefore the behaviour of the proton in the carboxylic acid can be expected to be similar, this difference must come from the stability of the sulfur-anchoring group. Symmetric junctions using thiols on both ends of the molecule are known to be stable [16], but the DMBT anchoring group seems to perform even better [138]. The major difference in hit rate, i.e. counts/trace for the molecular peak (see chapter 3), indicates that the decreased rotation of the DMBT group significantly improves the junction stability [139].

### 5.2.2 Squarates

The pyridinium squarate wires **2** do not form any molecular junctions between gold electrodes as indicated by the histograms in Figure 5.3C-D. However, this anchoring group has been shown to bind to metal oxide surfaces [140].

### 5.2.3 Cyano

The cyanobutenoic acid wire **A3** is, in principle, similar to the carboxylic acid wires **1**. The difference is that its pKa value is lower because the electron-withdrawing cyano-group stabilises the deprotonated form of this molecule. In principle, this would mean that **A3** forms junctions more easily than wires **1**, because the proton is more weakly bound. However, as the behaviour of the junction is determined by several different effects, this is not the observed result.

### 5.2.4 Acetyl-acetones

Intuitively, it makes sense that the carbonyl oxygen does not bind to the metal electrode. We also know from [141] that the carboxylic acid anchoring group only binds to gold when it is deprotonated, and esters do not bind at all. Therefore, one might assume that the double keto forms of **B4**, **C4**, and **C5** are not expected to form any molecular junctions. With this in mind, then, the enol form is likely responsible for forming junctions and the explanation for the poor performance of **B4** could be that deprotonation of its enol form is less likely. However, the pKa values for **B4** and **C4** are similar, which indicates that there might be another reason for the observed results. In addition, the HOMO and LUMO levels of both compounds are nearly the same, see appendix Appendix B. In summary, because the results with the acetyl-acetone anchoring groups are inconclusive, we have decided to focus on wires **A1-3** for the ITO experiments that follow.

## 5.3 Au-ITO junctions

### 5.3.1 Current-distance spectroscopy

To obtain Au-molecule-ITO junctions experimentally, the non-contact I(s) method intuitively would be a good starting point. This is because it is difficult to maintain control over what happens at the nanoscale when crashing one material (gold) into a different one (ITO). However, in practice, it was not possible to obtain reliable current-distance data using the I(s) technique, because the tunnelling current fluctuated during the entire retraction cycle. The same effect was observed when trying to obtain break-junction data using similar retraction distances as with the gold-gold junctions. After moving to a different STM setup, the retraction distance could be increased significantly. Figure 5.4 shows conductance-distance traces using the amended STM setup for break-junction experiments with an ITO substrate and a gold STM tip. This figure shows very long slowly decaying current-distance traces of >20 nm. One reason for the long decay might be that filaments of the substrate are being pulled out upon retraction [142]. However, the Mohs hardness of gold is much lower than that of ITO. And even though this is a bulk parameter, a couple of simple STM tests described below suggest this property is (somewhat) retained at the nanoscale. High voltage pulses applied to the gold tip will expel atoms onto the ITO surface, but scanning the area directly after a pulse does not show any gold deposited onto the ITO. This is likely a result of the atoms being picked up by the tip when it gets close, and the atoms are picked up by the tip while scanning. Lack of an established point contact ($G_0$ equivalent) hints at a stiff ITO electrode that gets probed by an easily deformed gold tip in different surface binding sites. This view is supported by comparing scanning images before and after crashing the tip, where the images before are of much higher quality, indicating a sharp tip.

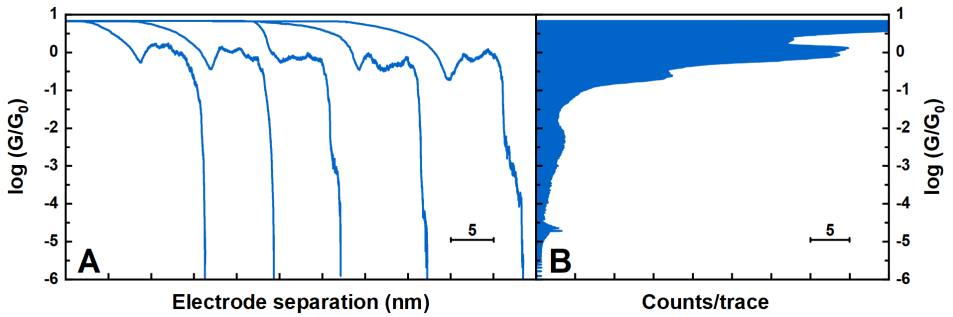


**Figure 5.4** An STMBJ experiment using an ITO substrate and Au tip showing example conductance-distance traces (A) and the corresponding one-dimensional histogram (B).

### 5.3.2 Current-time spectroscopy

The STM-I(t) technique relies on stochastic binding where molecules move in and out of contact with the electrodes due to thermal and Brownian motions. Therefore, this technique works best on molecular monolayers rather than using *in situ* measurements because more molecules are present, which increases the frequency of binding events. It is desirable to obtain uniform molecular layers, which is straightforward to do using thiols [143]. In contrast, the DMBT group might not form monolayers that are well defined, which is why we focused on the thiol-terminated molecules. Two different approaches to the experiment were used to improve the reliability of the Au-molecule-ITO junctions with controlled orientation:

i. SAMs of the molecules on the ITO substrate;

ii. SAMs of the molecules on the Au tip.

The choice of ITO samples matters when forming monolayers [109]. The first few experiments were carried out using PG&O slides, which were kindly donated by the group of Frank Jaeckel (see section 3.3 on Experimental setup). However, for the transport measurements, new ITO slides were purchased from SPI Supplies, based on several independent recommendations regarding monolayer

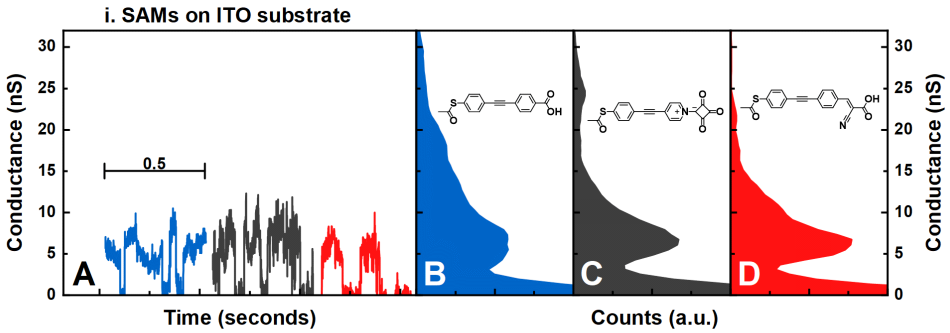


**Figure 5.5** Conductance data for ITO-molecule-Au junctions using SAMs on ITO substrates. (A) Example current-time traces for the wires **A1** (blue), **A2** (grey), and **A3** (red). (B-D) Corresponding one-dimensional conductance histograms with insets show the molecular structures for each histogram. Measurements were carried out using a negative sample bias of 100 mV.

formation. These slides were also used for the 'reverse-I(t)' (current-time-ii) experiments, where the monolayer is formed onto the Au tip.

### SAMs on ITO substrate

Figure 5.5 shows current-time-i data for wires **A**, with stochastic current jumps presented in panel (A), and the histograms that were built from these traces in panels (B-D), also see section 3.3 for details.

### SAMs on Au tip

Figure 5.6 shows current-time-ii data for wires **A**, with the histogram of **A1** in the top left (dark blue), **A2** in the top right (red), and **A3** in the bottom (light blue). Again see section 3.3 for details. Table 5.1 provides a summary for the conductance of Au-molecule-ITO junctions. The two experiments have taken measurements at opposite bias polarities and by forming SAMs on one electrode or the other. A small rectification feature is observed, which might be interpreted according to junction models that are similar to the ones presented here. However, the number of traces that make up the current-time histograms is quite small. Therefore, experiments need to be repeated and even better is

to collect current-voltage characteristics for these systems. The two missing experiments should also be carried out, i.e. a positive sample bias for method i and a negative sample bias for method ii.

**Table 5.1** Summary of junction conductance values for the thiol-wires **A**. All values reported in nS. [i]Molecular SAMs adsorbed onto the ITO substrate. [ii]Molecular SAMs adsorbed onto the Au tip. Positive (+) or negative (−) sample bias indicated for the ITO junctions.

| | **A1** (carboxylic) | **A2** (squarate) | **A3** (cyano) |
|---|---|---|---|
| Au-molecule-Au | 12 | - | 9.0 |
| Au-molecule-ITO[i] (−) | 6.1 | 6.7 | 6.4 |
| Au-molecule-ITO[ii] (+) | 2.5 | 3.6 | 2.6 |
| Rectification Ratio (RR) | ∼2.5 | ∼1.9 | ∼2.7 |

### Rectification

In simple asymmetric molecular wires, like the ones presented in this chapter, molecular orbitals are mostly centred on certain parts of the molecule. In this case, the HOMO is centred on the side of the molecule that contains the

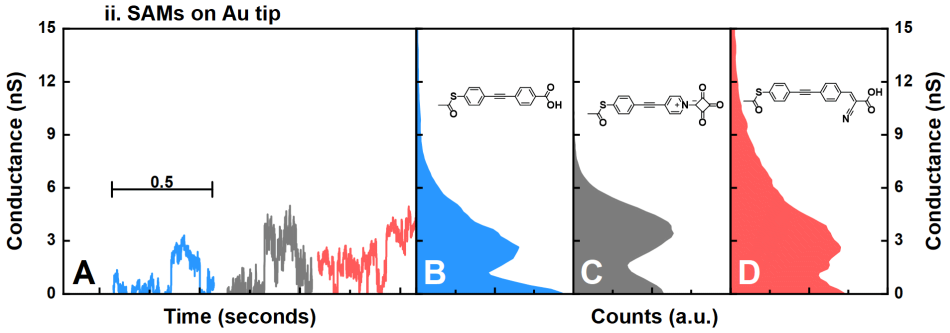


**Figure 5.6** Conductance data for ITO-molecule-Au junctions using SAMs on Au tips. (A) Example current-time traces for the wires **A1** (blue), **A2** (grey), and **A3** (red). (B-D) Corresponding one-dimensional conductance histograms with insets show the molecular structures for each histogram. Measurements were carried out using a positive sample bias of 300 mV.

sulfur anchoring group, and LUMO has more contribution from the other side (unless there is a moiety present that is more electron-rich than the sulfur-side of the tolane wire). We now have a system with asymmetric electrodes and asymmetric positioning of the HOMO and LUMO levels of the molecule within the junction. Here, rectification might then be expected to occur as a result of the relative position of the HOMO level with respect to the Fermi level of the electrodes [144]. It is tempting to extend this picture to our system, even though these hypotheses need to be verified experimentally. In forward bias, the HOMO would lie in between the two electrodes, whereas in reverse bias, it would be located below both Fermi levels. A note of caution needs to be added with respect to the magnitude of the rectification observed in these experiments. This notion is especially true when considering the relatively low number of traces recorded during these experiments.

## 5.4 Surface characterisation

Monolayers of wires **A** on both Au and ITO were analysed using AFM imaging, QCM, XPS, and contact angle measurements.

### 5.4.1 AFM scratching

Figure 5.7 shows AFM images with (top) and without (bottom) a molecular monolayer present. The left panel for each condition shows a scan of the ITO substrate prior to the experiment. The small inset in the centre shows a zoomed-in area where a large force was applied. The right panel shows the same scan area as the left panel (zoomed back out after the experiment). The substrate that had a monolayer (top) clearly shows that it has been deformed by the pressure, whereas the bare substrate (bottom) shows no signs of deformation at all.

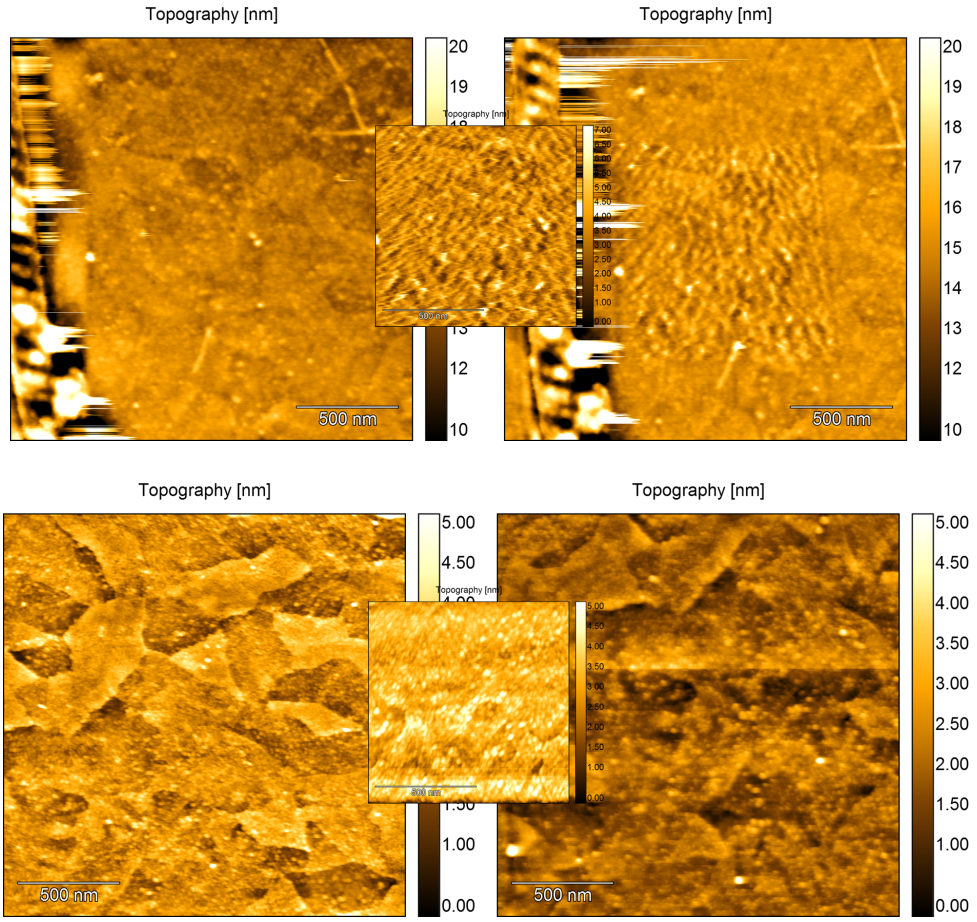


**Figure 5.7** Monolayer scratching experiment using AFM contact-mode imaging. Top: the ITO surface shows a scratched patch in the monolayer after the experiment (right) when compared to its state before scratching (left). Bottom: the bare ITO surface shows no change after the scratching experiment. *Note that these experiments were carried out using PG&O substrates.*

### 5.4.2 QCM, XPS, and contact angle

Figure 5.8 shows two additional molecules, **D** and **E**. These molecules were used in control experiments to determine interactions between anchoring groups and electrodes.

Surface characterisation experiments were carried out by collaborators in Zaragoza, Spain (see chapter 3 for details). X-ray photoelectron spectroscopy (XPS) results for wires **A** are presented in appendix Appendix B and show non-thiol interaction with the ITO substrate in all cases (bottom right plots).


**Figure 5.8** Molecular structures for the control wires used in the surface characterisation experiments.

This observation can be seen from the peaks that correspond to the thiol groups. These peaks are in good agreement with the spectra that are recorded for the powders (graphs on the left in all cases). These two results combined show that the molecule binds to ITO preferentially with its non-thiol anchoring group. Indeed, when molecules **A1** and **A3** are adsorbed onto gold substrates instead (top right panel in Figure B.3 and Figure B.5, respectively), a new peak appears that corresponds to the free thiol anchoring group. This result indicates that the molecules bind to gold with both anchoring groups, which is in good agreement with the gold-gold break-junction data described above. In the case of molecule **A2**, the peak that corresponds to the free thiol is almost completely absent, which indicates preferential thiol-binding of this molecule to gold. This result is also in good agreement with the gold-gold break-junction data described above. In addition, quartz crystal microbalance (QCM) experiments have confirmed that the squarate anchoring group does not interact with gold. Contact angle measurements were also carried out on monolayers of these molecules on gold and on ITO, see Table 5.2. The angles are smaller for monolayers on gold, indicating the relatively hydrophilic non-thiol anchoring groups are free, which is in good agreement with the XPS results. The angles for the monolayers on ITO are larger, which indicates the more hydrophobic thiol groups are unbound. This result also agrees well with the XPS and the conductance experiments. Another interpretation of these results is that the current-time experiments with molecules adsorbed onto ITO might be more reliable since the binding of the molecules has a greater preferential orientation. This conclusion is especially true for the squarate wire **A2** since it does not interact with gold at all.

**Table 5.2** Contact angles of molecular SAMs on Au and ITO.

| | **A1** (carboxylic) | **A2** (squarate) | **A3** (cyano) |
|---|---|---|---|
| Contact angle on Au | 73° | 63° | 72° |
| Contact angle on ITO | 79° | 80° | 77° |

## 5.5 Calculations

Due to the challenges involved with modelling the ITO electrodes, computational studies are currently still ongoing. Preliminary data shows that there are many possible transmission paths in the Au-molecule-ITO junction. The results are difficult to interpret, even when the theoretical model is limited to a specific metal oxide surface configuration. Therefore, more detailed surface characterisation experiments are currently ongoing in an attempt to reduce the total number of possible binding configurations. Finding a specific binding mode for each molecule is likely to reduce drastically the number of transmission pathways and thus will be a great enhancement for the theoretical model. Figure 5.9 shows UV-VIS absorption spectra for wires **A** in the same solvents that the Au-molecule-Au junctions were measured in. These experiments give an indication for the band gap, which also makes the transport calculations more accurate.

## 5.6 Conclusions

We have measured electrical transport properties of a series of tolane wires using STM techniques to form metal-molecule-metal junctions. We first determined rough conductance values of eight wires using two gold electrodes in the break-junction. Values were around $10^{-3.5}$ $G_0$ for all wires that formed junctions, which is slightly lower than values for symmetric tolane wires as expected [77]. Crucially, the pyridinium squarate group does not form any junctions using gold electrodes only. Next, we focused on the thiol molecules for forming asymmetric

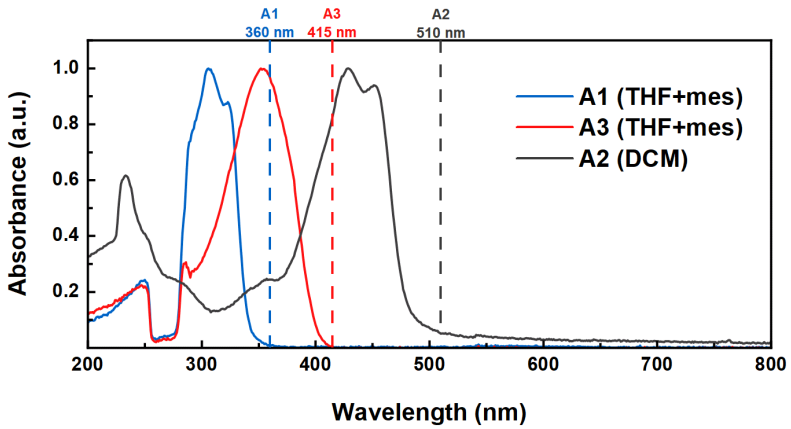


**Figure 5.9** Absorption profiles for wires **A1-3** in the same solvent as the conductance measurements. The shoulder of the peak gives an estimation for the HOMO-LUMO band gap, shown by the dashed lines for each wire. The converted values are 3.44 eV for **A1**, 2.99 eV for **A3**, and 2.43 eV for **A2**.

Au-molecule-ITO junctions. Here we have shown the controlled orientation of the molecules by design of their electrode-specific anchoring groups, which is confirmed by surface characterisation experiments. These asymmetric junctions show rectifying behaviour, which can be attributed to both the nature of the molecule and the two different electrode materials at either end of the junction. The rectification ratio is ∼2.6 for wires **A1** and **A3**, but has a slightly lower value of ∼1.9 for the squarate wire **A2**. However, these results come from small datasets and thus more traces should be added to improve the statistics of these values. We have also shown that current-distance experiments using ITO electrodes are very challenging as the tunnelling current only drops to the noise floor when the electrode separation reaches >20 nm, regardless of whether molecules are present in the environment of the electrodes.

Future work includes light-modulation experiments and evaporation techniques to make ITO tips for symmetric transport experiments. Large-area conductance measurements on molecular layers using ITO as the bottom electrode is also an important next step.

# Chapter 6

# Complex architectures

*"In math, you're either right or you're wrong."*

— **Katherine Johnson**

## 6.1 Introduction

There has been a tremendous interest in studying the electrical properties of complex molecular architectures in recent years. In particular, long-range electron transport mechanisms are important for the design of complex architectures and can be achieved using secondary structures, e.g. conformational folding (peptides [145]) or supramolecular effects like host-guest (shown earlier by our group [146]), or charge-transfer complexation [147].

This chapter will first describe the design of a three-dimensional (3D) molecular conductor, see wires **1Fe** and **1Co** on the left in Figure 6.1. The spatial orientation of this molecule is such that the ligands form a symmetrical helix around the metal centre resulting in a ball-like structure. The aim here is to study lateral interactions between ligand (or molecules) and nonlinear conformations at the same time. As mentioned in chapter 1, it is an important objective to optimise anchoring groups for single-molecule active components in electronic nanodevices. In the second part of this chapter, a molecular wire that incorporates metal atoms in one of its anchoring groups is discussed, see **FePt** in the middle of Figure 6.1. The third and final section of this chapter covers a molecular wire that is designed for active optical switching, see **DHP** on the right in Figure 6.1. Such a system is particularly interesting in conjunction with transparent electrodes from chapter 5.

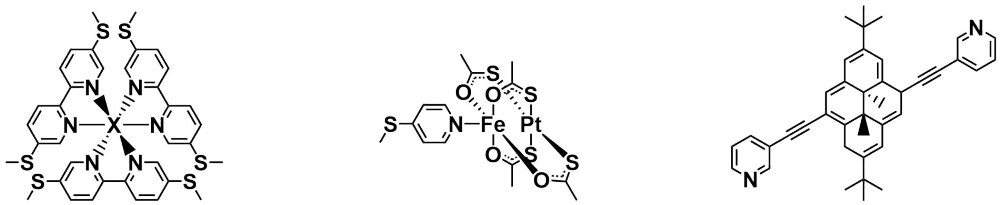


**Figure 6.1** Molecular structures for the three systems covered in this chapter: a molecular ball (left), a metallic anchor (middle), and an optical switch (right).

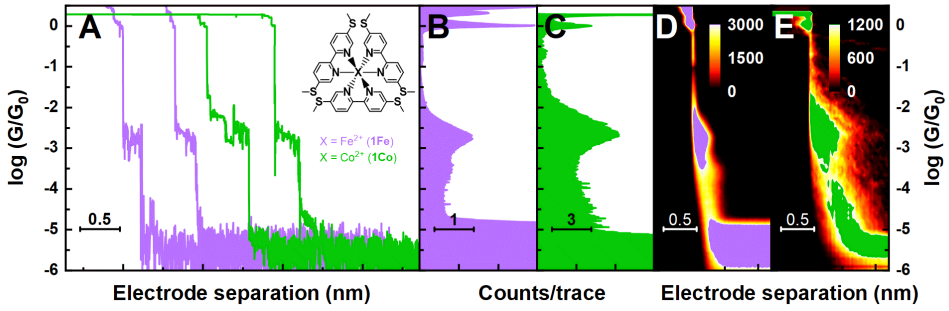


**Figure 6.2** Single-molecule conductance data for **1Fe** (purple) and **1Co** (green). Example conductance-distance traces along with molecular structures (A), as well as one-dimensional (B, C) and two-dimensional histograms (D, E).

## 6.2 A molecular ball

Figure 6.2 shows single-molecule conductance data for metal complexes **1Fe** and **1Co**, with example conductance-distance traces for both wires in panel A. The two purple traces on the left correspond to the iron complex and the two green ones on the right to the cobalt complex. Clear molecular plateaus can be seen just below $10^{-3}$ $G/G_0$, resulting in distinct peaks in the one-dimensional (1D) histograms of **1Fe** and **1Co** in panels B and C, respectively. The same features are also visible in the two-dimensional (2D) histograms in panel D (**1Fe**) and E (**1Co**). However, the junction formation probability (JFP), defined as the number of traces with a molecular feature divided by the total number of traces, is lower for both these molecules when compared to simple linear wires bearing the same anchoring groups. This is indicated by an intensity count of clean tunnelling traces (no molecular junctions) reaching ∼1500 and ∼600 in panels D and E, respectively. For comparison, see 2D histograms of **2a** and **3a** in Figure 4.2F and H on page 50. This means that over half of the conductance-distance traces do not show any molecular features in each case, which is likely a result of the spherical geometry of the molecules, making it harder for the molecules to bridge the gap between the electrodes. The magnitude of the conductance is around the expected value for the ligand (bearing in mind that

**2a** is longer than the ligands of these wires), which means that it if the metal ion participates in the charge transport pathway, it does not significantly affect the conductance. However, it is more likely that the metal ion does not actually participate in charge transport, as has been found for other systems where the metal is part of an optional electron pathway (see chapter 4 of reference [148]). In order to verify this, longer helix wires with a deliberate break in the ligand conjugation pathway were also synthesised and measured. Unfortunately, their poor solubility requires measurements in polar solvents, which means that *in situ* break-junction experiments are not suitable for these longer wires with a much lower conductance. Therefore, they were preadsorbed onto the gold substrate and subsequently measured in air. The molecular structures of these compounds, along with their conductance histograms, are presented in appendix Appendix C, Figure C.1 on page 114. There is a faint feature visible in the 2D histogram of **2Fe** as indicated by the white circle, but the JFP is extremely low, and **2Co** does not show any molecular features. Theoretical calculations on the short wires **1Fe** and **1Co** are currently ongoing as another approach to verify whether the metals contribute to the conductance pathway.

## 6.3 A metallic anchor

A short molecule with a new metallic anchoring group is presented in this section, where one of the metals is proposed to participate in binding to the electrode. Example conductance-distance traces are shown in panel A of Figure 6.3, showing several different types of characteristic molecular plateaus. From left to right, the first two traces in pink show a small feature at a relatively high conductance of $\sim 10^{-1.5}$ $G/G_0$, which may come from the electrodes binding to the thioether on one end and the pyridine nitrogen in the middle. The next two traces (in purple) show features approximately one order of magnitude lower, with a slightly longer plateau, where the second one in light purple shows added telegraphic noise. These features would then

be a result of the electrodes binding to the terminal ends of the molecule. The final three traces in cyan show traces with a combination of both these features, indicating that the junction might start with one electrode binding to the nitrogen, followed by the molecule terminally bridging the gap upon further electrode separation. With these features clearly present in individual conductance-distance traces, a distinct peak in the conductance histograms would be expected. However, no molecular features can be seen when all traces are combined into histograms, see panels B and C of Figure 6.3. This is likely due to a combination of conductance features at various values, and a low JFP (see discussion above), which has been shown to result in poor histograms [149]. Manually selecting only the traces that contain a plateau shows a JFP of approximately 10%. However, since the selection of data by hand introduces a subjective inclination, the above experiment was repeated for a range of different concentrations and bias voltages, with the aim to observe conductance peaks in unselected data. Increasing the bias voltage to 200 mV did not increase the JFP noticeably, but a faint molecular feature did appear at a bias of 300 mV with a concentration of 0.1 mM and above. This could mean that JFP depends on electric field strength, which is in contrast with the idea that junctions are mechanically less stable at higher bias and therefore have a shorter lifetime. Another thing to note is that the $G_0$ peak in both histograms is poorly defined, which results from having many noisy traces like the dark purple one shown in panel A. This can be caused when the molecules start covering the electrode surface after prolonged experiment times, making clean gold-gold point contacts less probable. The experiments were also carried out using three equivalents of **FePt**, with the iron atom being replaced by a cobalt, nickel, and zinc atom, respectively. The idea here is that small differences in electronic structure might improve the JFP, but unfortunately, none of these wires showed any molecular feature in unselected histograms either. It seems that the break-junction technique is not suitable for measuring these molecules, which could be a result of the undercoordinated nature of available gold sites,

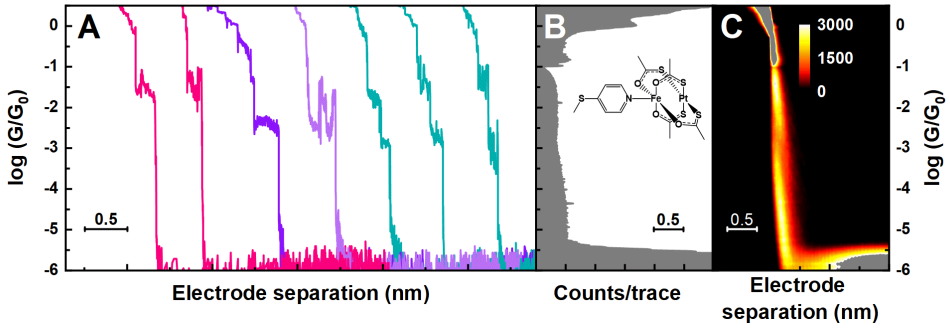


**Figure 6.3** Single-molecule conductance data for **FePt** with example conductance-distance traces (A) showing several distinct types of plateaus. 1D histogram (B) with the molecular structure of **FePt**, and 2D histogram (C).

to which the planar anchoring group of these molecules do not readily bind.

## 6.4 An optical switch

Molecular wires with the pyrene moiety can structurally switch between two isomers [150]. The closed ring form (as presented in the right panel of Figure 6.1) opens up when irradiated with visible light. This ring opening is reversible and the original structure can be recovered either by exposure to UV light, or by heating up the sample. We have added extra alkyne groups in comparison to reference [150] to increase the junction formation probability. In addition, the specific wire presented here has meta-substituted pyridine anchoring groups, see Figure 6.4. Example conductance-distance traces are shown in panel A. The first two traces in magenta are examples from the dataset recorded at a bias voltage of 100 mV. The resulting histogram in Figure 6.4B is poorly defined due to its proximity to the noise floor. A common tool for improving the signal-to-noise ratio and thereby obtaining a well-defined histogram peak is to increase the bias voltage of the experiment. This pushes down the absolute value of the conductance noise floor because it stems from a lower limit of the current, and not the conductance. The experiment was thus repeated at a bias voltage of

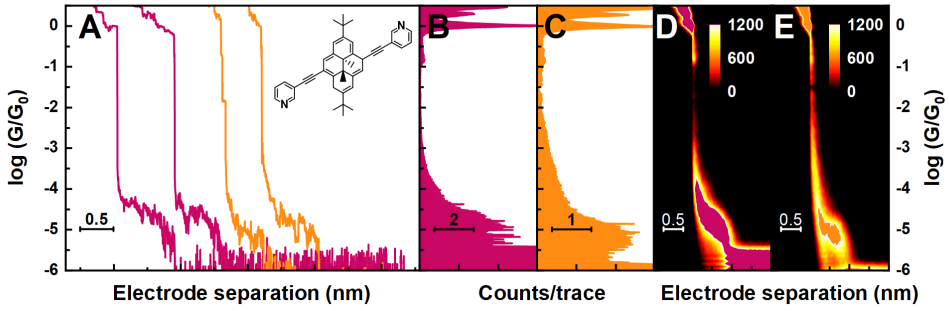


**Figure 6.4** Single-molecule conductance data for **DHP** measured at a bias voltage of 100 mV (magenta) and 300 mV (orange). Example conductance-distance traces along with the molecular structure (A), as well as one-dimensional (B, C) and two-dimensional histograms (D, E).

300 mV, example traces of which are shown in orange in panel A, along with its histograms is panel C and E. Remarkably, the conductance value seems to drop slightly when the bias voltage is increased, which could be caused by a nonlinear feature in the current-voltage characteristics. Therefore, the first effect that comes to mind is negative differential resistance (NDR). This effect typically arises from molecular orbital energies aligning with the electrodes [151]. As the bias voltage is increased, the molecular energy levels first are in resonance with the electrodes. Upon further increasing the bias voltage, the energy levels shift off resonance, which leads to a decrease in the current. Unfortunately, there are issues when applying this exciting hypothesis to the **DHP** system discussed here. Most importantly, the effect does not seem to be present when current-voltage experiments are carried out on the molecular junction. However, the effect was also seen for single-molecule conductance data of the para-substituted equivalent of this meta-substituted pyridine wire. Therefore, a more likely reason for the observed results is that only a portion of the 100 mV histogram (magenta, panel B) is sampled at 300 mV (orange histogram, panel C). This would explain why the observed number of counts per trace is approximately halved for the measurement at relatively high bias, indicating less stable molecular junctions. That said, even a bias voltage of 300

mV is relatively mild and still quite far from any other tunnelling mechanisms coming into play.

## 6.5 Conclusions

We measured the conductance of three types of molecular wires bearing functionality beyond the traditional linear structure, collectively referred to in this chapter as complex architectures. The first design consists of a 3D helical structure, in which the metal centres do not seem to participate in the dominant transport pathway. The metallic functionality of the lantern complex in the second design prove difficult to evaluate using STMBJ, despite molecular features present in individual traces. As a result, the question remains unanswered whether the lantern metal atoms play a direct role in the hybridisation of the metal-molecule anchor. A promising alternative technique to try as a next step is STM current-time spectroscopy, as discussed in subsection 5.3.2 on page 75. This technique is recommended because it does not form direct contacts between the metal electrodes and relies on stochastic binding events, thus allowing for junctions to form that are less robust and happen on longer timescales. The third and final design, which contains the optically switchable pyrene moiety, showed a curious conductance dependence on the applied bias voltage. It is likely that this result is caused by a change in junction stability when the bias voltage, and thus the electric field strength, is increased.

Overall, control experiments are recommended for the helix and the lantern wires, by using their bare ligands, to confirm the exact behaviour of the wires. After establishing the reason for the conductance-bias behaviour of the pyrene wires, their optical switching properties need to be tested with light in solution first, and then in the metal-molecule-metal junction too.

# Chapter 7

# Conclusions

*"Have no fear of perfection; you'll never reach it."*

— **Marie Skłodowska Curie**

The central focus of this thesis has been to manipulate specific parts of nanoscale electronic junctions and to study how these changes affect electron transport through these junctions. Scanning tunnelling microscopy techniques have been used to fabricate single-molecule junctions consisting of metal-molecule-metal and metal-molecule-semiconductor architectures.

First, in chapter 4, the backbones of a series of conjugated molecular wires were modified by adding a platinum or ruthenium metal atom in the centre while keeping the thioether-based anchoring groups the same. As discussed, the resulting organometallic molecular wires generally have a conductance of up to an order magnitude higher than their organic counterparts. However, the platinum wires presented here are less conductive than the organic wires, which is in contrast to results of similar systems found in the literature. For the organic and ruthenium wires, a correlation was found between conductance values and oxidation potentials, the latter providing an estimated position of the highest occupied molecular orbital. The platinum wires did not follow this trend, hinting at an increased contribution of $\sigma$-orbitals in these wires. This finding also explains the relatively low values of conductance for these wires.

Next, in chapter 5, the molecular bridge was kept constant while the impact of electrode design on electron transport was evaluated using a series of asymmetric molecular wires. Here, one end of the molecule had an anchoring group that is known to bind well to gold electrodes, while the other was designed explicitly for binding to indium tin oxide. A set of anchoring group combinations was first tested using gold-gold break-junctions, after which three specific wires were selected for further studies on indium tin oxide substrates. One of the new anchoring groups did not bind to gold, only to indium tin oxide, which is an advantage for studying asymmetric metal-molecule-semiconductor junctions like these as the orientation of molecules in the junction can be controlled. Switching the polarity of the applied bias voltage across these asymmetric junctions resulted in moderate rectification. This result is not surprising as differences in the electrodes and anchoring groups on either side

of the junction result in an asymmetric distribution of electron density. This asymmetry makes it easier for the electrons to flow in one direction compared to the other.

Finally, in chapter 6, three examples of more complex and new molecular wires were presented. The first design aimed to study supramolecular interactions within a single helical wire that contains a metal centre. The conductivities of these wires are in the same range as the values for the bare ligands, which indicates that the metal centres do not seem to participate in the dominant transport pathway. The second design aimed to increase the coupling between molecules and electrodes by using an organometallic moiety in one anchoring group of the molecules. Despite molecular features present in individual traces, the dynamic break-junction technique does not seem suitable for measuring these lantern complexes. The third and last design aimed to create an active molecular junction that can be switched between states of relatively high and low conductance using light as an external source. Experiments involving this system are currently ongoing, but preliminary results show a curious inverse correlation of conductance with applied bias voltage.

This work has confirmed the complex interplay between parameters at the nanoscale together determining electron transport through molecular junctions. The path to applications is still posed with many challenges, yet this work provides a small contribution to its progress, and hopefully, there will be more exciting discoveries along the road to molecular electronic applications.

# Chapter 8

# Future directions

*"We should be excited about the future & striving to go beyond the horizon!"*

— **Elon Musk**

Molecular electronics is a highly multidisciplinary field, which has brought together researchers from backgrounds in chemistry, physics, engineering, and biology alike. Many breakthroughs have advanced the field tremendously over the last few decades, and it has become one of the fastest-growing areas of research. However, there is still a long way to go until applications based on molecular assemblies can be realised. For example, reproducible and robust device fabrication is needed for scaling up production to reach the market. Some of the issues that are faced by currently existing methods include yield, variation, stability, integration, and reproducibility [3]. Therefore, new techniques need to be developed for reliably creating molecular electronic devices at a larger scale with a high yield.

Another specific technological challenge is to lower the power consumption of commercial devices. Molecular systems are well-suited to achieve this efficiency goal because of their ability to operate at low bias voltages. However, the critical obstacle here is that inefficient coupling between the molecules and the electrodes leads to high contact resistances [12]. The molecule-electrode interface has been a central area of focus ever since techniques in the field made the research accessible in laboratories. This interface will likely continue to receive considerable attention for several reasons. Firstly, the formation of electrodes, metal and nonmetal alike, is essential both for studying junction properties and for scaling up device fabrication as mentioned above. Secondly, the coupling strength is one of the most significant factors that dictates charge transport. For this reason, researching anchoring groups will continue to be significant, especially new groups for nonmetal electrodes. Thirdly, due to the significant contact resistance at the interface, new ways of reducing this resistance will be necessary. Covalent carbon bonds are one example of a good solution to this last problem [21]. Finally, resonant tunnelling devices based on molecular assemblies will need the band gap features of semiconductor architectures because energy level broadening in metal-molecule-metal junctions are not suitable for these devices [152].

Looking at inorganic chemistry, incorporating metal centres into molecular wires generally enhances the conductance through reduced optical band gaps [114]. However, since the molecule-electrode coupling is more important for increasing electron transmission, the advantages of metal complexes are more likely found in two other areas. Firstly, the robust and reversible redox properties will be important for switching functionalities using electrical gating as an external stimulus. Furthermore, the existing versatility and convenience of molecular synthesis are expanded even further through inorganic design. The benefits that result from this vast chemical design space are numerous. For example, to engineer molecular monolayers and even multi-layers for studies on molecular communication. In particular, it is still unclear when molecular assemblies have a strong coupling and consequently enhance the overall tunnelling current [153].

A more general problem in the field is the limited information available from simple conductance measurements. Therefore, the ability to provide detailed information about the nanoscopic environment during the measurements will be valuable. To achieve this, the integration of *in situ* characterisation methods is indispensable. An additional benefit of this integration is that these characterisation methods can easily be tuned or adapted to function as external parameters for junction switching [154].

A principal theme throughout the interdisciplinary field of molecular electronics is the presence of a wide variety of research topics. One such example is the cross-over to studies in biological systems, where peptides, proteins, and DNA have been the subject of several investigations [155]. The continued integration of nanoelectronics with fields like biochemistry and biophysics will likely result in an explosive number of new studies over the next few years. Other fields such as inorganic chemistry and optoelectronic physics can expect to receive a similar treatment. Sensors are prone to reach the market sooner than transistors do because sensor devices are more straightforward to manufacture than transistors, but who knows what will be discovered and developed along the way? Either

way, exciting times are ahead for the field and the potential contributions that will follow from continued effort of research groups around the world.

# Appendices

# Appendix A

# Supplementary information for chapter 4

## A.1 Statistical fitting

The following list of figures show the Gaussian fits to the conductance values, and to the break-off distances of the molecular wires in chapter 4. See chapter 3 for details of the analysis procedures.

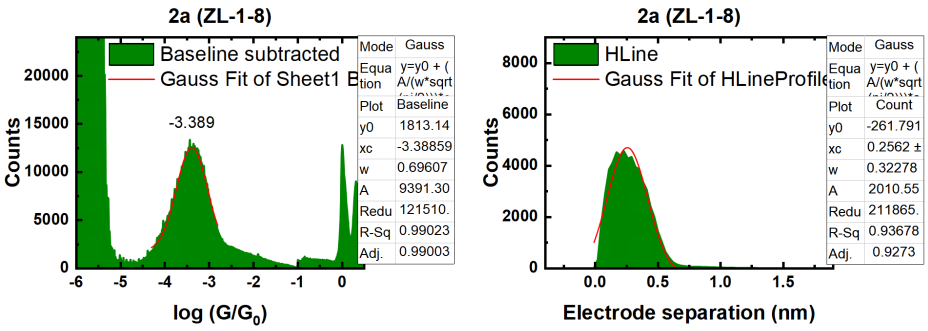


**Figure A.1** Gaussian fits to the histograms of **2a** in chapter 4: 1D conductance plot (left), and 2D break-off plot (right). Histograms compiled from 5306 current-distance traces recorded in a 1 mM mesitylene solution at an applied bias voltage of 100 mV (real bias was 104 mV). Molecular length is 1.571 nm as measured by the sulfur-sulfur distance, determined from crystallography data.

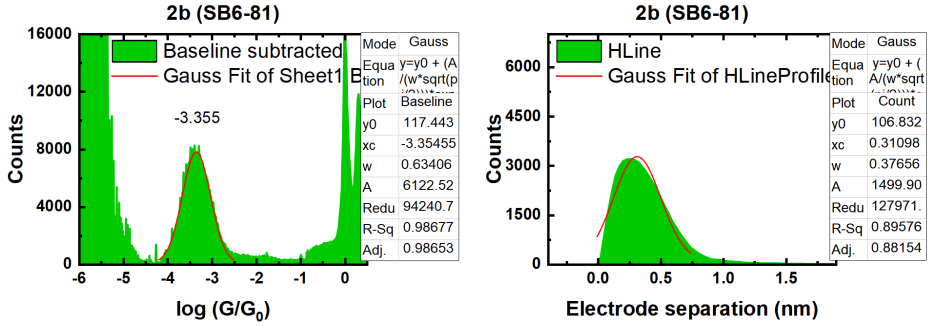


**Figure A.2** Gaussian fits to the histograms of **2b** in chapter 4: 1D conductance plot (left), and 2D break-off plot (right). Histograms compiled from 5395 current-distance traces recorded in a 1 mM mesitylene solution at an applied bias voltage of 100 mV (real bias was 76 mV). Molecular length is 1.566 nm as measured by the sulfur-sulfur distance, determined from crystallography data.

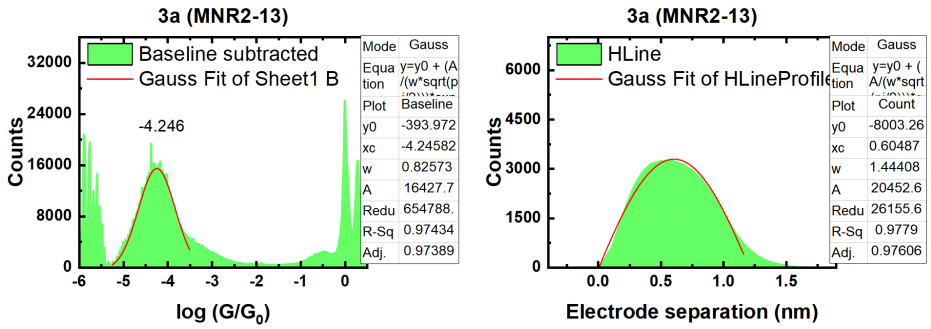


**Figure A.3** Gaussian fits to the histograms of **3a** in chapter 4: 1D conductance plot (left), and 2D break-off plot (right). Histograms compiled from 5451 current-distance traces recorded in a 1 mM mesitylene solution at an applied bias voltage of 100 mV. Molecular length is 2.007 nm as measured by the sulfur-sulfur distance, determined from crystallography data.

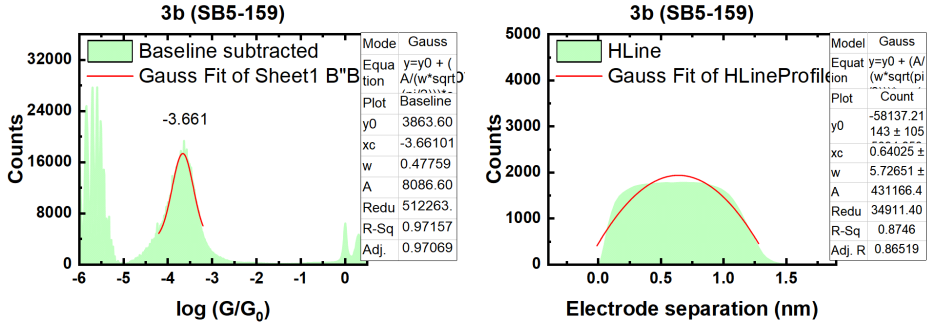


**Figure A.4** Gaussian fits to the histograms of **3b** in chapter 4: 1D conductance plot (left), and 2D break-off plot (right). Histograms compiled from 5451 current-distance traces recorded in a 1 mM mesitylene solution at an applied bias voltage of 100 mV (real bias was 75 mV). Molecular length is 2.000 nm as measured by the sulfur-sulfur distance, estimated from crystallography data.

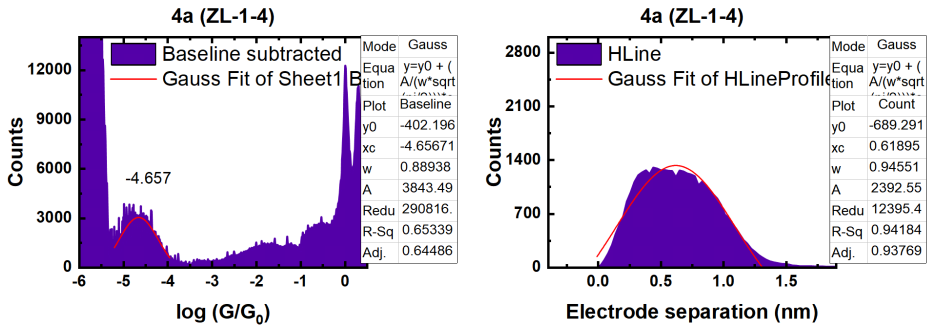


**Figure A.5** Gaussian fits to the histograms of **4a** in chapter 4: 1D conductance plot (left), and 2D break-off plot (right). Histograms compiled from 3366 current-distance traces recorded in a 1 mM mesitylene solution at an applied bias voltage of 100 mV (real bias was 100 mV). Molecular length is 1.847 nm as measured by the sulfur-sulfur distance, determined from crystallography data.

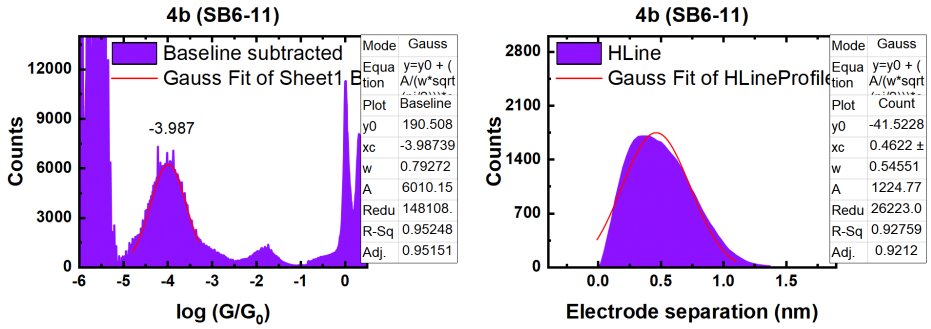


**Figure A.6** Gaussian fits to the histograms of **4b** in chapter 4: 1D conductance plot (left), and 2D break-off plot (right). Histograms compiled from 3641 current-distance traces recorded in a 1 mM mesitylene solution at an applied bias voltage of 100 mV (real bias was 71 mV). Molecular length is 1.839 nm as measured by the sulfur-sulfur distance, determined from crystallography data.

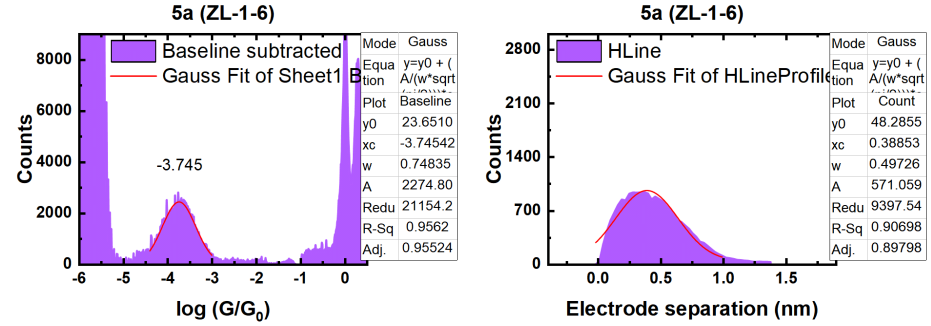


**Figure A.7** Gaussian fits to the histograms of **5a** in chapter 4: 1D conductance plot (left), and 2D break-off plot (right). Histograms compiled from 2873 scans recorded in a 1 mM mesitylene solution at an applied bias voltage of 100 mV.

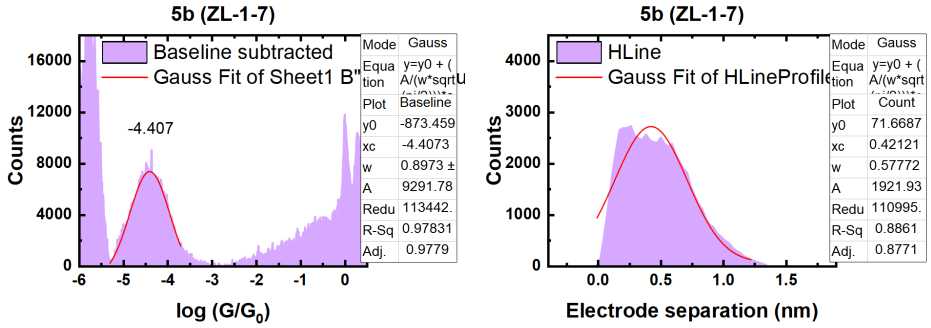


**Figure A.8** Gaussian fits to the histograms of **5b** in chapter 4: 1D conductance plot (left), and 2D break-off plot (right). Histograms compiled from 3832 current-distance traces recorded in a 1 mM mesitylene solution at an applied bias voltage of 100 mV.

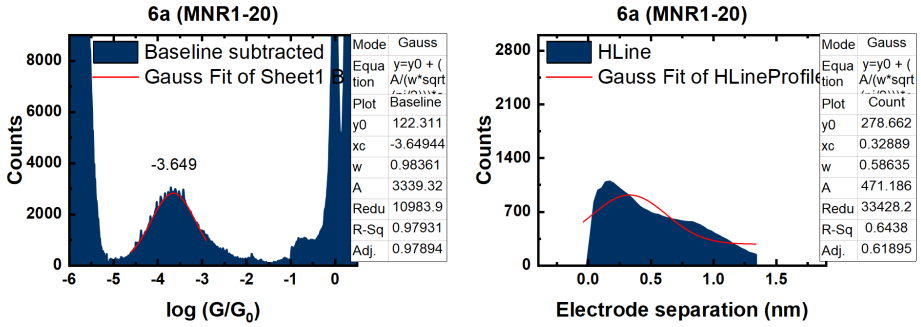


**Figure A.9** Gaussian fits to the histograms of **6a** in chapter 4: 1D conductance plot (left), and 2D break-off plot (right). Histograms compiled from 3814 current-distance traces recorded from three separate experiments in 0.1 mM solutions of 3:7 solvent mixtures of THF:mesitylene at an applied bias voltage of 100 mV. Molecular length is 1.858 nm as measured by the sulfur-sulfur distance, determined from crystallography data.

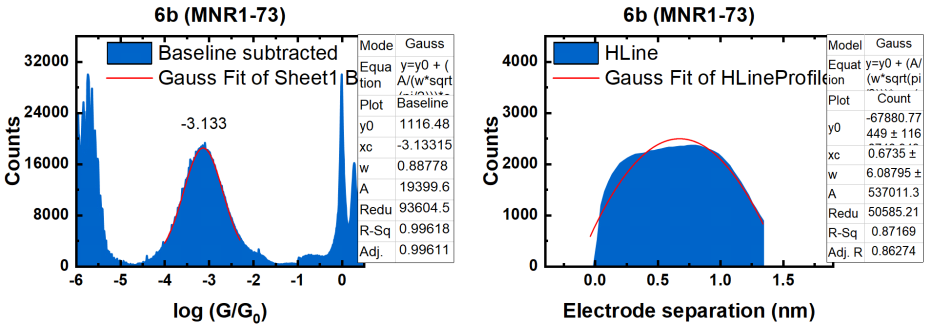


**Figure A.10** Gaussian fits to the histograms of **6b** in chapter 4: 1D conductance plot (left), and 2D break-off plot (right). Histograms compiled from 5015 current-distance traces recorded in a 0.1 mM solution of 1:4 solvent mixture of THF:mesitylene at an applied bias voltage of 100 mV. Molecular length is 1.853 nm as measured by the sulfur-sulfur distance, determined from crystallography data.

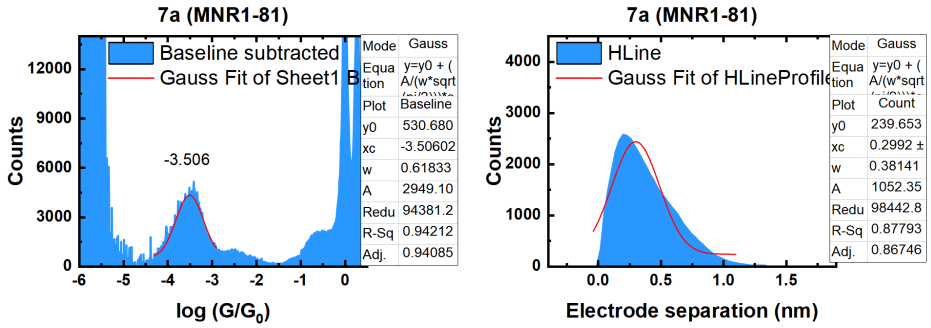


**Figure A.11** Gauss fits to the histograms of **7a** in chapter 4: 1D conductance plot (left), and 2D break-off plot (right). Histograms compiled from 5432 current-distance traces recorded in a 1 mM mesitylene solution at an applied bias voltage of 100 mV. Molecular length is 1.857 nm as measured by the sulfur-sulfur distance, determined from crystallography data.

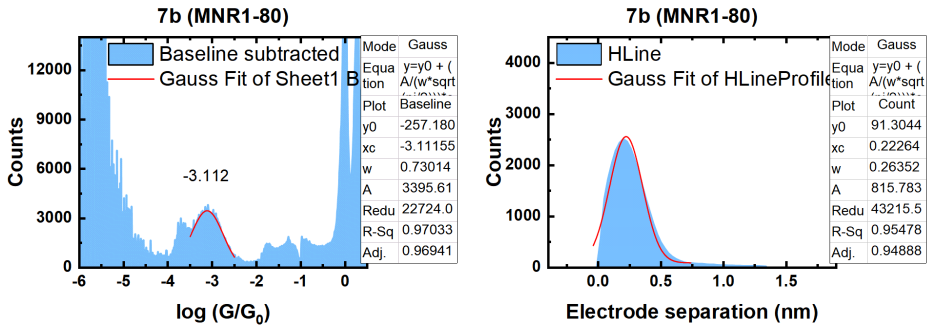


**Figure A.12** Gaussian fits to the histograms of **7b** in chapter 4: 1D conductance plot (left), and 2D break-off plot (right). Histograms compiled from 5493 current-distance traces recorded in a 1 mM mesitylene solution at an applied bias voltage of 100 mV. Molecular length is 1.830 nm as measured by the sulfur-sulfur distance, determined from crystallography data.

## A.2 Scan rate analysis

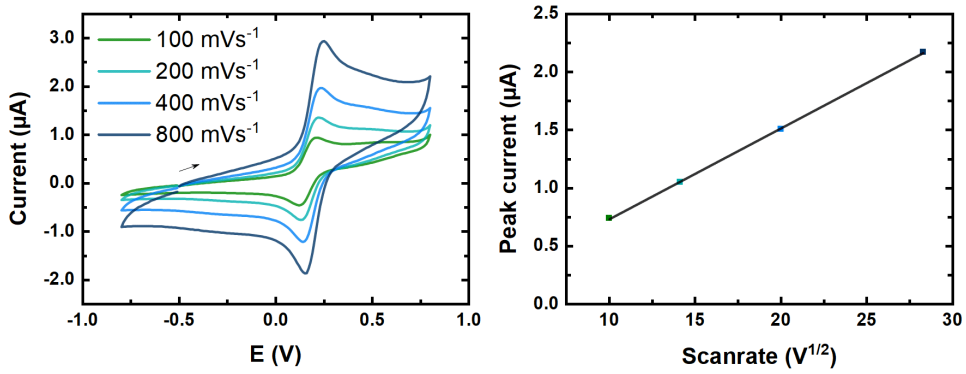


**Figure A.13** Scan rate analysis for **6a** in chapter 4: Overlay of scan rates (left), and the corresponding linear fit (right).

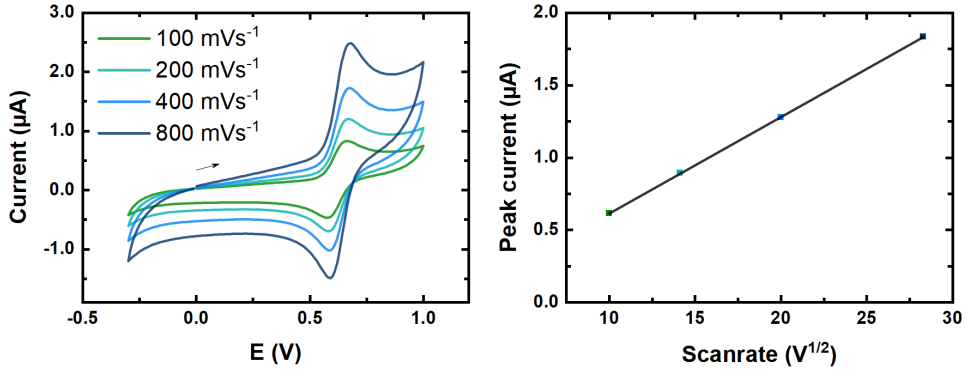


**Figure A.14** Scan rate analysis for **6b** in chapter 4: Overlay of scan rates (left), and the corresponding linear fit (right).

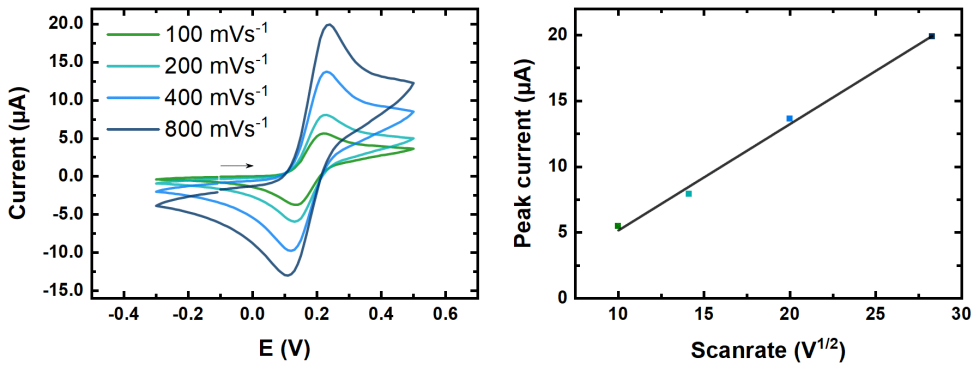


**Figure A.15** Scan rate analysis for **7a** in chapter 4: Overlay of scan rates (left), and the corresponding linear fit (right).

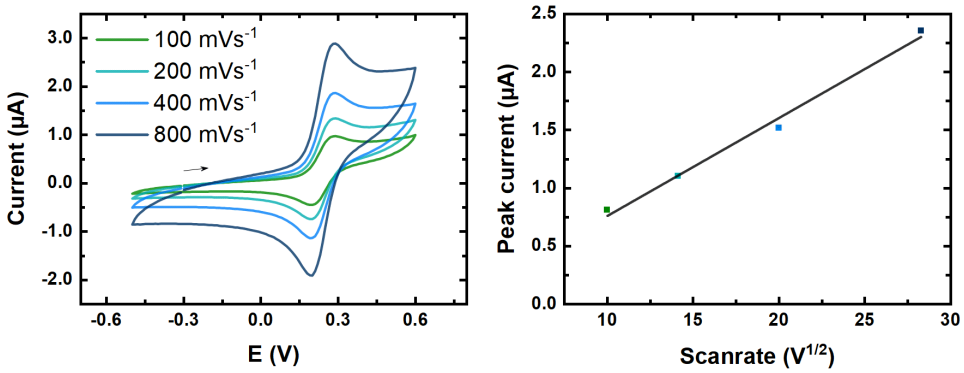


**Figure A.16** Scan rate analysis for **7b** in chapter 4: Overlay of scan rates (left), and the corresponding linear fit (right).

## A.3 Thermoelectric properties

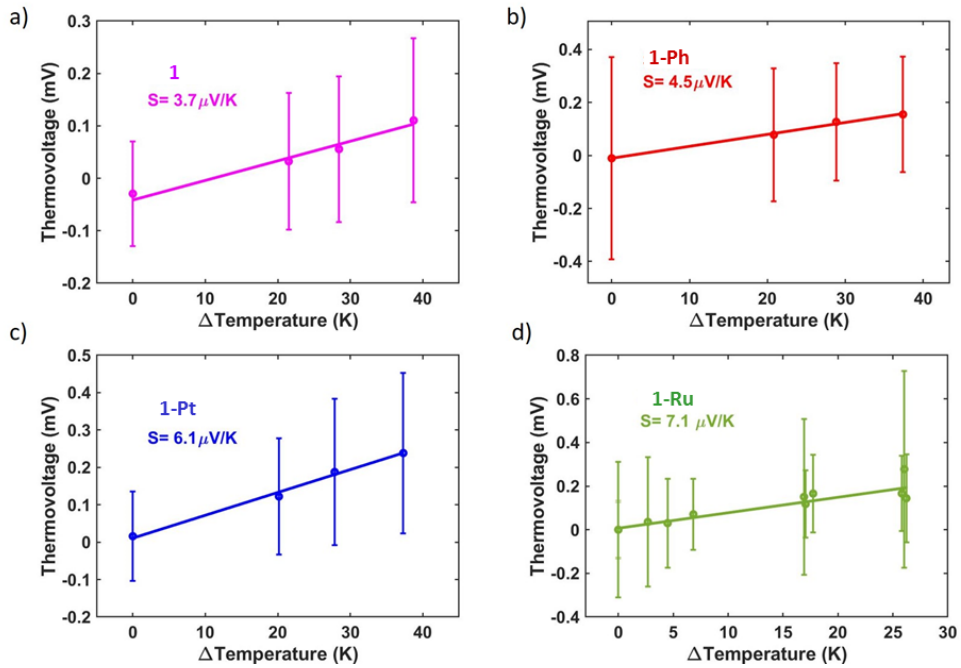


**Figure A.17** Thermopower measurements of selected DMBT-wires: (a) **2b** labelled as **1**, (b) **3b** labelled as **1-Ph**, (c) **4b** labelled as **1-Pt**, and (d) **7b** labelled as **1-Ru**.

# Appendix B

# Supplementary information for chapter 5

## B.1 HOMO-LUMO levels for B4 and C4

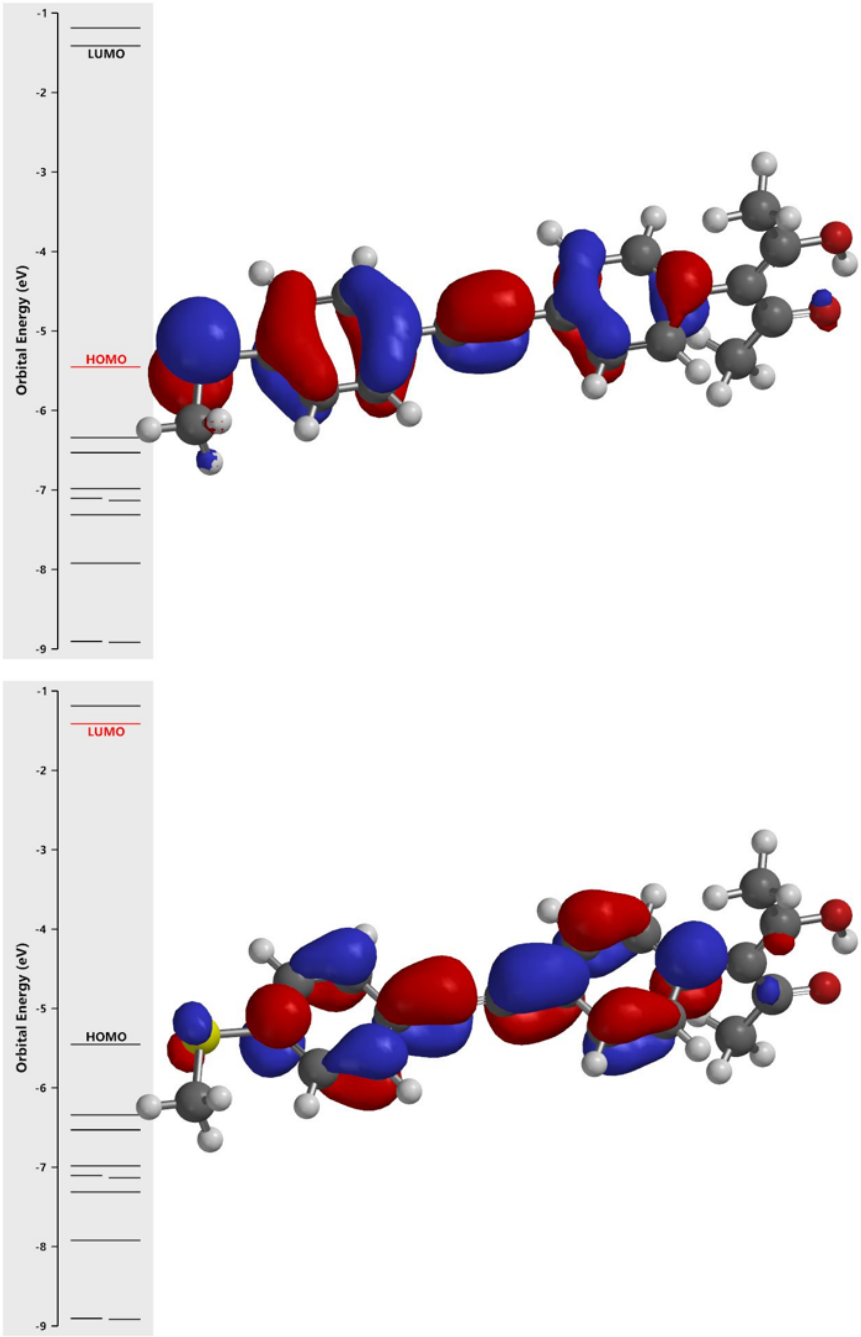


**Figure B.1** HOMO (top), and LUMO (bottom) levels for wire **B4**.

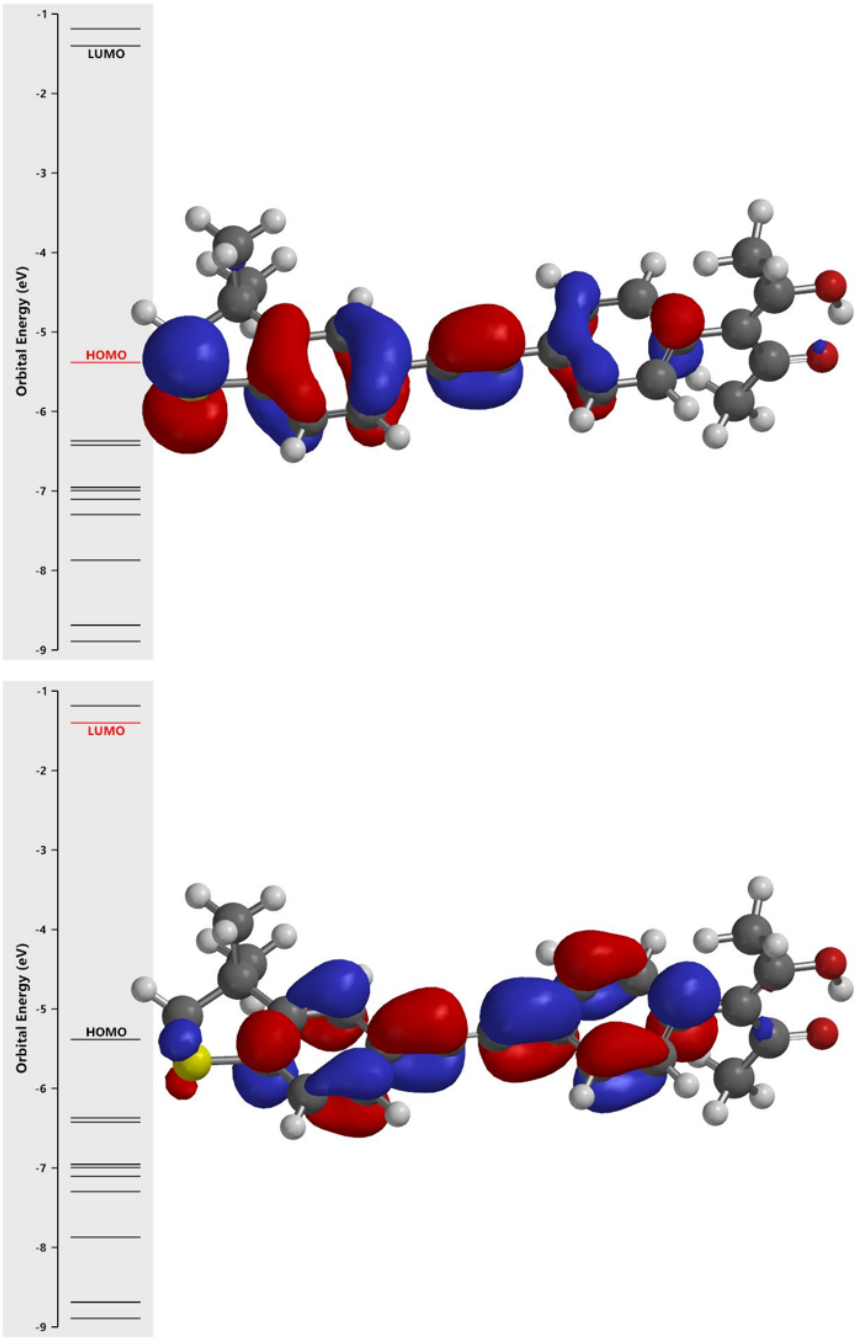


**Figure B.2** HOMO (top), and LUMO (bottom) levels for wire **C4**.

## B.2 XPS data for wires A1-3

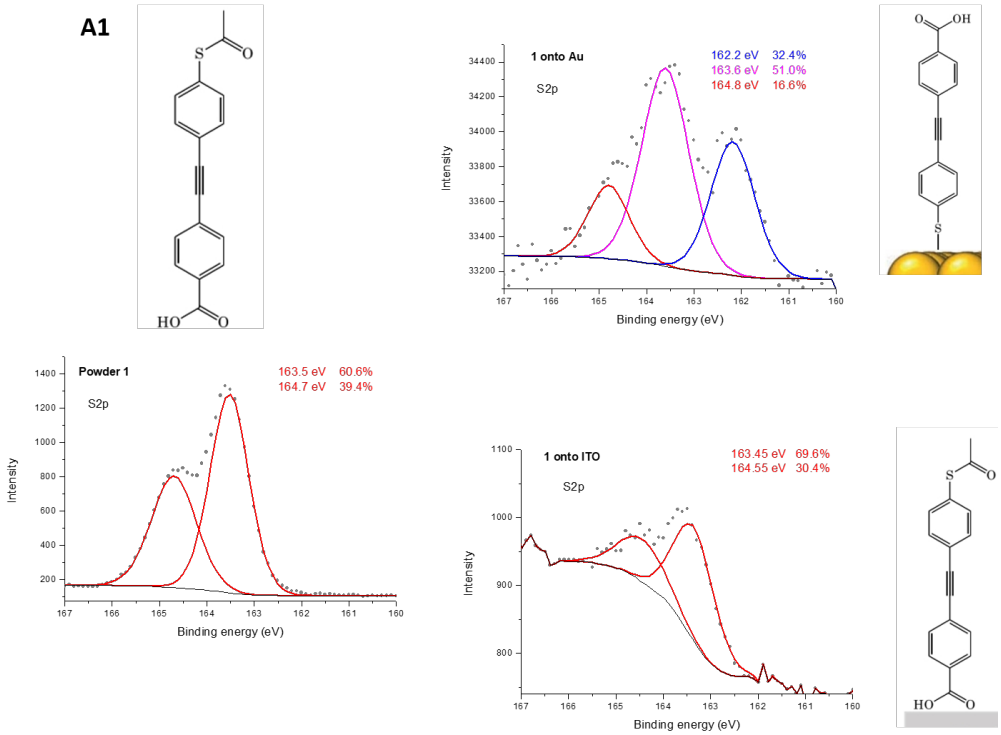


**Figure B.3** XPS results of **A1**.

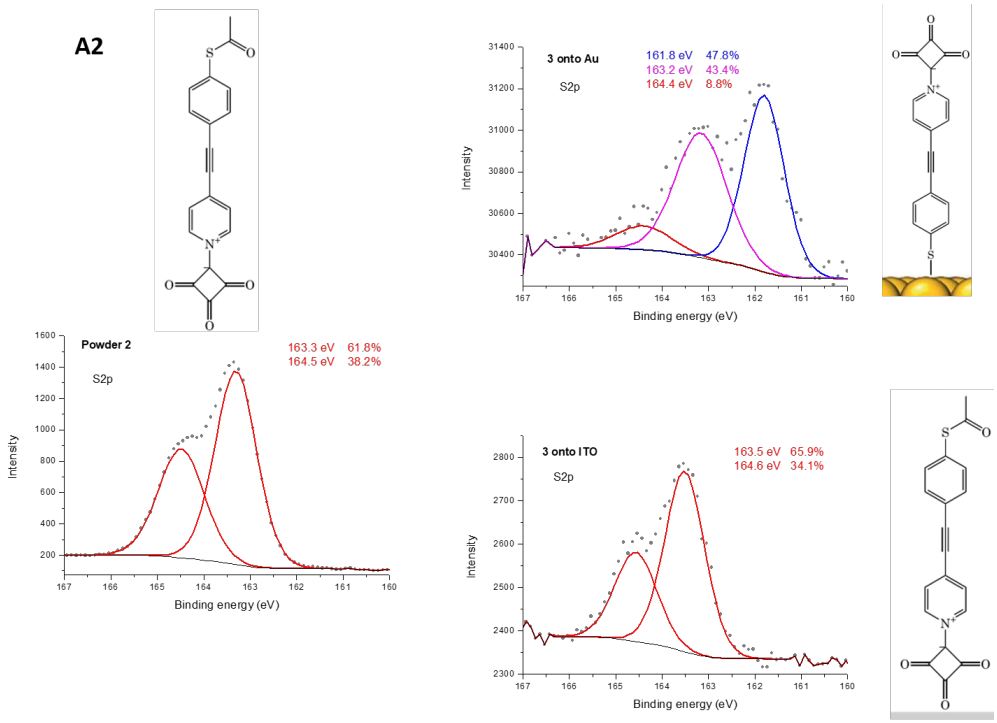


**Figure B.4** XPS results of **A2**.

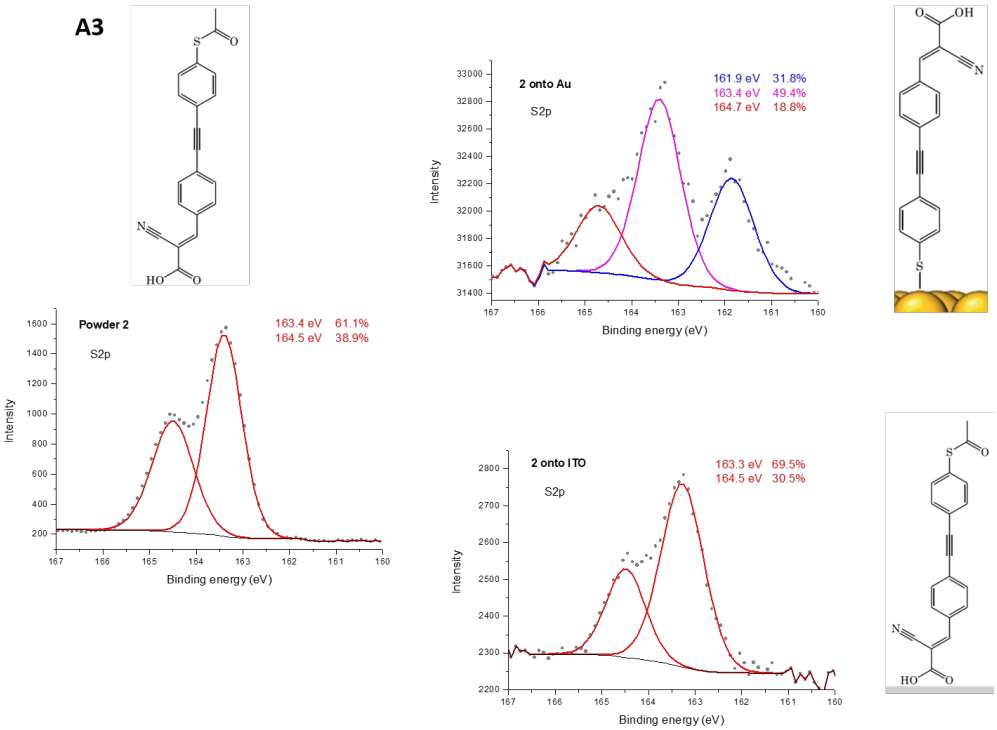


**Figure B.5** XPS results of **A2**.

# Appendix C

# Supplementary information for chapter 6

## C.1 Data for compounds 2Fe and 2Co

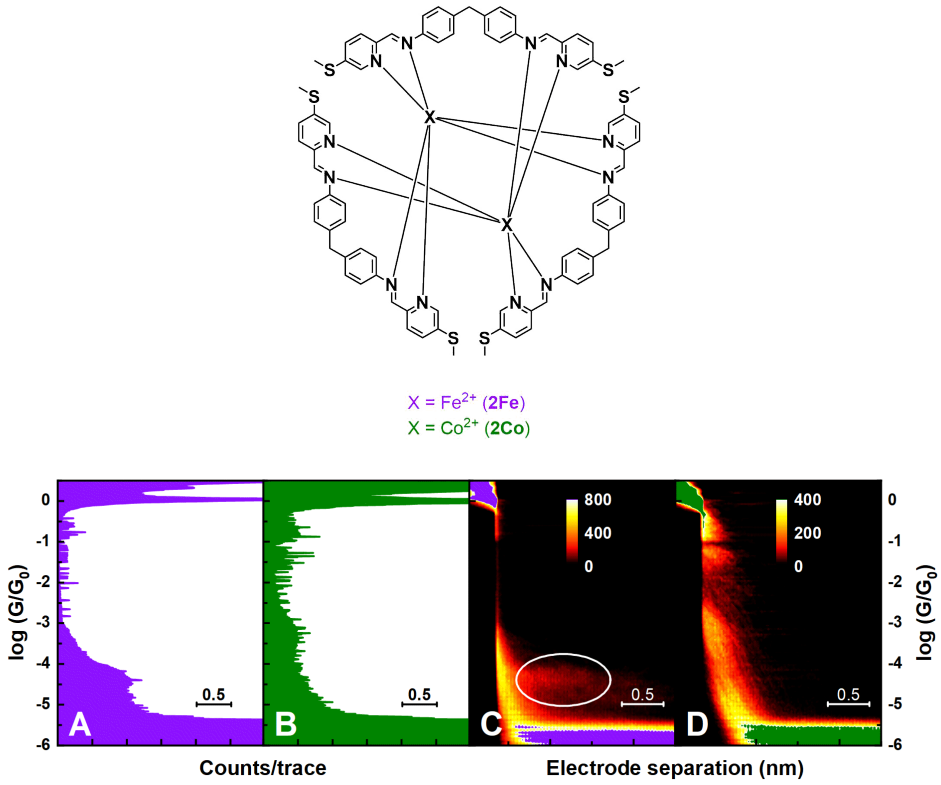


**Figure C.1** Molecular structure (top) and single-molecule conductance data (bottom) for **2Fe** (purple) and **2Co** (green) presented as one-dimensional (A, B) and two-dimensional histograms (C, D).

# Acknowledgements

A few lines will never be enough to express my gratitude and appreciation for the wonderful people in both my professional and personal life. That said, first and foremost, **Richard**, thank you for everything—from offering me the PhD position to your continued support until today. I am especially grateful for a perfect balance between giving me independence and always being available when I needed you.

**Andrea**, thank you for teaching me your ways, making fun of me at the right time, and patiently explaining countless times what an amplifier is. **David**, thank you for showing me how to connect a microscope. **Nico**, thank you for annoying the sh*t out of me in a way that was somehow charming, it was weirdly quiet after you left the group. **Paul**, man I like you both as a person and as a scientist, thank you deeply for all the fantastic moments we shared. And also thank you for adopting me into your home-base for six weeks last year, it was amazing!

Also a big thank you to all the people who supported me, believed in me, and made my time in Liverpool a great experience. Cheers to all of you: **Simon**, **Don**, **Saman**, **Eika**, **Matt**, **Maryam**, **Lucía**, **Ross**, **Masnun**, **DJ**, **Sara**, **Oday**, **Andy**, **Colin**, and **Santi**.

**Jurriaan**, thank you for putting me in touch with Mathias, and **Mathias**, thank you for putting me in touch with **Richard**. Without either of you, I would not have ended up studying molecular electronics in Liverpool. I have

had a blast during my four years spent there, which means I am very grateful to the both of you.

**Heike** and **Rick**, thanks to both of you for your guidance during the beginning of my PhD, especially for the valuable feedback in the vivas.

**Isma**, thank you for hiring me before I finished my PhD, I am both honoured and grateful for the opportunity you have given me. **Albert**, you b*stard, it has been a pleasure to meet you, and to get to know you a bit in the short period of approximately two months.

It may be obvious, but written works by people in the field have been invaluable. Especially books and reviews written by **Elke Scheer**, **Juan Carlos Cuevas**, **Supriyo Datta**, **Latha Venkataraman**, and **Xuefeng Guo** have been invaluable to me personally.

By far the greatest highlight of my time in Liverpool (outside the research circles), is the squish community. It started a little slow, but I have gained a tight group of friends over the years (some of which I will forget in this list): **Alex**, **Luke**, **Andy**, **Mo**, **Oliver**, **Dan**, **Eve**, **Kirsty**, **Katie**, **Catherine**, **Marsya**, **Chris**, and **Tom** from the student squash team. But also **Mark**, **Robert**, **James**, **Chris**, **Ivan**, and **Emmett** from the staff squash club.

**Cheryl**, **Piotr**, **Hahn**, **Kali**, and **Oliver**, thank you for being amazing friends!

**Dina**, muito obrigado por me fazer sentir bem-vindo desde do início. Eu estou sempre ansioso vos visitar.

In deze rij ga ik zeker mensen vergeten, maar aan al mijn vrienden in Nederland, jullie zijn toffe mensen en ik ben blij dat we af en toe kunnen rondhangen: **Julius**, **Tobias**, **Tim**, **Peter**, **Bas**, **Tias**, **Ben**, **Frank**, **Elwin**, **Aryan**, **Rick**, **Lars**, en **Marcel**

Mijn ouders, **Christie** en **Hans**, en mijn zusjes, **Laina** en **Daphne**, dankjulliewel voor alles, ik weet dat een simpel dankwoord nooit genoeg is, maar ik hoop dat jullie weten wat de steun voor mij betekent. De rest van de 'família' ook bedankt voor alle steun en lieve wensen: **Els**, **Willem**, **Marco**, **Steijn**, en **Danny**.

Last and most important, **Marta**, thank you so much for all your patience, understanding, and love! Eu amo-te muito, coelhinha. Eu também estou feliz que sentaste no meu lugar! Finalmente, vamos à Viena!

**Inco J. Planje**

*2019, September 30th*

# References


[1] H. Choi, C. C. Mody, "The Long History of Molecular Electronics: Microelectronics Origins of Nanotechnology", *Social Studies of Science* **2009**, *39*, 11–50, DOI 10.1177/0306312708097288 (cit. on p. 2).

[2] G. E. Moore, "Cramming more components onto integrated circuits", *Electronics* **1965**, *38*, 114–117, DOI 10.1109/jproc.1998.658762 (cit. on pp. 2, 3).

[3] D. Xiang, X. Wang, C. Jia, T. Lee, X. Guo, "Molecular-Scale Electronics: From Concept to Function", *Chemical Reviews* **2016**, *116*, 4318–4440, DOI 10.1021/acs.chemrev.5b00680 (cit. on pp. 2, 9, 34, 95).

[4] G. Binnig, H. Rohrer, C. Gerber, E. Weibel, "Surface Studies by Scanning Tunneling Microscopy", *Physical Review Letters* **1982**, *49*, 57–61, DOI 10.1103/PhysRevLett.49.57 (cit. on pp. 2, 10, 12).

[5] G. Binnig, C. F. Quate, C. Gerber, "Atomic Force Microscope", *Physical Review Letters* **1986**, *56*, 930–933, DOI 10.1103/PhysRevLett.56.930 (cit. on pp. 2, 11, 12).

[6] L. Hoddeson, "The Discovery of the Point-Contact Transistor", *Historical Studies in the Physical Sciences* **1981**, *12*, 41–76, DOI 10.2307/27757489 (cit. on p. 3).

[7] D. Kahng, "Electric field controlled semiconductor device", *US Patent 3102230* **1963**, 1–4 (cit. on p. 3).

[8] A. von Hippel, "Molecular Engineering", *Science* **1956**, *123*, 315–317, DOI 10.1126/science.123.3191.315 (cit. on p. 3).

[9] R. P. Feynman, "There is plenty of room at bottom", *Engineering and Science* **1960**, *23*, 22–36 (cit. on p. 3).

[10] B. Mann, H. Kuhn, "Tunneling through Fatty Acid Salt Monolayers", *Journal of Applied Physics* **1971**, *42*, 4398–4405, DOI 10.1063/1.1659785 (cit. on p. 4).

[11] A. Aviram, M. A. Ratner, "Molecular rectifiers", *Chemical Physics Letters* **1974**, *29*, 277–283, DOI 10.1016/0009-2614(74)85031-1 (cit. on p. 4).

[12] T. A. Su, M. Neupane, M. L. Steigerwald, L. Venkataraman, C. Nuckolls, "Chemical principles of single-molecule electronics", *Nature Reviews Materials* **2016**, *1*, 16002, DOI 10.1038/natrevmats.2016.2 (cit. on pp. 5, 95).

[13] M. Paulsson, S. Datta, "Thermoelectric effect in molecular electronics", *Physical Review B* **2003**, *67*, 241403, DOI 10.1103/PhysRevB.67.241403 (cit. on pp. 6, 64).

[14] J. A. Malen, P. Doak, K. Baheti, T. Don Tilley, R. A. Segalman, A. Majumdar, "Identifying the length dependence of orbital alignment and contact coupling in molecular heterojunctions", *Nano Letters* **2009**, *9*, 1164–1169, DOI 10.1021/nl803814f (cit. on p. 6).

[15] A. Danilov, S. Kubatkin, S. Kafanov, P. Hedegård, N. Stuhr-Hansen, K. Moth-Poulsen, T. Bjørnholm, "Electronic transport in single molecule junctions: Control of the molecule-electrode coupling through intramolecular tunneling barriers", *Nano Letters* **2008**, *8*, 1–5, DOI 10.1021/nl071228o (cit. on p. 6).

[16] F. Chen, X. Li, J. Hihath, Z. Huang, N. Tao, "Effect of anchoring groups on single-molecule conductance: Comparative study of thiol-, amine-, and carboxylic-acid-terminated molecules", *Journal of the American Chemical Society* **2006**, *128*, 15874–15881, DOI 10.1021/ja065864k (cit. on pp. 7, 15, 17, 72).

[17] L. A. Zotti, T. Kirchner, J.-C. Cuevas, F. Pauly, T. Huhn, E. Scheer, A. Erbe, "Revealing the Role of Anchoring Groups in the Electrical Conduction Through Single-Molecule Junctions", *Small* **2010**, *6*, 1529–1535, DOI 10.1002/smll.200902227 (cit. on p. 7).

[18] L. Venkataraman, J. E. Klare, I. W. Tam, C. Nuckolls, "Single-Molecule Circuits with Well-Defined Molecular Conductance", *Nano Letters* **2006**, *6*, 458–462, DOI 10.1021/nl052373+ (cit. on p. 7).

[19] E. J. Dell, B. Capozzi, K. H. Dubay, T. C. Berkelbach, J. R. Moreno, D. R. Reichman, L. Venkataraman, L. M. Campos, "Impact of molecular symmetry on single-molecule conductance", *Journal of the American Chemical Society* **2013**, *135*, 11724–11727, DOI 10.1021/ja4055367 (cit. on p. 7).

[20] M. Kamenetska, S. Y. Quek, A. C. Whalley, M. L. Steigerwald, H. J. Choi, S. G. Louie, C. Nuckolls, M. S. Hybertsen, J. B. Neaton, L. Venkataraman, "Conductance and Geometry of Pyridine-Linked Single-Molecule Junctions", *Journal of the American Chemical Society* **2010**, *132*, 6817–6821, DOI 10.1021/ja1015348 (cit. on p. 7).

[21] Z.-L. Cheng, R. Skouta, H. Vazquez, J. R. Widawsky, S. Schneebeli, W. Chen, M. S. Hybertsen, R. Breslow, L. Venkataraman, "In situ formation of highly conducting covalent Au-C contacts for single-molecule junctions.", *Nature nanotechnology* **2011**, *6*, 353–357, DOI 10.1038/nnano.2011.66 (cit. on pp. 7, 95).

[22] M. A. Reed, C. Zhou, C. J. Muller, T. P. Burgin, J. M. Tour, "Conductance of a molecular junction", *Science* **1997**, *278*, 252–254, DOI 10.1126/science.278.5336.252 (cit. on p. 7).

[23] C. Muller, J. van Ruitenbeek, L. de Jongh, "Experimental observation of the transition from weak link to tunnel junction", *Physica C: Superconductivity* **1992**, *191*, 485–504, DOI 10.1016/0921-4534(92)90947-B (cit. on p. 7).

[24] A. F. Morpurgo, C. M. Marcus, D. B. Robinson, "Controlled fabrication of metallic electrodes with atomic separation", *Applied Physics Letters* **1999**, *74*, 2084–2086, DOI 10.1063/1.123765 (cit. on p. 8).

[25] H. Park, A. K. L. Lim, A. P. Alivisatos, J. Park, P. L. McEuen, "Fabrication of metallic electrodes with nanometer separation by electromigration", *Applied Physics Letters* **1999**, *75*, 301–303, DOI 10.1063/1.124354 (cit. on p. 8).

[26] H. Park, J. Park, A. K. L. Lim, E. H. Anderson, A. P. Alivisatos, P. L. McEuen, "Nanomechanical oscillations in a single-C60 transistor", *Nature* **2000**, *407*, 57–60, DOI 10.1038/35024031 (cit. on p. 8).

[27] S. Iijima, "Helical microtubules of graphitic carbon", *Nature* **1991**, *354*, 56–58, DOI 10.1038/354056a0 (cit. on p. 8).

[28] P. M. Ajayan, "Nanotubes from Carbon", *Chemical Reviews* **1999**, *99*, 1787–1800, DOI 10.1021/cr970102g (cit. on p. 8).

[29] P. G. Collins, M. S. Arnold, P. Avouris, "Engineering carbon nanotubes and nanotube circuits using electrical breakdown", *Science* **2001**, *292*, 706–709, DOI 10.1126/science.1058782 (cit. on p. 8).

[30] X. Guo, J. P. Small, J. E. Klare, Y. Wang, M. S. Purewal, I. W. Tam, B. H. Hong, R. Caldwell, L. Huang, S. O'Brien, J. Yan, R. Breslow, S. J. Wind, J. Hone, P. Kim, C. Nuckolls, "Covalently Bridging Gaps in

Single-Walled Carbon Nanotubes with Conducting Molecules", *Science* **2006**, *311*, 356–359, DOI 10.1126/science.1120986 (cit. on p. 8).

[31] M. Palma, W. Wang, E. Penzo, J. Brathwaite, M. Zheng, J. Hone, C. Nuckolls, S. J. Wind, "Controlled Formation of Carbon Nanotube Junctions via Linker-Induced Assembly in Aqueous Solution", *Journal of the American Chemical Society* **2013**, *135*, 8440–8443, DOI 10.1021/ja4018072 (cit. on p. 8).

[32] K. S. Novoselov, A. K. Geim, S. V. Morozov, D. Jiang, Y. Zhang, S. V. Dubonos, I. V. Grigorieva, A. A. Firsov, "Electric field in atomically thin carbon films", *Science* **2004**, *306*, 666–669, DOI 10.1126/science.1102896 (cit. on p. 8).

[33] F. Prins, A. Barreiro, J. W. Ruitenberg, J. S. Seldenthuis, N. Aliaga-Alcalde, L. M. Vandersypen, H. S. Van Der Zant, "Room-temperature gating of molecular junctions using few-layer graphene nanogap electrodes", *Nano Letters* **2011**, *11*, 4607–4611, DOI 10.1021/nl202065x (cit. on p. 8).

[34] Y. Cao, S. Dong, S. Liu, L. He, L. Gan, X. Yu, M. L. Steigerwald, X. Wu, Z. Liu, X. Guo, "Building High-Throughput Molecular Junctions Using Indented Graphene Point Contacts", *Angewandte Chemie International Edition* **2012**, *51*, 12228–12232, DOI 10.1002/anie.201205607 (cit. on p. 8).

[35] S. Tao, Q. Zhang, C. He, X. Lin, R. Xie, C. Zhao, C. Zhao, A. Smogunov, Y. J. Dappe, R. J. Nichols, L. Yang, "Graphene-Contacted Single Molecular Junctions with Conjugated Molecular Wires", *ACS Applied Nano Materials* **2019**, *2*, 12–18, DOI 10.1021/acsanm.8b01379 (cit. on p. 8).

[36] J. He, B. Chen, A. K. Flatt, J. J. Stephenson, C. D. Doyle, J. M. Tour, "Metal-free silicon–molecule–nanotube testbed and memory device", *Nature Materials* **2006**, *5*, 63–68, DOI 10.1038/nmat1526 (cit. on p. 8).

[37] G. J. Ashwell, L. J. Phillips, B. J. Robinson, B. Urasinska-Wojcik, C. J. Lambert, I. M. Grace, M. R. Bryce, R. Jitchati, M. Tavasli, T. I. Cox, I. C. Sage, R. P. Tuffin, S. Ray, "Molecular Bridging of Silicon Nanogaps", *ACS Nano* **2010**, *4*, 7401–7406, DOI 10.1021/nn102460z (cit. on p. 8).

[38] A. C. Aragonès, N. Darwish, S. Ciampi, F. Sanz, J. J. Gooding, I. Díez-Pérez, "Single-molecule electrical contacts on silicon electrodes under ambient conditions", *Nature Communications* **2017**, *8*, 15056, DOI 10.1038/ncomms15056 (cit. on p. 8).

[39] H. Atesci, V. Kaliginedi, J. A. Celis Gil, H. Ozawa, J. M. Thijssen, P. Broekmann, M.-a. Haga, S. J. van der Molen, "Humidity-controlled rectification switching in ruthenium-complex molecular junctions", *Nature Nanotechnology* **2018**, *13*, 117–121, DOI 10.1038/s41565-017-0016-8 (cit. on p. 8).

[40] A. Vezzoli, R. J. Brooke, N. Ferri, S. J. Higgins, W. Schwarzacher, R. J. Nichols, "Single-Molecule Transport at a Rectifying GaAs Contact", *Nano Letters* **2017**, *17*, 1109–1115, DOI 10.1021/acs.nanolett.6b04663 (cit. on p. 8).

[41] Y. Okawa, S. K. Mandal, C. Hu, Y. Tateyama, S. Goedecker, S. Tsukamoto, T. Hasegawa, J. K. Gimzewski, M. Aono, "Chemical Wiring and Soldering toward All-Molecule Electronic Circuitry", *Journal of the American Chemical Society* **2011**, *133*, 8227–8233, DOI 10.1021/ja111673x (cit. on p. 8).

[42] K. Slowinski, H. K. Y. Fong, M. Majda, "Mercury−Mercury Tunneling Junctions. 1. Electron Tunneling Across Symmetric and Asymmetric Alkanethiolate Bilayers", *Journal of the American Chemical Society* **1999**, *121*, 7257–7261, DOI 10.1021/ja991613i (cit. on p. 9).

[43] R. C. Chiechi, E. A. Weiss, M. D. Dickey, G. M. Whitesides, "Eutectic Gallium–Indium (EGaIn): A Moldable Liquid Metal for Electrical Characterization of Self-Assembled Monolayers", *Angewandte Chemie International Edition* **2008**, *47*, 142–144, DOI 10.1002/anie.200703642 (cit. on p. 9).

[44] A. Vilan, D. Cahen, "Soft Contact Deposition onto Molecularly Modified GaAs. Thin Metal Film Flotation: Principles and Electrical Effects", *Advanced Functional Materials* **2002**, *12*, 795–807, DOI 10.1002/adfm.200290009 (cit. on p. 9).

[45] Y.-L. Loo, D. V. Lang, J. A. Rogers, J. W. P. Hsu, "Electrical Contacts to Molecular Layers by Nanotransfer Printing", *Nano Letters* **2003**, *3*, 913–917, DOI 10.1021/nl034207c (cit. on p. 9).

[46] J. G. Kushmerick, J. Naciri, J. C. Yang, R. Shashidhar, "Conductance Scaling of Molecular Wires in Parallel", *Nano Letters* **2003**, *3*, 897–900, DOI 10.1021/nl034201n (cit. on p. 9).

[47] K. T. Shimizu, J. D. Fabbri, J. J. Jelincic, N. A. Melosh, "Soft Deposition of Large-Area Metal Contacts for Molecular Electronics", *Advanced Materials* **2006**, *18*, 1499–1504, DOI 10.1002/adma.200600195 (cit. on p. 9).

[48] J. Tang, Y. Wang, J. E. Klare, G. S. Tulevski, S. J. Wind, C. Nuckolls, "Encoding Molecular-Wire Formation within Nanoscale Sockets", *Angewandte Chemie International Edition* **2007**, *46*, 3892–3895, DOI 10.1002/anie.200604398 (cit. on p. 9).

[49] J. Chen, M. A. Reed, A. M. Rawlett, J. M. Tour, "Large on-off ratios and negative differential resistance in a molecular electronic device", *Science* **1999**, *286*, 1550–1552, DOI 10.1126/science.286.5444.1550 (cit. on p. 9).

[50] N. Majumdar, N. Gergel, D. Routenberg, J. C. Bean, L. R. Harriott, B. Li, L. Pu, Y. Yao, J. M. Tour, "Nanowell device for the electrical characterization of metal–molecule–metal junctions", *Journal of Vacuum Science & Technology B: Microelectronics and Nanometer Structures* **2005**, *23*, 1417, DOI 10.1116/1.1935528 (cit. on p. 9).

[51] J. K. N. Mbindyo, T. E. Mallouk, J. B. Mattzela, I. Kratochvilova, B. Razavi, T. N. Jackson, T. S. Mayer, "Template Synthesis of Metal Nanowires Containing Monolayer Molecular Junctions", *Journal of the American Chemical Society* **2002**, *124*, 4020–4026, DOI 10.1021/ja016696t (cit. on p. 9).

[52] H. B. Akkerman, P. W. M. Blom, D. M. De Leeuw, B. De Boer, "Towards molecular electronics with large-area molecular junctions", *Nature* **2006**, *441*, 69–72, DOI 10.1038/nature04699 (cit. on p. 9).

[53] P. Tyagi, "Multilayer edge molecular electronics devices: a review", *Journal of Materials Chemistry* **2011**, *21*, 4733, DOI 10.1039/c0jm03291c (cit. on p. 9).

[54] C. A. Nijhuis, W. F. Reus, J. R. Barber, M. D. Dickey, G. M. Whitesides, "Charge Transport and Rectification in Arrays of SAM-Based Tunneling Junctions", *Nano Letters* **2010**, *10*, 3611–3619, DOI 10.1021/nl101918m (cit. on p. 9).

[55] M. L. Pedano, S. Li, G. C. Schatz, C. A. Mirkin, "Periodic Electric Field Enhancement Along Gold Rods with Nanogaps", *Angewandte Chemie International Edition* **2010**, *49*, 78–82, DOI 10.1002/anie.200904646 (cit. on p. 10).

[56] B. Y. Lee, K. Heo, A. L. Schmucker, H. J. Jin, J. K. Lim, T. Kim, H. Lee, K.-S. Jeon, Y. D. Suh, C. A. Mirkin, S. Hong, "Nanotube-Bridged Wires with Sub-10 nm Gaps", *Nano Letters* **2012**, *12*, 1879–1884, DOI 10.1021/nl204259t (cit. on p. 10).

[57] H. Y. Yu, C. S. Ah, I.-B. Baek, A. Kim, J.-H. Yang, C.-G. Ahn, C. W. Park, B. H. Kim, "Nanogap Array Fabrication Using Doubly Clamped Freestanding Silicon Nanowires and Angle Evaporations", *ETRI Journal* **2009**, *31*, 351–356, DOI 10.4218/etrij.09.0109.0006 (cit. on p. 10).

[58] S. Seo, M. Min, S. M. Lee, H. Lee, "Photo-switchable molecular monolayer anchored between highly transparent and flexible graphene electrodes", *Nature Communications* **2013**, *4*, 1920, DOI 10.1038/ncomms2937 (cit. on p. 10).

[59] V. Dubois, S. N. Raja, P. Gehring, S. Caneva, H. S. van der Zant, F. Niklaus, G. Stemme, "Massively parallel fabrication of crack-defined gold break junctions featuring sub-3 nm gaps for molecular devices", *Nature Communications* **2018**, *9*, 3433, DOI 10.1038/s41467-018-05785-2 (cit. on p. 10).

[60] A. P. Bonifas, R. L. McCreery, "'Soft' Au, Pt and Cu contacts for molecular junctions through surface-diffusion-mediated deposition", *Nature Nanotechnology* **2010**, *5*, 612–617, DOI 10.1038/nnano.2010.115 (cit. on p. 10).

[61] A. P. Bonifas, R. L. McCreery, "Assembling Molecular Electronic Junctions One Molecule at a Time", *Nano Letters* **2011**, *11*, 4725–4729, DOI 10.1021/nl202495k (cit. on p. 10).

[62] G. Binnig, H. Rohrer, C. Gerber, E. Weibel, "Tunneling through a controllable vacuum gap", *Applied Physics Letters* **1982**, *40*, 178–180, DOI 10.1063/1.92999 (cit. on p. 10).

[63] J. Tersoff, D. R. Hamann, "Theory of the scanning tunneling microscope", *Physical Review B* **1985**, *31*, 805–813, DOI 10.1103/PhysRevB.31.805 (cit. on p. 11).

[64] A. Aviram, C. Joachim, M. Pomerantz, "Evidence of switching and rectification by a single molecule effected with a scanning tunneling microscope", *Chemical Physics Letters* **1988**, *146*, 490–495, DOI 10.1016/0009-2614(88)87486-4 (cit. on p. 11).

[65] D. J. Wold, C. D. Frisbie, "Formation of Metal−Molecule−Metal Tunnel Junctions: Microcontacts to Alkanethiol Monolayers with a Conducting AFM Tip", *Journal of the American Chemical Society* **2000**, *122*, 2970–2971, DOI 10.1021/ja994468h (cit. on pp. 11, 12).

[66] X. D. Cui, A. Primak, X. Zarate, J. Tomfohr, O. F. Sankey, A. L. Moore, T. A. Moore, D. Gust, G. Harris, S. M. Lindsay, "Reproducible Measurement of Single-Molecule Conductivity", *Science* **2001**, *294*, 571–575, DOI 10.1126/science.1064354 (cit. on p. 11).

[67] B. Xu, "Measurement of Single-Molecule Resistance by Repeated Formation of Molecular Junctions", *Science* **2003**, *301*, 1221–1223, DOI 10.1126/science.1087481 (cit. on pp. 12, 13, 70).

[68] B. J. van Wees, H. van Houten, C. W. J. Beenakker, J. G. Williamson, L. P. Kouwenhoven, D. van der Marel, C. T. Foxon, "Quantized conductance of point contacts in a two-dimensional electron gas", *Physical Review Letters* **1988**, *60*, 848–850, DOI 10.1103/PhysRevLett.60.848 (cit. on p. 12).

[69] W. Haiss, H. V. Zalinge, S. J. Higgins, D. Bethell, H. Höbenreich, D. J. Schiffrin, R. J. Nichols, "Redox State Dependence of Single Molecule Conductivity", *J. Amer. Chem. Soc.* **2003**, *125*, 15294–15295, DOI 10.1021/ja038214e (cit. on p. 13).

[70] W. Haiss, R. J. Nichols, H. van Zalinge, S. J. Higgins, D. Bethell, D. J. Schiffrin, "Measurement of single molecule conductivity using the spontaneous formation of molecular wires", *Physical Chemistry Chemical Physics* **2004**, *6*, 4330, DOI 10.1039/b404929b (cit. on pp. 13, 14).

[71] R. J. Nichols, W. Haiss, S. J. Higgins, E. Leary, S. Martin, D. Bethell, "The experimental determination of the conductance of single molecules", *Physical Chemistry Chemical Physics* **2010**, *12*, 2801, DOI 10.1039/b922000c (cit. on p. 14).

[72] P. Darancet, J. R. Widawsky, H. J. Choi, L. Venkataraman, J. B. Neaton, "Quantitative current-voltage characteristics in molecular junctions from first principles", *Nano Letters* **2012**, *12*, 6250–6254, DOI 10.1021/nl3033137 (cit. on p. 15).

[73] Y. S. Park, A. C. Whalley, M. Kamenetska, M. L. Steigerwald, M. S. Hybertsen, C. Nuckolls, L. Venkataraman, "Contact Chemistry and Single-Molecule Conductance: A Comparison of Phosphines, Methyl Sulfides, and Amines", *Journal of the American Chemical Society* **2007**, *129*, 15768–15769, DOI 10.1021/ja0773857 (cit. on pp. 15–17).

[74] C. A. Martin, D. Ding, J. K. Sørensen, T. Bjørnholm, J. M. Van Ruitenbeek, H. S. Van Der Zant, "Fullerene-based anchoring groups for molecular electronics", *Journal of the American Chemical Society* **2008**, *130*, 13198–13199, DOI 10.1021/ja804699a (cit. on p. 15).

[75] W. Chen, J. R. Widawsky, H. Vázquez, S. T. Schneebeli, M. S. Hybertsen, R. Breslow, L. Venkataraman, "Highly conducting $\pi$-conjugated molecular junctions covalently bonded to gold electrodes", *Journal of the American Chemical Society* **2011**, *133*, 17160–17163, DOI 10.1021/ja208020j (cit. on p. 15).

[76] P. Pla-Vilanova, A. C. A. Aragonès, S. Ciampi, F. Sanz, N. Darwish, I. Diez-Perez, "The spontaneous formation of single-molecule junctions via terminal alkynes", *Nanotechnology* **2015**, *26*, 381001, DOI 10.1088/0957-4484/26/38/381001 (cit. on p. 15).

[77] W. Hong, D. Z. Manrique, P. Moreno-García, M. Gulcur, A. Mishchenko, C. J. Lambert, M. R. Bryce, T. Wandlowski, "Single Molecular Conduc-

tance of Tolanes: Experimental and Theoretical Study on the Junction Evolution Dependent on the Anchoring Group", *Journal of the American Chemical Society* **2012**, *134*, 2292–2304, DOI 10.1021/ja209844r (cit. on pp. 16, 17, 50, 81).

[78] A. Salomon, D. Cahen, S. Lindsay, J. Tomfohr, V. Engelkes, C. Frisbie, "Comparison of Electronic Transport Measurements on Organic Molecules", *Advanced Materials* **2003**, *15*, 1881–1890, DOI 10.1002/adma.200306091 (cit. on p. 18).

[79] Z. Xie, I. Bâldea, C. D. Frisbie, "Determination of Energy-Level Alignment in Molecular Tunnel Junctions by Transport and Spectroscopy: Self-Consistency for the Case of Oligophenylene Thiols and Dithiols on Ag, Au, and Pt Electrodes", *Journal of the American Chemical Society* **2019**, *141*, 3670–3681, DOI 10.1021/jacs.8b13370 (cit. on pp. 18, 63).

[80] S. H. Choi, B. S. Kim, C. D. Frisbie, "Electrical resistance of long conjugated molecular wires", *Science* **2008**, *320*, 1482–1486, DOI 10.1126/science.1156538 (cit. on pp. 19, 20).

[81] W. Ho, "Single-molecule chemistry", *The Journal of Chemical Physics* **2002**, *117*, 11033–11061, DOI 10.1063/1.1521153 (cit. on p. 19).

[82] S. V. Aradhya, L. Venkataraman, "Single-molecule junctions beyond electronic transport", *Nature Nanotechnology* **2013**, *8*, 399–410, DOI 10.1038/nnano.2013.91 (cit. on p. 20).

[83] M. Galperin, A. Nitzan, "Molecular optoelectronics: the interaction of molecular conduction junctions with light", *Physical Chemistry Chemical Physics* **2012**, *14*, 9421, DOI 10.1039/c2cp40636e (cit. on p. 20).

[84] J. Zhou, C. Guo, B. Xu, "Electron transport properties of single molecular junctions under mechanical modulations", *Journal of Physics: Con-*

*densed Matter* **2012**, *24*, 164209, DOI 10.1088/0953-8984/24/16/164209 (cit. on p. 20).

[85] Y. Dubi, M. Di Ventra, "Colloquium : Heat flow and thermoelectricity in atomic and molecular junctions", *Reviews of Modern Physics* **2011**, *83*, 131–155, DOI 10.1103/RevModPhys.83.131 (cit. on pp. 20, 21).

[86] S. Sanvito, "Molecular spintronics", *Chemical Society Reviews* **2011**, *40*, 3336, DOI 10.1039/c1cs15047b (cit. on p. 20).

[87] T. Deckert-Gaudig, A. Taguchi, S. Kawata, V. Deckert, "Tip-enhanced Raman spectroscopy – from early developments to recent advances", *Chemical Society Reviews* **2017**, *46*, 4077–4110, DOI 10.1039/C7CS00209B (cit. on p. 20).

[88] A. B. S. Elliott, R. Horvath, K. C. Gordon, "Vibrational spectroscopy as a probe of molecule-based devices", *Chem. Soc. Rev.* **2012**, *41*, 1929–1946, DOI 10.1039/C1CS15208D (cit. on p. 20).

[89] Y. Kim, H. Song, "Investigation of molecular junctions with inelastic electron tunneling spectroscopy", *Applied Spectroscopy Reviews* **2016**, *51*, 603–620, DOI 10.1080/05704928.2016.1166435 (cit. on p. 20).

[90] H. Song, Y. Kim, Y. H. Jang, H. Jeong, M. A. Reed, T. Lee, "Observation of molecular orbital gating", *Nature* **2009**, *462*, 1039–1043, DOI 10.1038/nature08639 (cit. on p. 20).

[91] C. Bruot, J. Hihath, N. Tao, "Mechanically controlled molecular orbital alignment in single molecule junctions", *Nature Nanotechnology* **2012**, *7*, 35–40, DOI 10.1038/nnano.2011.212 (cit. on p. 20).

[92] B. Xu, X. Xiao, N. Tao, "Measurements of Single-Molecule Electromechanical Properties", *Journal of the American Chemical Society* **2003**, *125*, 16164–16165, DOI 10.1021/ja038949j (cit. on p. 20).

[93] E. J. Dell, B. Capozzi, J. Xia, L. Venkataraman, L. M. Campos, "Molecular length dictates the nature of charge carriers in single-molecule junctions of oxidized oligothiophenes", *Nature Chemistry* **2015**, *7*, 209–214, DOI 10.1038/nchem.2160 (cit. on p. 21).

[94] H. Sadeghi, "Discriminating Seebeck sensing of molecules", *Physical Chemistry Chemical Physics* **2019**, *21*, 2378–2381, DOI 10.1039/c8cp05991h (cit. on p. 21).

[95] N. Mosso, U. Drechsler, F. Menges, P. Nirmalraj, S. Karg, H. Riel, B. Gotsmann, "Heat transport through atomic contacts", *Nature Nanotechnology* **2017**, *12*, 430–433, DOI 10.1038/nnano.2016.302 (cit. on p. 21).

[96] L. Cui, S. Hur, Z. A. Akbar, J. C. Klöckner, W. Jeong, F. Pauly, S.-Y. Jang, P. Reddy, E. Meyhofer, "Thermal conductance of single-molecule junctions", *Nature* **2019**, *572*, 628–633, DOI 10.1038/s41586-019-1420-z (cit. on p. 21).

[97] J. M. Beebe, B. Kim, J. W. Gadzuk, C. Daniel Frisbie, J. G. Kushmerick, "Transition from Direct Tunneling to Field Emission in Metal-Molecule-Metal Junctions", *Physical Review Letters* **2006**, *97*, 026801, DOI 10.1103/PhysRevLett.97.026801 (cit. on pp. 21, 33).

[98] S. Guo, J. Hihath, I. Díez-Pérez, N. Tao, "Measurement and statistical analysis of single-molecule current-voltage characteristics, transition voltage spectroscopy, and tunneling barrier height", *Journal of the American Chemical Society* **2011**, *133*, 19189–19197, DOI 10.1021/ja2076857 (cit. on p. 21).

[99] J. Repp, G. Meyer, S. M. Stojković, A. Gourdon, C. Joachim, "Molecules on Insulating Films: Scanning-Tunneling Microscopy Imaging of Individual Molecular Orbitals", *Physical Review Letters* **2005**, *94*, 026803, DOI 10.1103/PhysRevLett.94.026803 (cit. on p. 21).

[100] A. C. Aragonès, N. L. Haworth, N. Darwish, S. Ciampi, N. J. Bloomfield, G. G. Wallace, I. Diez-Perez, M. L. Coote, "Electrostatic catalysis of a Diels–Alder reaction", *Nature* **2016**, *531*, 88–91, DOI 10.1038/nature16989 (cit. on p. 21).

[101] X. Huang, C. Tang, J. Li, L.-C. Chen, J. Zheng, P. Zhang, J. Le, R. Li, X. Li, J. Liu, Y. Yang, J. Shi, Z. Chen, M. Bai, H.-L. Zhang, H. Xia, J. Cheng, Z.-Q. Tian, W. Hong, "Electric field–induced selective catalysis of single-molecule reaction", *Science Advances* **2019**, *5*, eaaw3072, DOI 10.1126/sciadv.aaw3072 (cit. on p. 21).

[102] J. L. Zhang, J. Q. Zhong, J. D. Lin, W. P. Hu, K. Wu, G. Q. Xu, A. T. S. Wee, W. Chen, "Towards single molecule switches", *Chem. Soc. Rev.* **2015**, *44*, 2998–3022, DOI 10.1039/C4CS00377B (cit. on p. 21).

[103] F. Q. Xie, L. Nittler, C. Obermair, T. Schimmel, "Gate-controlled atomic quantum switch", *Physical Review Letters* **2004**, *93*, 128303, DOI 10.1103/PhysRevLett.93.128303 (cit. on p. 22).

[104] S. Sanvito, "Ab-initio methods for spin-transport at the nanoscale level", *arXiv e-prints* **2005**, cond–mat/0503445 (cit. on p. 27).

[105] D. Xiang, PhD thesis, Aachen University, **2012** (cit. on p. 30).

[106] S. Bock, PhD thesis, University of Western Australia, **2017**, DOI 10.4225/23/5a31d551caeea (cit. on p. 36).

[107] B. Ren, G. Picardi, B. Pettinger, "Preparation of gold tips suitable for tip-enhanced Raman spectroscopy and light emission by electrochemical etching", *Review of Scientific Instruments* **2004**, *75*, 837–841, DOI 10.1063/1.1688442 (cit. on p. 37).

[108] W. Haiss, D. Lackey, J. K. Sass, K. H. Besocke, "Atomic resolution scanning tunneling microscopy images of Au(111) surfaces in air and

polar organic solvents", *The Journal of Chemical Physics* **1991**, *95*, 2193–2196, DOI 10.1063/1.460967 (cit. on p. 38).

[109] M. Chockalingam, N. Darwish, G. Le Saux, J. J. Gooding, "Importance of the Indium Tin Oxide Substrate on the Quality of Self-Assembled Monolayers Formed from Organophosphonic Acids", *Langmuir* **2011**, *27*, 2545–2552, DOI 10.1021/la104464w (cit. on pp. 38, 75).

[110] H. Ohnishi, Y. Kondo, K. Takayanagi, "Quantized conductance through individual rows of suspended gold atoms", *Nature* **1998**, *395*, 780–783, DOI 10.1038/27399 (cit. on p. 42).

[111] A. I. Yanson, G. R. Bollinger, H. E. van den Brom, N. Agraït, J. M. van Ruitenbeek, "Formation and manipulation of a metallic wire of single gold atoms", *Nature* **1998**, *395*, 783–785, DOI 10.1038/27405 (cit. on p. 42).

[112] I. Horcas, R. Fernández, J. M. Gómez-Rodríguez, J. Colchero, J. Gómez-Herrero, A. M. Baro, "WSXM: A software for scanning probe microscopy and a tool for nanotechnology", *Review of Scientific Instruments* **2007**, *78*, 013705, DOI 10.1063/1.2432410 (cit. on p. 44).

[113] J. Hrbac, V. Halouzka, L. Trnkova, J. Vacek, "eL-Chem Viewer: A Freeware Package for the Analysis of Electroanalytical Data and Their Post-Acquisition Processing", *Sensors* **2014**, *14*, 13943–13954, DOI 10.3390/s140813943 (cit. on p. 45).

[114] D. C. Milan, A. Vezzoli, I. J. Planje, P. J. Low, "Metal bis(acetylide) complex molecular wires: concepts and design strategies", *Dalton Transactions* **2018**, *47*, 14125–14138, DOI 10.1039/C8DT02103A (cit. on pp. 47, 48, 96).

[115] S. Y. Quek, M. Kamenetska, M. L. Steigerwald, H. J. Choi, S. G. Louie, M. S. Hybertsen, J. B. Neaton, L. Venkataraman, "Mechanically

controlled binary conductance switching of a single-molecule junction", *Nature Nanotechnology* **2009**, *4*, 230–234, DOI 10.1038/nnano.2009.10 (cit. on p. 50).

[116] W. R. French, C. R. Iacovella, I. Rungger, A. M. Souza, S. Sanvito, P. T. Cummings, "Structural Origins of Conductance Fluctuations in Gold–Thiolate Molecular Transport Junctions", *The Journal of Physical Chemistry Letters* **2013**, *4*, 887–891, DOI 10.1021/jz4001104 (cit. on p. 51).

[117] R. J. Davidson, D. C. Milan, O. A. Al-Owaedi, A. K. Ismael, R. J. Nichols, S. J. Higgins, C. J. Lambert, D. S. Yufit, A. Beeby, "Conductance of 'bare-bones' tripodal molecular wires", *RSC Advances* **2018**, *8*, 23585–23590, DOI 10.1039/C8RA01257A (cit. on p. 51).

[118] W. Haiss, C. Wang, I. Grace, A. S. Batsanov, D. J. Schiffrin, S. J. Higgins, M. R. Bryce, C. J. Lambert, R. J. Nichols, "Precision control of single-molecule electrical junctions", *Nature Materials* **2006**, *5*, 995–1002, DOI 10.1038/nmat1781 (cit. on p. 51).

[119] M. Kamenetska, M. Koentopp, A. C. Whalley, Y. S. Park, M. L. Steigerwald, C. Nuckolls, M. S. Hybertsen, L. Venkataraman, "Formation and evolution of single-molecule junctions", *Physical Review Letters* **2009**, *102*, 2–5, DOI 10.1103/PhysRevLett.102.126803 (cit. on p. 51).

[120] S. J. Higgins, R. J. Nichols, "Metal/molecule/metal junction studies of organometallic and coordination complexes; What can transition metals do for molecular electronics?", *Polyhedron* **2018**, *140*, 25–34, DOI 10.1016/j.poly.2017.10.022 (cit. on p. 55).

[121] O. A. Al-Owaedi, S. Bock, D. C. Milan, M.-C. Oerthel, M. S. Inkpen, D. S. Yufit, A. N. Sobolev, N. J. Long, T. Albrecht, S. J. Higgins, M. R. Bryce, R. J. Nichols, C. J. Lambert, P. J. Low, "Insulated molecular wires: inhibiting orthogonal contacts in metal complex based molecular

junctions", *Nanoscale* **2017**, *9*, 9902–9912, DOI 10.1039/C7NR01829K (cit. on pp. 55, 65).

[122] S. Y. Quek, L. Venkataraman, H. J. Choi, S. G. Louie, M. S. Hybertsen, J. B. Neaton, "Amine - Gold linked single-molecule circuits: Experiment and theory", *Nano Letters* **2007**, *7*, 3477–3482, DOI 10.1021/nl072058i (cit. on p. 62).

[123] D. J. Mowbray, G. Jones, K. S. Thygesen, "Influence of functional groups on charge transport in molecular junctions", *The Journal of Chemical Physics* **2008**, *128*, 111103, DOI 10.1063/1.2894544 (cit. on p. 62).

[124] R. Venkatasubramanian, E. Siivola, T. Colpitts, B. O'Quinn, "Thin-film thermoelectric devices with high room-temperature figures of merit", *Nature* **2001**, *413*, 597–602, DOI 10.1038/35098012 (cit. on p. 64).

[125] P. Reddy, S.-Y. Jang, R. A. Segalman, A. Majumdar, "Thermoelectricity in Molecular Junctions", *Science* **2007**, *315*, 1568–1571, DOI 10.1126/science.1137149 (cit. on p. 64).

[126] J. Pommerehne, H. Vestweber, W. Guss, R. F. Mahrt, H. Bässler, M. Porsch, J. Daub, "Efficient two layer leds on a polymer blend basis", *Advanced Materials* **1995**, *7*, 551–554, DOI 10.1002/adma.19950070608 (cit. on p. 64).

[127] J. R. Quinn, F. W. Foss, L. Venkataraman, R. Breslow, "Oxidation Potentials Correlate with Conductivities of Aromatic Molecular Wires", *Journal of the American Chemical Society* **2007**, *129*, 12376–12377, DOI 10.1021/ja0745097 (cit. on p. 65).

[128] M. Parthey, K. B. Vincent, M. Renz, P. A. Schauer, D. S. Yufit, J. A. K. Howard, M. Kaupp, P. J. Low, "A Combined Computational and Spectroelectrochemical Study of Platinum-Bridged Bis-Triarylamine

Systems", *Inorganic Chemistry* **2014**, *53*, 1544–1554, DOI 10.1021/ic402538e (cit. on p. 65).

[129] A. C. Whalley, M. L. Steigerwald, X. Guo, C. Nuckolls, "Reversible switching in molecular electronic devices", *Journal of the American Chemical Society* **2007**, *129*, 12590–12591, DOI 10.1021/ja073127y (cit. on p. 69).

[130] P. Anger, P. Bharadwaj, L. Novotny, "Enhancement and quenching of single-molecule fluorescence", *Physical Review Letters* **2006**, *96*, 113002, DOI 10.1103/PhysRevLett.96.113002 (cit. on p. 69).

[131] P. P. Edwards, A. Porch, M. O. Jones, D. V. Morgan, R. M. Perks, "Basic materials physics of transparent conducting oxides", *Dalton Transactions* **2004**, 2995, DOI 10.1039/b408864f (cit. on p. 69).

[132] J. Harrell, M. Acikgoz, H. Lieber Sasson, I. Visoly-Fisher, A. Genova, M. Pavanello, "Models of Surface Morphology and Electronic Structure of Indium Oxide and Indium Tin Oxide for Several Surface Hydroxylation Levels", *The Journal of Physical Chemistry C* **2018**, acs.jpcc.7b10267, DOI 10.1021/acs.jpcc.7b10267 (cit. on p. 69).

[133] F. Chen, Z. Huang, N. Tao, "Forming single molecular junctions between indium tin oxide electrodes", *Applied Physics Letters* **2007**, *91*, 162106, DOI 10.1063/1.2800303 (cit. on p. 69).

[134] S. Battacharyya, A. Kibel, G. Kodis, P. A. Liddell, M. Gervaldo, D. Gust, S. Lindsay, "Optical modulation of molecular conductance", *Nano Letters* **2011**, *11*, 2709–2714, DOI 10.1021/nl200977c (cit. on p. 69).

[135] S. E. Koh, K. D. McDonald, D. H. Holt, C. S. Dulcey, J. A. Chaney, P. E. Pehrsson, "Phenylphosphonic Acid Functionalization of Indium Tin Oxide: Surface Chemistry and Work Functions", *Langmuir* **2006**, *22*, 6249–6255, DOI 10.1021/la052379e (cit. on p. 69).

[136] S. A. Paniagua, P. J. Hotchkiss, S. C. Jones, S. R. Marder, A. Mudalige, F. S. Marrikar, J. E. Pemberton, N. R. Armstrong, "Phosphonic Acid Modification of Indium−Tin Oxide Electrodes: Combined XPS/UPS/Contact Angle Studies", *The Journal of Physical Chemistry C* **2008**, *112*, 7809–7817, DOI 10.1021/jp710893k (cit. on p. 69).

[137] S. Sergani, Y. Furmansky, I. Visoly-Fisher, "Metal-free molecular junctions on ITO via amino-silane binding—towards optoelectronic molecular junctions", *Nanotechnology* **2013**, *24*, 455204, DOI 10.1088/0957-4484/24/45/455204 (cit. on p. 69).

[138] P. Moreno-García, M. Gulcur, D. Z. Manrique, T. Pope, W. Hong, V. Kaliginedi, C. Huang, A. S. Batsanov, M. R. Bryce, C. Lambert, T. Wandlowski, "Single-molecule conductance of functionalized oligoynes: Length dependence and junction evolution", *Journal of the American Chemical Society* **2013**, *135*, 12228–12240, DOI 10.1021/ja4015293 (cit. on p. 72).

[139] Y. S. Park, J. R. Widawsky, M. Kamenetska, M. L. Steigerwald, M. S. Hybertsen, C. Nuckolls, L. Venkataraman, "Frustrated Rotations in Single-Molecule Junctions", *Journal of the American Chemical Society* **2009**, *131*, 10820–10821, DOI 10.1021/ja903731m (cit. on p. 72).

[140] T. Y. Li, C. Su, S. B. Akula, W. G. Sun, H. M. Chien, W. R. Li, "New Pyridinium Ylide Dyes for Dye Sensitized Solar Cell Applications", *Organic Letters* **2016**, *18*, 3386–3389, DOI 10.1021/acs.orglett.6b01539 (cit. on p. 73).

[141] S. Ahn, S. V. Aradhya, R. S. Klausen, B. Capozzi, X. Roy, M. L. Steigerwald, C. Nuckolls, L. Venkataraman, "Electronic transport and mechanical stability of carboxyl linked single-molecule junctions", *Physical Chemistry Chemical Physics* **2012**, *14*, 13841–13845, DOI Doi10.1039/C2cp41578j (cit. on p. 73).

[142] C. Sabater, D. Gosálbez-Martínez, J. Fernández-Rossier, J. G. Rodrigo, C. Untiedt, J. J. Palacios, "Topologically Protected Quantum Transport in Locally Exfoliated Bismuth at Room Temperature", *Physical Review Letters* **2013**, *110*, 176802, DOI 10.1103/PhysRevLett.110.176802 (cit. on p. 74).

[143] M. Muntwiler, C. D. Lindstrom, X.-Y. Zhu, "Delocalized electron resonance at the alkanethiolate self-assembled monolayer/Au(111) interface", *The Journal of Chemical Physics* **2006**, *124*, 081104, DOI 10.1063/1.2171437 (cit. on p. 75).

[144] N. Nerngchamnong, L. Yuan, D.-C. Qi, J. Li, D. Thompson, C. A. Nijhuis, "The role of van der Waals forces in the performance of molecular diodes", *Nature Nanotechnology* **2013**, *8*, 113–118, DOI 10.1038/nnano.2012.238 (cit. on p. 78).

[145] L. Scullion, T. Doneux, L. Bouffier, D. G. Fernig, S. J. Higgins, D. Bethell, R. J. Nichols, "Large Conductance Changes in Peptide Single Molecule Junctions Controlled by pH", *The Journal of Physical Chemistry C* **2011**, *115*, 8361–8368, DOI 10.1021/jp201222b (cit. on p. 84).

[146] W. Zhang, S. Gan, A. Vezzoli, R. J. Davidson, D. C. Milan, K. V. Luzyanin, S. J. Higgins, R. J. Nichols, A. Beeby, P. J. Low, B. Li, L. Niu, "Single-Molecule Conductance of Viologen-Cucurbit[8]uril Host-Guest Complexes", *ACS Nano* **2016**, *10*, 5212–5220, DOI 10.1021/acsnano.6b00786 (cit. on p. 84).

[147] K. Wang, A. Vezzoli, I. M. Grace, M. McLaughlin, R. J. Nichols, B. Xu, C. J. Lambert, S. J. Higgins, "Charge transfer complexation boosts molecular conductance through Fermi level pinning", *Chemical Science* **2019**, *10*, 2396–2403, DOI 10.1039/C8SC04199G (cit. on p. 84).

[148] N. Ferri, PhD thesis, University of Liverpool, **2018** (cit. on p. 86).

[149] M. S. Inkpen, M. Lemmer, N. Fitzpatrick, D. C. Milan, R. J. Nichols, N. J. Long, T. Albrecht, "New Insights into Single-Molecule Junctions Using a Robust, Unsupervised Approach to Data Collection and Analysis", *Journal of the American Chemical Society* **2015**, *137*, 9971–9981, DOI 10.1021/jacs.5b05693 (cit. on p. 87).

[150] D. Roldan, V. Kaliginedi, S. Cobo, V. Kolivoska, C. Bucher, W. Hong, G. Royal, T. Wandlowski, "Charge Transport in Photoswitchable Dimethyldihydropyrene-Type Single-Molecule Junctions", *Journal of the American Chemical Society* **2013**, *135*, 5974–5977, DOI 10.1021/ja401484j (cit. on p. 88).

[151] M. L. Perrin, R. Frisenda, M. Koole, J. S. Seldenthuis, J. A. Gil, H. Valkenier, J. C. Hummelen, N. Renaud, F. C. Grozema, J. M. Thijssen, D. Dulić, H. S. Van Der Zant, "Large negative differential conductance in single-molecule break junctions", *Nature Nanotechnology* **2014**, *9*, 830–834, DOI 10.1038/nnano.2014.177 (cit. on p. 89).

[152] N. P. Guisinger, M. E. Greene, R. Basu, A. S. Baluch, M. C. Hersam, "Room Temperature Negative Differential Resistance through Individual Organic Molecules on Silicon Surfaces", *Nano Letters* **2004**, *4*, 55–59, DOI 10.1021/nl0348589 (cit. on p. 95).

[153] Y. Dubi, "Transport Through Self-Assembled Monolayer Molecular Junctions: Role of In-Plane Dephasing", *The Journal of Physical Chemistry C* **2014**, *118*, 21119–21127, DOI 10.1021/jp503887p (cit. on p. 96).

[154] M. L. Perrin, E. Burzurí, H. S. J. van der Zant, "Single-molecule transistors", *Chem. Soc. Rev.* **2015**, *44*, 902–919, DOI 10.1039/C4CS00231H (cit. on p. 96).

[155] C. D. Bostick, S. Mukhopadhyay, I. Pecht, M. Sheves, D. Cahen, D. Lederman, "Protein bioelectronics: a review of what we do and do not

know", *Reports on Progress in Physics* **2018**, *81*, 026601, DOI 10.1088/1361-6633/aa85f2 (cit. on p. 96).